INTEGRATED ULTRA-HIGH *Q* BULK ACOUSTIC WAVE RESONATORS IN THICK MONOCRYSTALLINE SILICON CARBIDE

A Dissertation
Presented to
The Academic Faculty

By

Jeremy Yang

In Partial Fulfillment
of the Requirements for the Degree
Doctor of Philosophy in the
School of Physics

Georgia Institute of Technology

August 2020

Copyright © Jeremy Yang 2020

INTEGRATED ULTRA-HIGH *Q* BULK ACOUSTIC WAVE RESONATORS IN THICK MONOCRYSTALLINE SILICON CARBIDE

Approved by:

Dr. Farrokh Ayazi, Advisor
School of Electrical and Computer Engineering
Georgia Institute of Technology

Dr. Chandra Raman
School of Physics
Georgia Institute of Technology

Dr. Zhigang Jiang
School of Physics
Georgia Institute of Technology

Dr. Azadeh Ansari
School of Electrical and Computer Engineering
Georgia Institute of Technology

Dr. Oliver Brand
School of Electrical and Computer Engineering
Georgia Institute of Technology

Date Approved: June 16, 2020

"Hope" is the thing with feathers -
That perches in the soul -
And sings the tune without the words -
And never stops - at all -

And sweetest - in the Gale - is heard -
And sore must be the storm -
That could abash the little Bird
That kept so many warm -

I've heard it in the chillest land -
And on the strangest Sea -
Yet - never - in Extremity,
It asked a crumb - of me

Emily Dickinson

To my dearest friends and family.
To my beautiful cats Pebbles and Hammy (Dec. 2009 - Apr. 27th, 2020).

ACKNOWLEDGEMENTS

I sincerely believe that everyone you interact with touches you in some way, anything from a brief glance, a casual acquaintance, to a lifelong friendship. Everything in this world has an art or a romance; one just has to find it. With that said, I'm extremely grateful to have had the opportunity to work with Dr. Ayazi, the rest of my colleagues on the IMEMS team and my thesis committee: Drs. Raman, Jiang, Ansari and Brand. I'm well aware I'm not the easiest person to work with and the experience I've garnered both technically and personally is indispensable to me. These past few years have effected in me a great deal of introspection and reflection about what is truly important. Again, thank you to Dr. Ayazi for enabling this journey, and thank you to Dr. Anosh Daruwalla, Dr. Haoran Wen, Dr. Seungdeok Ko, Dr. Chang-shun Liu, Pranav Gupta, Seungyong Shin and Mojtaba Hodjat-Shamami. In particular, I want to thank Dr. Benoit Hamelin for providing invaluable guidance personally and professionally—your passion left me awestruck.

Naturally, the staff at the Institute for Electronics and Nanotechnology were absolutely critical in the completion of this work. Gary Spinner, Vinh Nguyen, Dr. Hang Chen, Andrew Watkins, Dr. Chris Yang, Dr. Mikkel Thomas, Dean Sutter, Todd Walters, Eric Woods, Charlie Suh, Charlie Turgeon, Alex Gallmon, Devin Brown and Ben Hollerbach among many others. Not only did they provide their time and expertise, but also their levity, good-humor and compassion. Thanks also goes to administrative staff in the Schools of Physics and Electrical and Computer Engineering.

I extend my sincere gratitude to my therapist Yvette Cianfaglione who has been an invaluable presence for the past three years, providing me counsel and reinforcement. Our

meetings were something that I could look forward to on a weekly basis and our chats were always constructive to me, whether discussing the profound or the more light-hearted like movies and books. I'm also indebted to the staff at Georgia Tech's health services including Dr. Jennifer Fortner and Dr. Mark Corsale.

My close friends Shane Jacobeen, Evan Mistur, Yiran Hu and Anna Miettinen who've helped me weather so many storms and act without reservation or condition as my lightning rods. I'm not an artist and I regret that I lack the faculty to really articulate just how much you all mean to me. Thanks must go to other students that have become not only technical liaisons but sincere friends: Joe Gonzalez, Sreejith Kochupurackal Rajan, Paul Jo and Steven Schwartz.

My two cats have seen me through the darkest moments of my life; they lifted me up and provided me unconditional love and companionship. They buoyed me through college and graduate school with the sardonic loving indifference that only cats can provide. Sadly, in the course of writing this dissertation, Hamilton passed away due to cancer and was only weeks away from completing this journey with me. Indisputably, my one regret in this life is not being able to reciprocate the love and life that he afforded me and his sister Pebbles. The written word's fundamental inability to capture the capacity of human emotion is one of life's great tragedies.

Finally, my family has been the one constant through all of this; knowing that I have their unconditional support has been my sanctuary. Thank you to my sisters Lanshin and Lanwei, my brother Jonathan and my parents Diana and Ayfang. The work that I put in has been for you all.

TABLE OF CONTENTS

Acknowledgments v

List of Tables x

List of Figures xii

List of Symbols and Abbreviations xxii

Summary xxiv

Chapter 1. Introduction and Background 1

1.1 Resonant Gyroscope Operational Principles 2

1.1.1 Lumped Parameter Harmonic Motion 4

1.1.2 Disk Gyroscope Electrical Transduction Performance Metrics . . . 8

1.2 Thesis Organization 11

Chapter 2. Dissipation in Silicon Carbide Bulk Acoustic Wave (BAW) Resonators 12

2.1 Measuring Quality Factor (Q) 12

2.2 Dissipation in Silicon Carbide MEMS Resonators 15

2.3 Intrinsic Dissipation Mechanisms 16

2.3.1 Dissipation due to Phonon-Phonon Interactions (AKE) 16

2.3.2 Thermoelastic Dissipation (TED) 20

2.4 Extrinsic Dissipation Mechanisms 25

2.4.1 Anchor and Support Losses (ANC) 25

2.4.2 Other Dissipation Mechanisms 26

2.5 Silicon Carbide as a MEMS material 28

Chapter 3. Monocrystalline Silicon Carbide Process Technology for Fabrication of Thick Electrostatic Resonators 30

3.1 Silicon Carbide: Growth and Crystallography 31

3.2 Crystallinity and Degenerate Gyroscopic Modes 33

3.3 SiC-on-Insulator (SiCOI) Platform 35

3.4 Fabrication of SiC Resonators 37

3.4.1 Silicon Carbide Deep Reactive Ion Etch 40
3.4.2 Etch Chemistry and Parameters 45
3.4.3 Effect of Process Parameters on DRIE 46
3.4.4 Polysilicon Plug 50
3.4.5 Sidewall Passivation 52
3.4.6 Backside Etch and Release 54
3.4.7 Ohmic Contact Formation 55

Chapter 4. SiC Disk Resonators for Gyroscopic Applications 58
4.1 Optically Transduced Disk Resonators 59
4.1.1 Disks with Release Holes 59
4.1.2 Solid Disks 63
4.2 Substrate Decoupled Disks: Design and Simulation 65
4.2.1 3D Substrate Decoupling for Anchor Loss 66
4.2.2 Results 71
4.2.3 Experimental Confirmation of Transverse Isotropy 77
4.3 Capacitively Transduced Disk Resonators 78
4.3.1 Capacitive Actuation and Optical Sensing 78
4.3.2 Capacitively Transduced Disks on PnC 79
4.4 Sources of Frequency Split 82

Chapter 5. Ultra-High Q Electrostatic Silicon Carbide Lamé Mode Resonators . 85
5.1 Theory and Background 86
5.2 Design and Fabrication 87
5.2.1 Phononic Crystal Tethers 89
5.2.2 Process and Fabrication 90
5.3 Results 93
5.4 4H-SiC Elasticity: FEA Simulation Vs. Reality 99

Chapter 6. Conclusion and Future Work 104
6.1 Exploring the Limits of Dissipation 104
6.2 BAW Gyroscopes with High Aspect Ratio Capacitive Gaps 106
6.3 Concluding Remarks 108

Appendices **110**

Appendix A. Hooke's Law for Anisotropic Media **111**
A.1 Universal Anisotropy Index 114
A.2 Material Frame Rotation 116

Appendix B. Bulk Elliptical Modal Analysis in Disks **122**
B.1 Elliptical Mode Frequency Split in Disks 126

Appendix C. Material Parameters used for Simulation **128**
C.1 Stiffness Matrices used in Simulation 128

Appendix D. Process Parameters **132**

Appendix E. Density Functional Theory in Quantum Espresso **136**

Bibliography **139**

LIST OF TABLES

1.1 Gyroscope application grades and typical performance specifications [5, 6]. 1

2.1 Prominent MEMS dissipation mechanisms [20] 16

2.2 Akhiezer limit $f \cdot Q$ of common resonator materials and relevant material properties. 19

2.3 Bulk parameters comparing silicon and silicon carbide, values are reported for $T = 300$ K. $c_{l,t}$ are sound velocities for longitudinal and transverse waves, respectively. 29

3.1 Properties of common SiC polytypes with comparison to silicon [59]. . . . 32

3.2 Inexhaustive review of masking materials used for deep reactive ion etching of silicon carbide. 40

3.3 Typical solution composition and parameters used for Ni electroplating: Technic, Inc.'s Elevate Ni RTU nickel sulfamate solution. Parameters a typical user should monitor are in **bold**. 43

3.4 Partial list of parameters available in an ICP-DRIE system. Recipe values for AOE and AOE Pro highlight the respective tools' capabilities. 47

4.1 Device parameters and Q simulation for fully capacitive disks with 3D substrate decoupling fabricated on SiCOI. 81

5.1 Parameters for resonance frequencies for various bulk modes depicted in Figure 5.1. C_{eq} expressions for both cubic materials [131] and hexagonal materials are listed. 87

5.2 Device parameters and simulation for fully capacitive Lamé mode devices in thick 4H-SiCOI. 94

5.3 Comparison between Akhiezer-limited Lamé mode resonators in Si and this work in SiC. 95

5.4 Measured and simulated frequencies of devices measured in this work. Simulated frequencies are performed in COMSOL with elasticity values from Kamitani *et al.* 101

5.5 Simulated values of modes using new stiffness matrix (5.4). The values of C_{11} and C_{66} are chosen to match measurements of capacitive disks with diameter of 1.44 mm and in general simulate the elliptical modes with greater precision. 103

6.1 Overview of material parameters relevant to Q_{AKE} and Q_{TED} as a function of temperature at low temperature. A good reference for low temperature material properties can be found in [152, Ch. 2]. 106

6.2 Comparison of proposed SiC gyro design utilizing laser trimming along with existing Si BAW gyros and state-of-the-art ring laser gyro [157]. . . . 108

A.1 Miller index notation for cubic crystals [158] and Miller-Bravais index notation for hexagonal crystals where $u + v + t = 0$ [159]. 111

B.1 Parameters to calculate in-plane elliptical wineglass mode frequencies using (B.11). k_m depends upon the Poisson's ratio of the material which can be derived from the stiffness matrices via (A.5) for orthotropic and cubic materials and more directly via (A.23e) for hexagonal materials. The last two columns are in 4H-SiC. 125

C.1 Relevant bulk material parameters used in FEA simulation. Stiffness matrices follow in section C.1. 128

D.1 Wet etch chemistries and their material compatibilities. ✓, ✗ and ✓, ✗ denote strong and weak compatibilities and incompatibilities, respectively. SiC is virtually totally inert to all of these chemistries. 132

D.2 Photoresist conditions. In general, dose and softbake time scale linearly with thickness whereas thickness is proportional to the inverse square root of speed. AZ P4620 was used for general thick resist use. AZ 9260 high resolution resist was used for nickel electroplating. SC1827 was used for poly patterning and oxide etching. Softbakes conducted at 110 °C, 110 °C and 120 °C for AZ P4620, AZ 9260 and SC1827, respectively. 134

D.3 Parameters for etching vias in the silicon handle layer in an STS Pegasus ICP tool. → indicates the parameter is ramped over the duration of the etch. 135

LIST OF FIGURES

1.1 A Qualtré BAW gyroscope with two degenerate $m = 3$ wineglass modes center-supported by a pedestal [9]. 3

1.2 MEMS gyroscope as a two-degree-of-freedom spring-mass system. 4

1.3 (a) Normalized real and imaginary responses (1.9) as a function of frequency split. The peak's sharpness is defined by Q_2. (b) Sense response of mode-split (left) and mode-matched (Q-amplified, right) gyroscopes. 7

2.1 A time domain plot of the displacement of a damped harmonic oscillator with quality factor Q and angular frequency ω. The exponential decay curve (blue) envelopes the damped periodic motion (red). By determining the time τ at which $u(\tau) = 1/e$, one can extract the quality factor Q via (2.3). 14

2.2 The acoustic wave is modeled as a perturbation of a large number of coherent phonons (red peak at $\omega_{resonance}$) disturbing the thermal Planck spectral energy equilibrium (black). Through entropy-producing processes, collision and scattering with thermal phonons will tend the distribution back to thermal equilibrium [21]. The Debye frequency ω_D is the frequency of highest occupancy; contrary to photons which can have infinite frequency, phonons exist in finite lattice spacing and cannot support infinitesimally small wavelengths. 17

2.3 With respect to Akhiezer damping, silicon carbide is a superior mechanical material. The bend in the curves represents the transition to the Landau-Rumer regime of dissipation, well above our frequencies of interest. 19

2.4 Tuning fork gyros operate in the Debye regime where the thermal frequency lies near the resonant mechanical frequency. In contrast, BAW resonators operate adiabatically, allowing for much higher Q factors. 21

2.5 The TED of a resonant mode can be modeled as the sum the overlap between the mechanical strain and thermal modes of the mode. In the case of the disk, there is a large overlap between the mechanical strain and the first thermal mode which has $\lambda = 0$, resulting in no dissipation. 24

2.6 The mechanical strain (top left) of the fundamental mode for a fixed-fixed cantilever beam interacts heavily with a thermal eigenmode (top right), resulting in large overlap integrals (red dots) and subsequently much higher TED. The alternating dots correspond to odd (high) and even (low) thermal eigenmodes. 24

2.7 Substrate decoupling for disk gyroscopes. Without decoupling features, large shear deformation is found at the anchor. Introducing substrate-decoupling features greatly mitigates deformation at the anchor, obstructing losses through the pedestal [19]. 26

2.8 (a) PML simulations of a lateral mode AlN-on-Si resonator. (b) Eigenfrequency simulations reveal band gaps forming along with two eigenmodes. (c) SEM of arrayed LAB tethers. (d) S_{21} measurements of two resonators with (left) and without (right) LAB tethers [35, 36]. 27

3.1 Anisotropy (or lack thereof) of Young's modulus E_1, Poisson's ratio ν_{12} and shear modulus G_{12} in (0 0 0 1) 4H-SiC (red), (1 0 0) Si (blue) and (1 1 1) Si (green). Here, 0° corresponds to wafer directions $[1\,1\,\bar{2}\,0]$, [1 0 0] and $[1\,1\,\bar{2}]$, respectively. 4H-SiC's transverse isotropy renders its elastic behavior azimuthally invariant similar to (1 1 1) Si. In contrast, (1 0 0) Si exhibits variations up to 45 %. 33

3.2 COMSOL simulated mode shapes for the secondary elliptical mode ($m = 3$) for (a) (1 0 0) Si, (b) (1 0 0) 3C-SiC and (c) (0 0 0 1) 4H-SiC. Referring to the heat map, significant material anisotropy in cubic materials such as (1 0 0) 3C-SiC and (1 0 0) Si manifests itself as non-uniform anti-nodal displacements. Transversely isotropic (0 0 0 1) 4H-SiC shows uniform displacement around the circumference of the disk. 34

3.3 (a,b) (1 0 0) Si anisotropy results in non-uniform radial displacement and requires deliberate electrode placement for tuning, drive and pickoff. (c) On the other hand, (0 0 0 1) SiC could potentially simplify electrode placement configurations. 34

3.4 COMSOL® simulation of the effect of polar cut misalignment on the frequency split of the degenerate $m = 3$ elliptical modes. (a) Significant non-degeneracy occurs in (1 0 0) Si with frequency splits in excess of 100 ppm. (b) This is significantly exacerbated in (1 1 1) Si with frequency splits approaching 1000 ppm whereas frequency split is lower by several orders of magnitude in SiC (c). The flatness between −3° to 3° is likely due to meshing. Note that the three y axes are not commensurate with one another. 35

3.5 (a) $E_{1,2}$ show large degree of splitting in 4° off-axis (1 1 1) Si. (b) 4H-SiC remains virtually isotropic despite 4° wafer cut. 36

3.6 (left) Surface acoustic microscope (SAM) image of a completely bonded SiCOI wafer without voids. (right) SEM of the HF-released (etch rate of 6 μm/min) SiCOI wafer [63]. 37

3.7 (a) Edge-trimmed wafers prior to thermal wet oxidation. The darker wafer in front is a 4° off-axis wafer. (b) Pressure bonded wafers reduce voiding. (c) A successfully grinded wafer; edge trimming allows for grinding despite voids. 38

3.8 Basic process flow for a capacitive silicon carbide disk resonator with backside release pattern/PnC. Fabrication of other resonators can be derived from this one. 39

3.9 (a) Electroplated nickel on Cr/Au seed layer dry etched with transference of the PR's wavelength-limited scalloping. The lateral waviness at the bottom is due to the substrate's rough features, an artifact from the grinding process. (b) Wet-etched Ti/Cu seed layer shows a small gap between the nickel and substrate. The gap's effect on subsequent DRIE is disputed. 41

3.10 Various nickel defects arising due to contamination be it intrinsically (solution additives reacting with the nickel anode) or extrinsically introduced. . 44

3.11 As trench width decreases, etch rate decreases (right to left). 46

3.12 AOE Pro recipe (Table 3.4) 60 min: (a) Passivation grows at ~ 15 nm/min (b) The recipe shows a fairly strong aspect ratio dependence for narrow trenches and only exhibits etch defects in 3.4 μm-wide trenches past 40 μm. Remaining nickel is shown in green with selectivities ranging from 15:1 to 30:1 for narrow trenches. (c) Wide trenches and features etch at a rate of 1.5 μm/h with minimal micromasking and an etch selectivity of ~ 45:1. (d) The same recipe employed on SiCOI with little to no difference in performance, showing that the recipe is robust to substrate changes. 49

3.13 Etch rates of a 4 μm-wide gap for different SF_6 flow rates (a) 40 sccm, 90 min: 20 μm/h (b) 150 sccm, 45 min: 45 μm/h, (c) 200 sccm, 45 min: 50 μm/h and (d) 250 sccm, 60 min: 54 μm/h. Runs at the tool's MFC-limited 300 sccm were attempted but were scrapped due to the tool's automatic pressure controller reaching its limit. 50

3.14 Etch interactions with the BOX layer: (a) footing occurs due to BOX charging. This effect is visible in SEM (bright interlayer) as incident electrons charge the BOX layer, adding electrons to the sample and distorting the image. (b) Close-up of the bottom of the trench with footing ~ 2 µm on each side due to over-etch. BOX is colored brown in post-processing. (c-e) Different locations in the same sample as Figure 3.12d showing overetches of 0 µm, 5 µm and 15 µm, respectively. TTV becomes incredibly important barring other developments in DRIE of silicon carbide. 51

3.15 Process flow for polysilicon plug. Provides resonator polarization with additional benefit of augmented pedestal strength and HF resilience. 52

3.16 Electron dispersive x-ray spectroscopy of sidewall passivation. Incident electrons are scattered and detected with each atom exhibiting a unique spectrum. (a) SEM of an etched high aspect ratio trench before cleaning. (b-d) Atomic count mapping for Ni, F, and C. 53

3.17 (a) Passivation builds at ~1 µm/h, limiting the depth of the etch due to trench pinching and subsequent closing. (b) Following in-situ clean using EKC 162™ residue remover, the trench is cleaned with the nickel mask preserved. 54

3.18 (a) Passivation peeling after a certain deposition thickness. (b) Passivation charges and deflects incoming plasma species causing sidewall damage and daggering. (c) A particularly severe case. In this case, improper *ex-situ* cleaning exacerbated the passivation peeling problem. (d) Everything else constant, reducing the Ar flow removes peeling while maintaining etch depth and rate. 55

3.19 (a) A straddling gap type n-N heterojunction with depletion width x_d and accumulation width x_a. The band discontinuities arise due to the mismatch between the valence and conduction bands of the two semiconductors, leading to a barrier height ΔE_C, the energy gap required for thermionic emission to occur. (b) Annealing at high temperatures aims to reduce effective barrier height by introducing carbon vacancies which act as electron acceptors. . . 56

3.20 (a) Nitridation of poly silicon in a nitrogen rich environment following rapid thermal processing at 1200 °C. (b) Significant damage to the polysilicon layer following HF cleaning and sonication. This affects not only ohmic contact, but roughness can make it extremely difficult to wirebond. (c) Depositing a PECVD protective film and limiting ambient N_2 flow prior to high temperature anneal can prevent nitridation. 57

4.1 Disks fabricated in chronological order: (a) perforated disks (b) Solid disks (c) solid disks on phononic crystal (d) capacitive disk on phononic crystal. . 58

4.2 Optical image of fabricated disk with release holes 200 µm wide in radius. Elliptical wineglass mode shapes simulated via COMSOL® are depicted on the right; the silicon oxide pedestal is shown in green [63]. 60

4.3 Schematic (left) and photograph (right) of the LDV measurement setup [63]. 60

4.4 (a) LDV spectrum of the perforated SiC disk with simulated mode shapes, (b) two degenerate peaks from the $m = 3$ modes, (c) its magnified view [63]. 61

4.5 Ringdown measurement of the fabricated disk. The amplifier is switched off at 2.8 s and the time response is measured. Eq. (2.3) yields a Q of 120k, matching simulation well. 61

4.6 Comparison between measurements and simulations. The strain energy density is concentrated near the pedestal for the first two elliptical modes resulting in lower $Q_{ANC(m=0,2)}$ compared to the $m = 3$ modes [96, 97]. . . . 62

4.7 SEM of 9 µm disk with release holes (left). COMSOL thermoelastic dissipation eigenmode simulation shows significant temperature and strain gradients due to introduction of release structures, reducing Q-factor from $>100 \times 10^6$ in a solid disk to 170×10^3 in a perforated disk. 63

4.8 (left) Optical image of a disk 5 µm in diameter and a pedestal 80 µm in radius with 50 µm misalignment due to spatially varying HF etch rates during release. Note the periodic color fringes due to constructive and destructive wave interference at the BOX layer; this indicates disk bending. (right) Curves of constant pedestal height plotting Q_{ANC} for varying pedestal radii. The dashed line in red is the Q_{TED} for the disk, unperturbed for variations at this size. 64

4.9 Optically measured modes in a 5 µm diameter disk with neither frontside nor backside release holes. Qs are limited by anchor loss to the substrate and generally increase with increasing mode number (counter-clockwise from bottom left). 65

4.10 Measured values of bulk elliptical modes compared with simulation of various damping mechanisms (ANC, TED, AKE). Q is limited by anchor loss in devices without substrate decoupling or frontside release holes. Grey dotted line depicts the Akhiezer fundamental limit. 66

4.11 (top) Phononic crystals have potential application across the phononic spectrum. Bottom left: periodic distribution of hollow stainless-steel cylinders, with a diameter of 2.9 cm, simple cubic symmetry and a unit cell of 10 cm exhibits attenuation peaks from 1 kHz to 5 kHz [100]. Bottom middle: epoxy with circular occlusions forming a triangular lattice fabricated via interference lithography with bandgaps 1 GHz [111] Bottom right: silicon nanomesh fabricated on SOI to mitigate thermal transport [102]. 67

4.12 (left) Eigenmode simulations using Bloch-Floquet boundary show a bandgap centered at 5 MHz for a = 420 µm for the honeycomb unit cell. (right) The unit cell with high symmetry points Γ, M and X. The eigenmode frequencies are found along paths between these points, garnering a complete picture of wave propagation within the cell. For illustrative purposes, the unit cell is depicted in real space and **not** k-space. 69

4.13 The honeycomb lattice (right) offers the widest bandgap at the smallest filling factor. The unit cell, when placed in a rectangular lattice, creates a honeycomb tessellation (bottom right) [70]. 69

4.14 Handle layer thickness affects Q_{ANC}. At $\lambda/4$, wave interference creates a standing wave with a node at the suspended end of the device. In concert with a PnC, anchor loss can be made negligible [70]. 70

4.15 As more unit cells are added, Q_{ANC} (blue) surpasses Q_{TED} (red) and finally Q_{AKE} (dashed green). In a 1540 µm diameter disk, radial mode at 5 MHz is TED limited [70]. 71

4.16 (a) SEM of BAW SiC disk resonator (100 µm thick, 1540 µm diameter) anchored upon a phononic crystal of three unit cells. The radial mode resonates at 5 MHz.(b) The device rests upon the silicon handle layer with 2 µm gap determined by the thickness of the BOX layer. The lack of an etch stop manifests itself as over-etch into the silicon handle layer [70]. 71

4.17 Simulated dispersion curves (gray) depict frequencies of allowed propagation across the first Brillouin zone. Measured Qs of bulk modes across devices of varying size inside and outside the bandgap (purple). The breathing mode ($m = 0$) exhibits Q of 3.7×10^6 (green circle), perfectly coinciding with $\lambda/4$ frequency at 5 MHz. Modes operating away from the $\lambda/4$ frequency ($m = 3$ modes at 5.3 MHz) suffer in performance [70]. 72

4.18 Radial mode frequency response of a 1540 µm diameter disk with $f \cdot Q$ product of 1.85×10^{13} Hz. Measured Q and f corroborate simulation well. $Q_{simulated}$ incorporates fabrication defects [70]. 73

4.19 Measured frequency split $\Delta f/f$ of several bulk elliptical modes below 40 ppm. $m = 3$ modes exhibit 18 ppm frequency split [70]. 74

4.20 (a) With increasing striation radius/disk radius ratio, simulations show a precipitous reduction in Q_{TED} of the radial mode. (b) Atomic force micrograph of the sidewall of the disk showing striation and roughness on the micron scale [70]. 75

4.21 (a) SEM of 4.05 µm diameter SiC disk resonator with simulated $m = 8$ mode shape (inset). (b) Spectrum of measured elliptical modes showing the highest Q within the bandgap and—more specifically—the $\lambda/4$ matching. (c) $m = 8$ resonant mode with a measured Q of 18.7×10^6 corresponding to $f \cdot Q = 9.5 \times 10^{13}$ Hz. (d) Frequency split of odd-numbered elliptical modes are low; in this case, 2.8 ppm for the $m = 9$ mode [71]. 76

4.22 Optically measured peaks in a 1.64 mm diameter disk exhibiting small frequency splits below for both even and odd-ordered modes (a) $m = 2$ mode at 3.61 MHz with $\Delta f/f = 110$ ppm. (b) $m = 3$ mode at 5.52 MHz with $\Delta f/f = 9$ ppm. (c) $m = 4$ mode at 7.18 MHz with $\Delta f/f = 63$ ppm. (d) $m = 5$ mode at 8.73 MHz with $\Delta f/f = 14$ ppm. 77

4.23 Setup for capacitive actuation and optical readout along with optical image of disk [122]. 78

4.24 Optically measured peaks show low frequency splits and good frequency agreement with simulation. (top left) $m = 2$ mode with Q = 99×10^3 and $\Delta f/f = 50$ ppm. (top right) $m = 3$ mode with Q = 199×10^3 and $\Delta f/f = 8$ ppm. (bottom) $m = 4$ mode with Q = 1.1×10^6 and $\Delta f/f = 65$ ppm. 79

4.25 (a) Variable-pressure SEM (to minimize charging) of capacitive disk with wirebonded drive and sense electrodes for degenerate $m = 3$ modes; the poly plug cap is in the center. (b) Optical image of the disk. SiC's wide bandgap and the device layer's smoothness renders it transparent to visible light revealing the PnC and the spoke release configuration below the disk. Fixed-fixed cantilever test structures surround the device. 80

4.26 Schematic for capacitive transduction of a disk resonator in 4H-SiCOI substrate [71]. The poly plug allows application of V_P without requiring wirebonding to the center of the disk. 81

4.27 (a,b) Degenerate $m = 3$ elliptical modes with Q in excess of 2.8×10^6. (c) S_{21} frequency response showing an as-born $\Delta f/f$ of 22 ppm. (d) Frequency response of radial mode at 5.5 MHz with $Q = 750 \times 10^3$, mirroring simulation well. 83

5.1 (a) Lamé mode with four nodal points ideal for anchoring. (b) Face shear mode. These two modes characteristically show simultaneous contraction and expansion between two orthogonal axes. (c) Square extensional mode with uniform displacement analogous to the radial breathing mode in disks. 86

5.2 65 µm-thick Lamé mode resonators exhibit high bulk (blue) and surface (red) Q_{TED} (148×10^6 and 50×10^6, respectively). (inset, in red) Roughness is modeled as uniform sidewall asperities. In practice, the as-born roughness of the sidewall is chaotic and difficult to simulate. The quantum Akhiezer limit (green) is ~100×10^6 at 6.27 MHz for a $Q_{Theoretical}$ of 45×10^6 for an acoustically decoupled device. 88

5.3 Eigenfrequency simulation with Bloch-Floquet boundary conditions in a 1D PnC. Allowable eigenmodes surround a bandgap centered on 6.27 MHz in a 700 µm long unit cell (inset). 90

5.4 (a) Perfectly matched layer eigenfrequency simulation of the Lamé mode with a plain tether (inset). The tether introduces spurious eigenmodes and waviness; consequently, varying tether length has a highly volatile effect on both f_{res} and Q_{ANC}. Further, absolute Q_{ANC} never exceeds 1×10^6. (b) The introduction of the PnC (inset) confers frequency robustness; the variation is on the order of Hz and can likely be attributed to meshing variation. Additionally, there is a clear positive monotonic relation between the number of unit of cells and Q_{ANC}. For comparison, the lengths of one, two and three unit cells are 1100 µm, 1900 µm and 2700 µm, respectively with Q_{ANC} exceeding 1×10^9 with two or more unit cells. 91

5.5 (top) An electroplated Ni mask is used for DRIE of 5 µm-wide smooth, vertical trenches in thick SiCOI substrates. Missing nickel on the left and SiC damage in the cleave plane are artifacts of the dicing process. (bottom) Without ex-situ passivation removal during etching, trenches are smooth with 50 nm surface roughness. 92

5.6 (a) SEM of an on-axis 4H-SiC Lamé mode resonator with phononic crystal (PnC) tether. A thin layer of LPCVD polysilicon (colored yellow) ensures ohmic contact between the wire bond and the electrodes. (b) Optical view of the transparent SiC square resonator above the Si cavity. The cavity facilitates release of the solid square resonator; the copper tape is visible below. 94

5.7 Cross-sectional schematic of the electrostatic transduction of a SiC-on-Insulator Lamé mode resonator. The cavity below the resonator obviates surface tension effects during drying that potentially crack the tethers. . . . 95

5.8 (a) The fabricated square resonator with one PnC cell exhibits a maximum Q of 12.8×10^6 for an $f \cdot Q = 8.0 \times 10^{13}$ Hz. (b) A similar square resonator with two PnC unit cells showed a higher Q of 20×10^6 yielding an $f \cdot Q = 1.25 \times 10^{14}$ Hz, over 4×higher than Si's quantum Akhiezer limit. 96

5.9 Square extensional mode measured in the same devices show a Q of 450×10^3 at 7.61 MHz, agreeing with simulation. Strong displacement at the corner tether locations leaks energy readily (inset). 97

5.10 TCF of 4H-SiC monocrystalline Lamé mode resonators is -12 ppm/°C with good linearity. 99

6.1 (a) Calculated coefficient of thermal expansion of Si from 0 K to 700 K with a zero at 120 K. In theory, this would eliminate TED entirely. (b) The Grüneisen parameter also sees a zero near 120 K as one would expect. (c) The heat capacity of Si tending toward zero. 105

6.2 (a) SEM image of a prototyped HARPSS on SiC device. (b) Cross section in a 40 µm thick substrate with a 440 nm gap. 107

6.3 Work presented in this dissertation show the highest mechanical $f \cdot Q$ in 4H-SiC and just under 10× below the fundamental phonon-phonon dissipation limits. 109

A.1 (a) A standard (1 0 0) silicon wafer with wafer flat aligned to the [1 1 0] direction. Rotated axes ($X'Y'$) show transformation from [1 0 0] to [1 1 0] alignment. (b) A standard {0 0 0 1} on-axis 4H-SiC wafer with wafer flat aligned to the $[1\,1\,\bar{2}\,0]$ direction. The red axes $a_{1,2}$ are lattice vectors that form the basis spanning crystal space. Natural Cartesian axes (black) aligned to reported crystallographic constants differ from as-manufactured flats, though for hexagonal SiC, this is largely irrelevant. 112

A.2 Hexagonal close packed crystallography. (a) The hexagonal unit cell depicting the c and $a_{1,2}$ vectors. (b) Directions with hexagonal Miller-bravais indices. The third index t is a dummy index to reinforce analogy with the cubic system i.e. the indices obey $u + v + t = 0$. (c) The link between Miller-Bravais index notation and standard orthogonal cartesian axes xyz. All elastic constant C values are reported with respect to this convention. . . 113

B.1 In these figures, the two orthogonal modes are in red and blue and their phase opposites are in the same color with dashed lines. (a,b) Even-ordered wineglass modes. For $m = 2$, the blue mode has anti-nodes aligned with $\langle 1\,0\,0 \rangle$ directions, while its orthogonal mode (red) has anti-nodes in the $\langle 1\,1\,0 \rangle$ directions. These directions have inequivalent stiffnesses according to (A.25), breaking the degeneracy. For $m = 4$, the mode (blue) has anti-nodes along $\langle 1\,0\,0 \rangle$ and $\langle 1\,1\,0 \rangle$ directions while its orthogonal mode (red) has anti-nodes offset by $\pi/(2m) = 22.5°$, inducing frequency split. (c) Compare this to the $m = 3$ wineglass modes, where the two degenerate modes' anti-nodes are congruent with each other though offset by 30°. For example, the blue mode's anti-nodes at 0°, 120° and 240° are aligned to 0°, 30° and 30° equivalent crystal directions (given cubic crystal symmetry, i.e. modulo(θ, 90°)); the red orthogonal mode's anti-nodes at 90°, 210° and 330° are similarly aligned to 0°, 30° and 30° equivalent crystal directions. This analysis can be continued for higher odd-numbered modes, so despite material anisotropy, odd-numbered modes are inherently degenerate while even-numbered modes are not. 127

C.1 Coordinate transformation using sequential Euler angle rotations α about the z-axis, β about the x-axis and γ about the z-axis. The 6×6 rotation matrix $\boldsymbol{K}$ is shown to the right. 130

LIST OF SYMBOLS AND ABBREVIATIONS

AKE Akhiezer Damping.

ANC Anchor Loss.

ARW Angular Random Walk ($^\circ/\sqrt{\mathrm{h}}$).

BAW Bulk Acoustic Wave.

CMOS Complementary Metal-Oxide Semiconductor.

CTE (α) Coefficient of Thermal Expansion (ppm/K).

CVD Chemical Vapor Deposition.

DFT Density Functional Theory.

DR Dynamic Range.

DRIE Deep Reactive Ion Etching.

EDXS Electron Dispersive X-ray Spectroscopy.

E_G Band Gap (eV).

E_b Breakdown Field (V/m).

FSR ($\Omega_Z|_{max}$) Full Scale Range ($^\circ$/s).

HARPSS High Aspect Ratio Combined Poly and Single Crystal Silicon.

ICP Inductively-Coupled Plasma.

IoT Internet of Things.

LDV Laser Doppler Vibrometer.

LPCVD Low Pressure Chemical Vapor Deposition.

MEMS Microelectromechanical System.

MNEΩ ($\Omega_Z|_{min}$) Mechanical Noise Equivalent Rotation ($^\circ/\mathrm{s}/\sqrt{\mathrm{Hz}}$).

PCB Printed Circuit Board.

PECVD Plasma Enhanced Chemical Vapor Deposition.

ε_0 Free space permittivity (F/m).

ε_r Relative permittivity $\frac{\varepsilon}{\varepsilon_0}$.

PML Perfectly-Matched Layer.

PnC Phononic Crystal.

PolySi Poly Silicon.

Q Quality Factor.

R_m Motional Resistance (Ω).

RLG Ring-Laser Gyro.

RTP Rapid Thermal Processing.

SAM Scanning Acoustic Microscopy.

SCS Single Crystal Silicon.

SEM Scanning Electron Microscopy.

SF Scale Factor (A/(°/s)).

SFD Squeeze-Film Damping.

SiC Silicon Carbide.

SiCOI Silicon Carbide on Insulator.

SOI Silicon on Insulator.

SURF Surface Loss.

TED Thermoelastic Dissipation.

TFG Tuning Fork Gyroscope.

TIA Transimpedance Amplifier.

TMAH Tetramethylammonium Hydroxide.

TSV Through-Silicon Via.

TTV Total Thickness Variation.

ZRO Zero Rate Output.

SUMMARY

This work aims to investigate the suitability and applicability of monocrystalline 4H-silicon carbide (SiC) as a platform for wafer level fabrication of ultra-high Q electrostatic acoustic resonators, including gyroscopic disk resonators. As a semiconductor with a band-gap of 3.2 eV compared to Si's 1.1 eV, SiC is already well explored in the field of power electronics for its electrical and thermal robustness. With respect to mechanical resonators, it possesses salient structural and mechanical dissipation properties, with theoretical $f \cdot Q$ prescribed by quantum mechanical phonon scattering limits surpassing Si by over an order of magnitude. With few exceptions, a high quality factor is universally desirable: improved motional resistance and insertion loss, greater displacements, longer decay times, along with reduced phase and Brownian noise translate to more sensitive, precise and stable instruments.

However, the intersection of theory and reality paint a far more obfuscated picture. At present SiC is more expensive to produce and more difficult to process compared to Si, hindering research and availability to the MEMS community. More specifically, unlike Si which supports high quality oxide growth as a mask material and a well established deep reactive ion etching method in the Bosch process, SiC is not well explored for thick high aspect ratio trenches, limiting researchers to thin film devices which suffer from a myriad of intrinsic and extrinsic complications.

In this work, we delineate the design, fabrication and measurement of resonators fabricated in a custom-made SiC on Insulator (SiCOI) with the aim of achieving ultra-high Q with integrated electrodes. To realize this, we investigate the deep reactive ion etch-

ing of custom-made SiC-on-insulator wafers to achieve aspect ratios in excess of 15:1 in 60 µm-thick SiC device layers with smooth, vertical sidewalls. The centrally-supported disk resonators are anchored upon an acoustically-engineered silicon substrate containing a phononic crystal which suppresses anchor loss and promise Q_{Anchor} in excess of 1×10^9 by design. Optically transduced disk resonators were fabricated, exhibiting $Q = 18 \times 10^6$ at 5.3 MHz, corresponding to $f \cdot Q = 9 \times 10^{13}$ Hz, a five-fold improvement over the Si Akhiezer limit. Integrated high aspect ratio capacitive disk resonators were also fabricated, consistently displaying gyroscopic $m = 3$ modes with Q-factors above 2×10^6 at 6.29 MHz, limited by surface TED due to microscale roughness along the disk sidewalls. Finally, ultra-high Q Lamé mode resonators were fabricated, demonstrating Q of 20×10^6 at 6.27 MHz while also shedding light upon SiC's anisotropic elasticity—specifically the opportunity to extract C_{66} = 203.5 GPa for 4H-SiC wafers sourced from Cree®.

This thesis expounds upon a platform for thick, single crystal silicon carbide resonant MEMS, explores the roots of dissipation and the structural properties most pertinent to bulk acoustic wave resonators and their applications in inertial sensors and instruments. Record measured quality factors $f \cdot Q = 1.25 \times 10^{14}$ Hz—well over Si's Akhiezer limit of 2.3×10^{13} Hz—demonstrate resonators primed for batch fabrication of high performance sensors and instruments. Strong emphasis is placed on developments in fabrication techniques and processes to enable the implementation of SiC in sensors. In summary, this thesis aims to elucidate dissipation, fabrication and anisotropic elasticity in SiC to render device design—from inception to fabrication to measurement—as seamless as possible.

CHAPTER 1

INTRODUCTION AND BACKGROUND

The pursuit of ultra-high quality factors (Q) in micro and nano resonators is of great interest and importance, benefiting a wide range of applications. While ubiquitous, contemporary MEMS gyroscopes fail to satisfy the stringent requirements set forth by the most demanding tasks, e.g. dead reckoning (inertial navigation). However, with sufficiently high Q, batch fabrication of inertial grade MEMS gyroscopes in small planar form factor at wafer level is realizable [1], meeting navigation grade requirements with superior precision and stability (Table 1.1). Currently, a select few types of gyroscopes make the cut: conventional spin-top gyroscopes, quartz hemispherical resonator gyroscopes [2], and Sagnac-effect based optical gyroscopes [3]. However, these solutions are unwieldy, cumbersome, and prohibitively expensive for many applications. Atomic devices are also being investigated [4]. As such, batch fabrication of SiC MEMS gyroscopes becomes extremely attractive. Wafer level production of gyroscopic resonators integrated with electronics promises to reduce footprint, cost and vastly diversify potential applications of inertial grade navigation.

Table 1.1: Gyroscope application grades and typical performance specifications [5, 6].

Specification	Rate Grade	Tactical Grade	Inertial Grade
Angular Random Walk [$^\circ/\sqrt{\text{h}}$]	> 0.5	0.5 – 0.05	< 0.001
Bias instability [°/h]	10 – 1000	0.1 – 10	< 0.01
Bandwidth [Hz]	> 70	100	100
Full scale range [°/s]	50 – 1000	> 500	>400

At present, MEMS inertial sensors are predominantly implemented in silicon largely due to the maturity of its fabrication—particularly at wafer level, with extremely high aspect ratio trenches demonstrated [7]. However, silicon carbide is a promising alternative resonator material as its mechanical performance is exemplary amongst all common substrate materials. Further, SiC is well known for its large Young's modulus, high acoustic velocity, wide bandgap and stable physicochemical properties in harsh environments, enabling a vast array of potential applications [8]. This stability doesn't come without its challenges however, as a consequence of its extremely high bond strength. To wit, SiC etching requires hard metal masks as silicon oxide is difficult to grow, and offers poor selectivity. Conversely, silicon etching requires only silicon oxide which can be grown with quality and patterned with great precision. However, to implement a metal mask requires electroplated, an inherently stressful material with far more trials and tribulations. As such, current SiC trenches have not exceeded 20:1 aspect ratios, precluding bulk micromachining, critical to enabling high performance. While several forms of SiC machining have been demonstrated (laser, molten salts), they lack the finesse required for the highest levels performance. As such, deep reactive ion etching is the most promising method to form trenches with nanoscale precision, revealing a path toward the batch fabrication of navigation grade inertial sensors.

1.1 Resonant Gyroscope Operational Principles

MEMS gyroscopes rely on the Coriolis effect - an inertial force acting on an object that is in motion relative to a rotating reference frame that arises when applying Newton's second law to a rotating frame. For an object with mass $\boldsymbol{m}$ and velocity $\boldsymbol{v}$, the Coriolis force

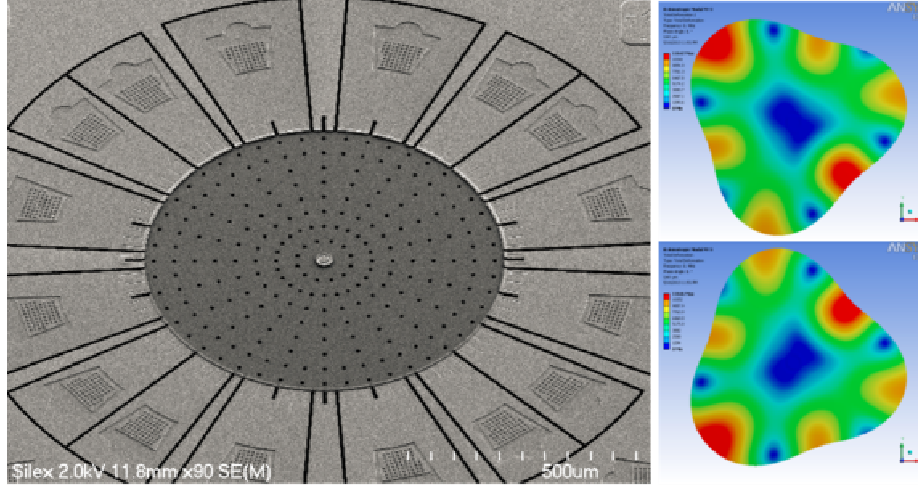

Figure 1.1. *A Qualtré BAW gyroscope with two degenerate $m = 3$ wineglass modes center-supported by a pedestal [9].*

$\boldsymbol{F}$ acting on it under rotation $\boldsymbol{\Omega}$ is:

$$\boldsymbol{F} = -2m\boldsymbol{v} \times \boldsymbol{\Omega} \tag{1.1}$$

Center-supported bulk acoustic wave (BAW) disk resonator gyroscopes use the degenerate $m = 3$ elliptical wine glass modes and the Coriolis force to detect rotation (Figure 1.1). Mode-matched operation, in which the drive and sense modes are degenerate in resonant frequency, offers a path to superior performance. I.e. when a disk vibrating in its drive mode undergoes rotation, the Coriolis force induces a Q-amplified response in the degenerate sense mode (Figure 1.3b).

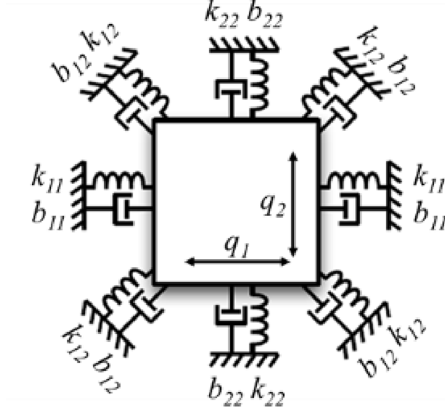

Figure 1.2. *MEMS gyroscope as a two-degree-of-freedom spring-mass system.*

1.1.1 Lumped Parameter Harmonic Motion

Using Newton's second law and the damped harmonic oscillator paradigm:

$$
\begin{aligned}
&F = m\frac{\mathrm{d}^2x}{\mathrm{d}t^2} = -kx - b\frac{\mathrm{d}x}{\mathrm{d}t} \\
&\frac{\mathrm{d}^2x}{\mathrm{d}t^2} + 2\zeta\omega_0 + \omega_0^2 x = 0
\end{aligned}
\tag{1.2}
$$

where the damping term $\zeta = b/(2\sqrt{mk}) = 1/(2Q)$ and the undamped angular frequency $\omega_0 = \sqrt{k/m}$. Adapting this model for a MEMS gyroscope as a two degree-of-freedom spring-mass system (Figure 1.2), the coupled second-order differential equations describing the disk gyroscope are expressed as follows [10]:

$$
m_{11}\ddot{q}_1(t) + b_{11}\dot{q}_1(t) + k_{11}q_1(t) = \sum_{i=1}^{k} f_{1,i} - 2\lambda m_{22}\Omega(t)\dot{q}_2 \tag{1.3a}
$$

$$
m_{22}\ddot{q}_2(t) + b_{22}\dot{q}_2(t) + k_{22}q_2(t) = \sum_{j=1}^{l} f_{2,i} - 2\lambda m_{11}\Omega(t)\dot{q}_1 \tag{1.3b}
$$

where m is the effective modal mass, b is the damping coefficient, k is the effective modal stiffness, λ is the angular gain[1], Ω is the angular velocity, and q_1 and q_2 are generalized translational coordinates for the two degenerate modes, respectively (Appendix B).

Utilizing the gyro as a rotation-rate sensor involves exciting the drive-mode into resonance and subsequently sensing Coriolis-coupled vibration in the sense-mode. The drive-mode (generalized coordinate q_1) transfer function is given by:

$$\ddot{q}_1 + \frac{\omega_{0_1}}{Q_1}\dot{q}_1 + \omega_{0_1}^2 q_1 = \frac{f_d(t)}{m_{11}} \tag{1.4}$$

with the assumption that any Coriolis-coupling from the sense mode is neglected, achievable using feedback electronics in the drive loop to keep the maximum displacement q_1 constant. Transforming (1.4) to the s-domain and solving for q_1 yields:

$$\frac{q_1(s)}{f_d(s)} = \frac{1}{m_{11}} \frac{1}{s^2 + \frac{\omega_{0_1}}{Q_1}s + \omega_{0_1}^2} \tag{1.5}$$

Given the prior assumption of feedback control for the drive loop, we can neglect the decay parameter σ within $s = \sigma + j\omega$. Thus, replacing s by $j\omega$ and separating for the real and imaginary parts:

$$\mathrm{Re}\left(\frac{q_1(j\omega)}{f_d(j\omega}\right) = \frac{1}{m_{11}} \frac{\omega_{0_1}^2 - \omega^2}{\omega^4 + 2(\frac{1}{2Q_1^2} - 1)\omega_{0_1}^2\omega^2 + \omega_{0_1}^4} \tag{1.6a}$$

$$\mathrm{Im}\left(\frac{q_1(j\omega)}{f_d(j\omega}\right) = \frac{-1}{Q_1 m_{11}} \frac{\omega_{0_1}\omega^2}{\omega^4 + 2(\frac{1}{2Q_1^2} - 1)\omega_{0_1}^2\omega^2 + \omega_{0_1}^4} \tag{1.6b}$$

[1]This is a measure of energy transfer with values from zero to one; the displacements in the gyroscopic elliptical modes are not entirely radial with some energy being transferred to shear displacement [11]

When excited at resonance i.e. the driving frequency $\omega = \omega_{0_1}$, the real component (1.6a) goes to zero and the imaginary component of displacement (1.6b) becomes maximal. In other words, displacement q_1 is $-90°$ out of phase with driving force f_d:

$$\left|\frac{q_1}{f_d}\right|_{\omega=\omega_{0_1}} = \frac{Q_1}{m_{11}\omega_{0_1}^2} \qquad \angle \left.\frac{q_1}{f_d}\right|_{\omega=\omega_{0_1}} = -90° \tag{1.7}$$

With the drive mode driven into resonance with displacement $q_1(t)$, the sense mode will respond to any non-zero rotation $\Omega(t)$[2] with angular gain λ:

$$\ddot{q}_2 + \frac{\omega_{0_2}}{Q_2}\dot{q}_{2c} + \omega_{0_2}^2 q_{2c} = 2\lambda\Omega\dot{q}_1 \tag{1.8}$$

Solving (1.8) in the s-domain and evaluating ω at the drive mode resonance frequency ω_{0_1} yields the transfer function of the Coriolis-induced displacement of the sense mode (q_{2c}) to the displacement of the drive mode (q_1):

$$\mathrm{Re}\left(\frac{q_{2c}}{q_1}\right)_{\omega=\omega_{0_1}} = \frac{2\lambda}{Q_2}\frac{\omega_{0_2}\omega_{0_1}^2}{\omega_{0_1}^4 + 2(\frac{1}{2Q_2^2} - 1)\omega_{0_2}^2\omega_{0_1}^2 + \omega_{0_2}^4}\Omega \tag{1.9a}$$

$$\mathrm{Im}\left(\frac{q_{2c}}{q_1}\right)_{\omega=\omega_{0_1}} = 2\lambda\frac{\omega_{0_1}(\omega_{0_2}^2 - \omega_{0_1}^2)}{\omega_{0_1}^4 + 2(\frac{1}{2Q_2^2} - 1)\omega_{0_2}^2\omega_{0_1}^2 + \omega_{0_2}^4}\Omega \tag{1.9b}$$

Equations (1.9) reveal that the sense response is a strong function of frequency split $\Delta\omega = |\omega_{0_1} - \omega_{0_2}|$. Typical tuning fork gyroscopes operate under mode-split condition, where $\omega_{0_1} \neq \omega_{0_2}$. In particular, taking the case where $\omega_{0_1} \ll \omega_{0_2}$, the real component of the sense response disappears leaving only the imaginary component with magnitude and

[2] It's assumed here that Ω is quasi-static, a fair assumption given that rotation rate bandwidths rarely exceed hundreds of Hz whereas device operating frequencies are regularly in excess of tens of kHz

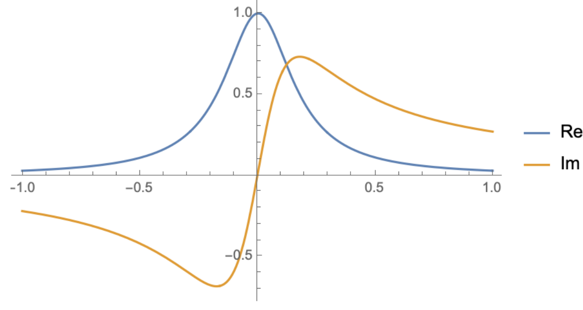

(a)

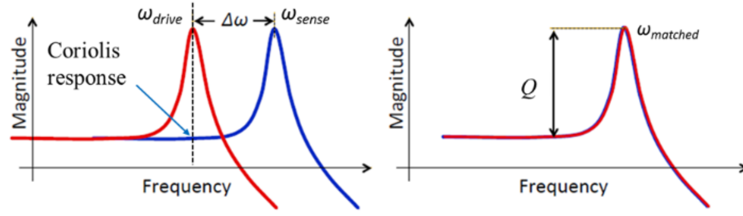

(b)

Figure 1.3. *(a) Normalized real and imaginary responses* (1.9) *as a function of frequency split. The peak's sharpness is defined by Q_2. (b) Sense response of mode-split (left) and mode-matched (Q-amplified, right) gyroscopes.*

phase:

$$\left|\frac{q_{2c}}{q_1}\right|_{\omega_{0_1} \ll \omega_{0_2}} = \frac{2\lambda\omega_{0_1}}{\omega_{0_2}^2}\Omega \qquad \angle \left.\frac{q_{2c}}{q_1}\right|_{\omega_{0_1} \ll \omega_{0_2}} = -90° \tag{1.10}$$

However, if operating under mode-matched conditions as is the case with axi-symmetric disk gyroscopes, with $\omega_{0_1} = \omega_{0_2}$, the imaginary component vanishes and the response becomes instead:

$$\left|\frac{q_{2c}}{q_1}\right|_{\omega_{0_1} = \omega_{0_2}} = \frac{2\lambda Q_2}{\omega_{0_1}}\Omega \qquad \angle \left.\frac{q_{2c}}{q_1}\right|_{\omega_{0_1} = \omega_{0_2}} = 0° \tag{1.11}$$

Critically, the sense response is Q-amplified, certainly advantageous during operation. Figure 1.3a shows the sense to drive displacement ratio with as a function of the frequency split.

1.1.2 Disk Gyroscope Electrical Transduction Performance Metrics

In order to electrically characterize a gyroscope, we need to adapt the mechanical assessment of an axi-symmetric gyroscope as described in subsection 1.1.1 to the electrical domain. This section will describe and present relevant performance metrics without comprehensive derivation and with a focus on quality factor Q [12]. A thorough treatment—including remarks on electrostatic tuning for mode-matching and quadrature cancellation—can be found in [13, 10].

Motional Resistance (R_m) An AC signal at the input drive electrode will induce mechanical vibration $-90°$ out of phase. The motional impedance is the ratio of the current at the pickoff electrode to the input drive signal v_d. To first order, the force exerted by v_d on a body polarized to V_P is:

$$f_d \approx \frac{\varepsilon A}{2g_0^2}(v_d^2 - 2v_d V_P + V_P^2) \tag{1.12}$$

Assuming that excitation is at resonance ($v_d = V_d \sin(\omega_{0_1} t + \phi)$) and neglecting the off resonance terms (v_d^2 and V_P^2), One can recast (1.7) with (1.12) to yield displacement q_1 with respect to excitation voltage:

$$\left|\frac{q_1}{v_d}\right|_{\omega=\omega_{0_1}} = \frac{Q_1}{m_{11}\omega_{0_1}^2}\frac{\varepsilon A V_P}{g_0^2} \qquad \angle \left.\frac{q_1}{v_d}\right|_{\omega=\omega_{0_1}} = 90° \tag{1.13}$$

To first order (i.e. if $q < 10\%$ of the gap), the output drive electrode capacitance will

change as a function of gap distance as given by:

$$\Delta C \approxeq -\frac{\varepsilon_o hR}{g_0}\left[\frac{2q_1 \sin\left(\frac{3\Delta\theta_n}{2}\right)}{3g_0} - \left(\frac{q_1}{g_0}\right)^2 \left(\frac{\Delta\theta_n}{2} + \frac{\sin(3\Delta\theta_n)}{6}\right)\right] \tag{1.14}$$

where $\Delta\theta_n$ is the span of the electrode, R is the disk radius, h is the disk thickness, and g_o is the gap. Modeling the gap as a parallel plate capacitor[3], and with constant polarization voltage V_P, the current is given by:

$$\begin{aligned} i_d &= \frac{\mathrm{d}Q}{\mathrm{d}t} = \frac{\mathrm{d}CV_P}{\mathrm{d}t} \\ &= \frac{\partial CV_P}{\partial V_P}\cancelto{0}{\frac{\mathrm{d}V_P}{\mathrm{d}t}} + \frac{\partial CV_P}{\partial C}\frac{\mathrm{d}C}{\mathrm{d}t} \\ &= V_P \frac{\partial C}{\partial q_1}\frac{\mathrm{d}q_1}{\mathrm{d}t} \end{aligned} \tag{1.15}$$

Substituting (1.7) and the first term of (1.14) into (1.15) and taking care of the phase differences, gives us the current in terms of drive voltage:

$$\left|\frac{i_d}{v_d}\right|_{\omega=\omega_{0_1}} = \frac{Q_1}{m_{11}\omega_{0_1}^2}\left(\frac{\frac{2}{3}\varepsilon hR\sin\left(\frac{3\Delta\theta_n}{2}\right)V_P}{g_0^2}\right)^2 \omega_{0_1} \qquad \angle \left.\frac{i_d}{v_d}\right|_{\omega=\omega_{0_1}} = 180^\circ \tag{1.16}$$

Inverting this equation gives the motional resistance (R_m) of the resonator, a measure of the equivalent resistance that the drive-loop electronics need to overcome:

$$R_m = \frac{v_d}{i_d} = \frac{\omega_{0_1} m_{11}}{Q_1}\left(\frac{g_0^2}{\frac{2}{3}\varepsilon hR\sin\left(\frac{3\Delta\theta_n}{2}\right)V_P}\right)^2 \tag{1.17}$$

[3]While not strictly correct, if the span $\Delta\theta_n \leq 30^\circ$, this approximation rings true.

Scale Factor (SF) Through analysis similar to motional resistance, the Coriolis force-induced scale factor as a function of rotation-rate Ω for one pair of drive and sense electrodes is:

$$\left|\frac{i_s}{\Omega}\right|_{\omega=\omega_{0_1}} = 2\lambda Q_2 \left(\frac{\frac{2}{3}\varepsilon h R \sin\left(\frac{3\Delta\theta_n}{2}\right) V_P}{g_0^2}\right) q_1 \qquad \angle \left.\frac{i_s}{\Omega}\right|_{\omega=\omega_{0_1}} = 90^\circ \tag{1.18}$$

Full Scale Range (FSR) In a parallel plate capacitor, (1.14) assumes that displacement remains linear and doesn't exceed ten percent of the nominal gap. Thus, replacing the sense-mode displacement q_{2_c} with $0.1 \times g_0$ gives the full scale range:

$$\Omega_Z|_{max} = \frac{g_0}{20} \frac{\omega_{0_1}}{2\lambda Q_2 q_1} \tag{1.19}$$

Mechanical Brownian Noise ($MNE\Omega$) Brownian mechanical vibration sets the fundamental limit for noise performance in a gyroscope [14] and can be modeled by an ersatz noise force proportional to the sense mode's damping ($F = \sqrt{4k_B T R}$). For a mode-matched gyroscope, equating this force to the Coriolis force gives:

$$\left|q_{2,Brownian}\right| = \sqrt{\frac{4k_B T Q_2}{m_{22}\omega_0^2}} \tag{1.20a}$$

$$MNE\Omega = \Omega_Z|_{min} = \frac{1}{\lambda q_1}\sqrt{\frac{k_B T}{Q_2 m_{22} \omega_0}} \tag{1.20b}$$

where the mechanical noise equivalent rate is in units of $\mathrm{rad/s}/\sqrt{\mathrm{Hz}}$.

1.2 Thesis Organization

A menagerie of sensors and instruments benefit nearly categorically from improved Q affecting a wide variety of performance specifications. With further investigation into silicon carbide's material properties and nanoscale precision machining, silicon carbide and its superb mechanical properties are poised to make waves in the high performance, extreme environment sensors and instruments space. As such, this thesis will focus on engineering silicon carbide to maximize Q in the batch fabrication of thick monocrystalline 4H-SiC on insulator. Chapter 2 will focus on dissipation mechanisms as they pertain to silicon carbide bulk acoustic wave resonators. Chapter 3 will detail advances in batch-fabrication of silicon carbide resonators within the silicon carbide on insulator platform. Chapter 4 will describe the design and measured results of bulk acoustic wave elliptical modes in disk resonators, whereas Chapter 5 will focus on square resonators suitable for achieving ultra-high Q. Finally, Chapter 6 will delineate contributions of this work to the field of resonant silicon carbide MEMS devices and their fabrication as well as outline avenues of research and development.

CHAPTER 2

DISSIPATION IN SILICON CARBIDE BULK ACOUSTIC WAVE (BAW) RESONATORS

Naturally, achieving high Q factor is almost categorically desired, benefiting the device's noise, stability, and performance. With very few exceptions, high Q enables devices to produce highly pure spectral oscillations with long decay times enabling far lower power consumption. Generally speaking, acoustic MEMS devices operate at much higher quality factors than their electrical counterparts and are well suited to take advantage of high Q and the performance enhancements it confers.

As there is an insurmountable array of intrinsic and extrinsic physical phenomena that play a role in a resonator's Q-factor, each of which can warrant fine-combed scrutiny and intensive research and development. That said, this chapter will focus largely on those affecting the design and fabrication of bulk acoustic wave resonators in thick monocrystalline silicon carbide.

2.1 Measuring Quality Factor (Q)

The most general definition of Q incorporates the fractional dissipation of energy per second [15]:

$$Q = 2\pi f \left| \frac{W_{sys}}{\dot{W}_{sys}} \right| \tag{2.1}$$

where f is the operating frequency, W_{sys} is the energy contained within the resonator, and $\dot{W}_{sys}$ is the rate at which energy leaves the system. There are several ways to characterize

quality factor, the most suitable of which depends drastically on the conditions of the experiment.

Ringdown One may measure Q via the ring-down method, analyzing the decay rate of the resonator's periodic harmonic motion in the time domain [16]. To wit, the solution of the homogeneous second order damped harmonic oscillator takes the general form:

$$u(t) = \underbrace{u_{max} e^{-\frac{\omega}{2Q}t}}_{\text{envelope}} \underbrace{\cos\left(\omega t \sqrt{1 - \frac{1}{4Q^2}} + \phi\right)}_{\text{harmonic motion}} \tag{2.2}$$

where u is the displacement, ω is the angular frequency, and ϕ is an arbitrary phase shift which we will take to be zero. The displacement is composed of two parts, the envelope representing the maximum displacement at time t and the harmonic motion itself (Figure 2.1). After being excited to resonant harmonic motion, the transient response after cessation of the driving force can reveal the quality factor. I.e. at a time $\tau = 2Q/\omega$, the displacement u will have decayed to a factor of $1/e$ times the maximum displacement. Therefore Q can be derived in the following way:

$$Q = \frac{\omega \tau}{2} \tag{2.3}$$

This method can be rather cumbersome to wield especially when contending with the high-frequency/low-displacement devices encountered in this work. It requires an appropriately high signal-to-noise ratio with minimal thermal and background vibration; in the case of capacitive transduction, parasitic capacitances from the device and feedthrough from the

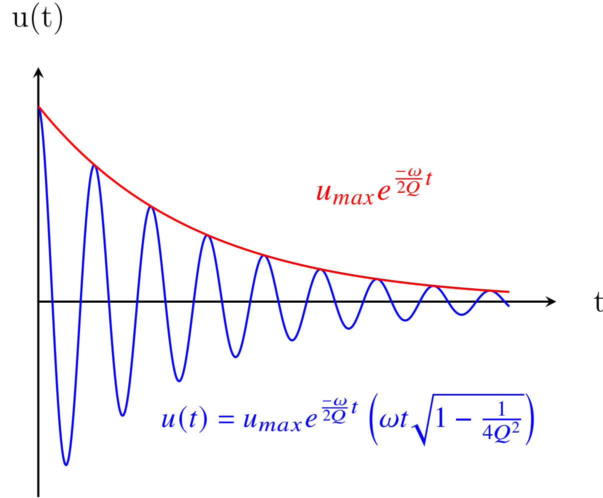

Figure 2.1. *A time domain plot of the displacement of a damped harmonic oscillator with quality factor Q and angular frequency ω. The exponential decay curve (blue) envelopes the damped periodic motion (red). By determining the time τ at which $u(\tau) = 1/e$, one can extract the quality factor Q via* (2.3).

test printed circuit board (PCB) must also be minimized.

3 dB Bandwidth An alternative measure of Q that illustrates the peak's sharpness is by analyzing the intensity of resonance which takes the form of the Lorentzian distribution [15]:

$$I(\omega) \propto \frac{1}{(\omega - 2\pi f_{res})^2 + \left(\frac{\Gamma}{2}\right)^2} \tag{2.4}$$

where Γ is the linewidth of resonance, inversely proportional to Q. Applicable to low-dissipation devices, it relates the resonance frequency to the 3 dB bandwidth, i.e. where the intensity is at half-maximum:

$$Q = \frac{f_{res}}{\Delta f_{-3dB}} \tag{2.5}$$

Incidentally, Q can also be determined via the slope of the phase, $\phi(\omega)$, as the excitation

traverses the resonance frequency [17]:

$$Q = \frac{\omega_0}{2} \left| \frac{\partial \phi}{\partial \omega} \right|_{\omega=\omega_0} \tag{2.6}$$

Evidently, (2.3) and (2.5) indicate that high Q enables resonant devices to produce spectrally pure oscillations in tandem with long decay times. With few exceptions, higher Q enables increased sensitivities with decreased power consumption in many resonant MEMS devices. In other words, resonant MEMS devices are designed specifically to take advantage of the high Q offered by acoustic or mechanical vibration.

2.2 Dissipation in Silicon Carbide MEMS Resonators

A MEMS resonator's quality factor is dependent on many physical phenomena, each contributing to Q [18]:

$$\frac{1}{Q_{Total}} = \frac{1}{Q_{TED}} + \frac{1}{Q_{ANC}} + \frac{1}{Q_{SFD}} + \frac{1}{Q_{PhPh}} + \sum_i \frac{1}{Q_i} \tag{2.7}$$

These dissipation mechanisms affecting Q can be categorized as either intrinsic (material dependent) or extrinsic (Table 2.1). While extrinsic mechanisms such as energy dissipated through the anchor (ANC) and squeeze/slide film damping (SFD) can be mitigated by clever design [19], intrinsic mechanisms like thermoelastic dissipation and fundamental quantum losses (PhPh) set the ultimate limit on Q.

Table 2.1: Prominent MEMS dissipation mechanisms [20]

Dissipation Mechanism	Intrisicality
Phonon-Phonon Interaction (Q_{PhPh})	Intrinsic
Phonon-Electron Interaction (Q_{PhEl})	Intrinsic
Acoustic Thermoelastic Dissipation (Q_{TED})	Intrinsic
Bulk Modal Thermoelastic Dissipation ($Q_{BulkTED}$)	Extrinsic
Impurity/Defect/Dislocation/Isotope/Vacancy Scattering	Quasi-Intrinsic
Surface/Interfacial Loss (Q_{SURF})	Extrinsic
Anchor/Support Loss (Q_{ANC})	Extrinsic
Air/Squeeze Film Damping (Q_{SFD})	Extrinsic
Surface TED ($Q_{SurfTED}$)	Extrinsic
Dielectric Loss (Q_{Diel})	Extrinsic
Electrical/Resistive Loss (Q_{Elec})	Extrinsic

2.3 Intrinsic Dissipation Mechanisms

2.3.1 Dissipation due to Phonon-Phonon Interactions (AKE)

Q_{PhPh} (Phonon-Phonon) represents fundamental phonon-phonon interactions and the ultimate limit of Q. When the phonon distribution is perturbed from its equilibrium Planck distribution by an acoustic wave, normal and Umklapp scattering with thermal phonons acts to bring the distribution back to equilibrium [20]. This is depicted in Figure 2.2 as a perturbation away from the equilibrium distribution of thermal phonons.

Physically, one may envision phonon-phonon dissipation as an acoustic wave propagation interacting with latent thermal lattice vibrations (thermal phonons). At low temperatures with low phonon occupation, interaction is minimal, and other mechanisms may dominate dissipation. However, at high temperature and more fervent lattice vibrations, greater probability of scattering with the acoustic wave leads to increased energy dissipation. The polarization of the wave can significantly influence this interaction; in general, longitudinal waves experience attenuation approximately ten times larger than that of shear waves [22].

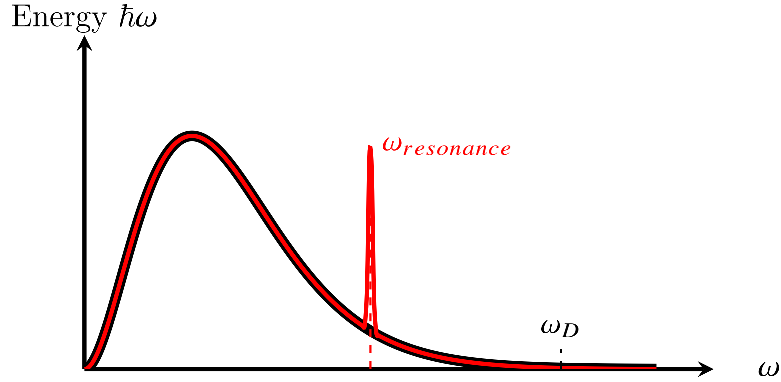

Figure 2.2. *The acoustic wave is modeled as a perturbation of a large number of coherent phonons (red peak at $\omega_{resonance}$) disturbing the thermal Planck spectral energy equilibrium (black). Through entropy-producing processes, collision and scattering with thermal phonons will tend the distribution back to thermal equilibrium [21]. The Debye frequency ω_D is the frequency of highest occupancy; contrary to photons which can have infinite frequency, phonons exist in finite lattice spacing and cannot support infinitesimally small wavelengths.*

This is relevant for the subsequent discussion of square resonators in Chapter 5.

Phonon dissipation is typically categorized based on the length of the acoustic wave relative to the thermal phonons' mean free paths and how it interacts with the sea of phonons. In the case where the wavelength is long, the wave is regarded as a macroscopic strain field in the crystal, interacting with the entire population of phonons. Described by Akhiezer [23], scattering and subsequent relaxation to thermal equilibrium is treated via phonon Boltzmann transport [24]. Conversely, Landau and Rumer provide an alternative approach [25], in which the acoustic wavelength is on the order of the mean free path and interacts directly with individual lattice phonons. In this thesis, resonators lie in the Akhiezer regime where vibrational period of the lattice distortion (τ_v) greatly exceeds the mean phonon scattering time (τ_s); thus, attention will be focused upon Akhiezer damping. That said, at high-frequency vibrations where $\tau_s > \tau_v$, scattering is unable to alter the phonon distribution and dissipation can largely be suppressed [26].

In the Akhiezer damping model, the applied strain and change in atomic periodicity due to an elastic wave modulates the phonon dispersion curve and the local phonon equilibrium. As phonon cannot change instantaneously, they will relax towards the modulated equilibrium distribution via phonon-phonon scattering when the thermal relaxation time (τ) is significantly shorter than the mechanical wave's period. This relaxation produces entropy and consumes the elastic wave's energy, first described by Akhiezer [23]. Using the Boltzmann transport equation, Akhiezer loss can be derived containing only classical, bulk properties [27]:

$$f \cdot Q = \frac{3\rho c^2}{2\pi\gamma_{avg}^2 c_v T\tau} = \frac{\rho c^4}{2\pi\gamma_{avg}^2 kT} \tag{2.8}$$

In this expression, γ_{avg} is the average Grüneisen parameter, c_v is the specific heat at constant volume, T is ambient temperature, c is the average acoustic speed, k is the thermal conductivity and τ is the scattering time. Maris provides a more complete analysis, incorporating both elastic and inelastic collisions, resulting in an expression for Q with an additional term relating the period and the time-scale for scattering:

$$Q = \frac{\rho c^2}{2\pi\gamma^2 c_v T}\frac{1 + (f\tau)^2}{f\tau} \tag{2.9}$$

While not a final picture of phonon-phonon dissipation, this provides an order-of-magnitude measurement that motivates this work and the use of silicon carbide as a resonator material. As shown in Figure 2.3 and Table 2.2, silicon carbide possesses an Akhiezer limit vastly eclipsing other common MEMS materials and nearly thirty times higer than silicon.

Table 2.2: Akhiezer limit $f \cdot Q$ of common resonator materials and relevant material properties.

Mat.	γ_{avg}	c_v [J/(kg K)]	k [W/(cm K)]	ρ [kg/m^3]	$f \cdot Q$ [× 10^{13}]
Silicon	0.51	700	1.3	2320	2.3
Fused Silica	0.87	740	0.014	2202	3.2
AlN	0.91	600	2.85	3255	2.5
Diamond	0.94	657	22	3510	3.7
Sapphire	1.1	570	0.35	3980	11.3
SiC	0.3	690	3.7	3230	64

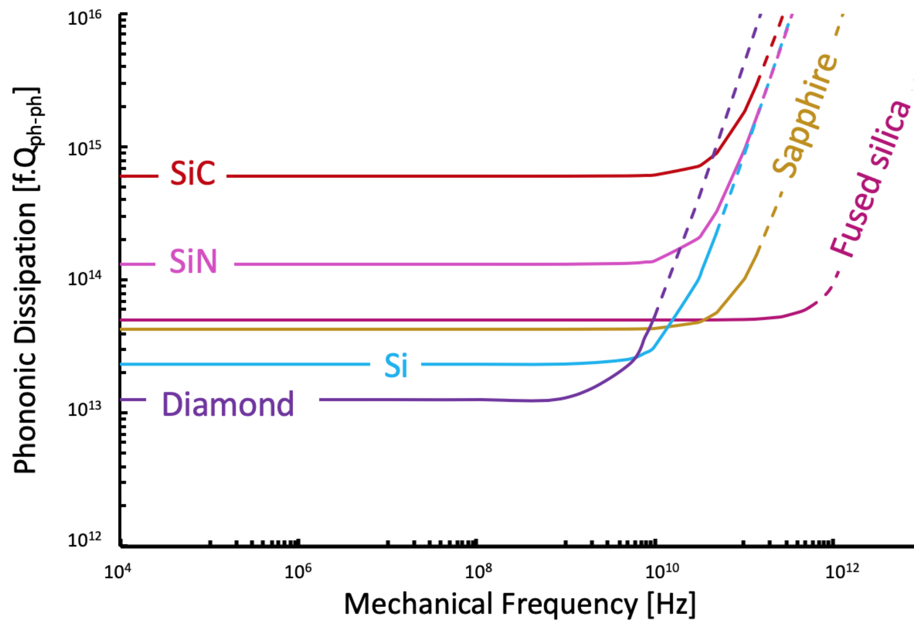

Figure 2.3. *With respect to Akhiezer damping, silicon carbide is a superior mechanical material. The bend in the curves represents the transition to the Landau-Rumer regime of dissipation, well above our frequencies of interest.*

2.3.2 Thermoelastic Dissipation (TED)

Thermoelastic dissipation (TED) occurs in any resonator material that experiences thermal expansion. I.e. when the resonator undergoes mechanical deformation, energy flows from regions of compressive (cold) and tensile (hot) stress [28]. Difficult to quantify analytically, a closed-form expression exists only for a cantilever as derived by Zener [29]:

$$\frac{1}{Q_{TED}} = \underbrace{\frac{\alpha^2 ET}{c_v}}_{\text{material term}} \underbrace{\frac{\omega\tau_{th}}{1 + (\omega\tau_{th})}}_{\text{frequency term}} \tag{2.10}$$

where α is the coefficient of thermal expansion of the material, E is the Young's modulus, c_v is the heat capacity per unit volume, ω is the resonator's mechanical frequency, and τ_{th} is the thermal diffusion time. Split into two parts, the first term encapsulates the material contribution whereas the second term captures the frequency dependence of the resonant motion. Three regimes exist: isothermal, adiabatic, and Debye [30]. If the mechanical period is greater than the thermal relaxation time ($\omega\tau_{th} \ll 1$), the resonator is said to behave isothermally, as thermal equilibrium is easily maintained across the resonator, energy transfer is limited and dissipation is inhibited. Conversely, if $\omega\tau_{th} \gg 1$, the behavior is adiabatic as there is insufficient time for energy transfer before tensile regions deform back to compressive regions and vice versa. Lastly, if $\omega\tau_{th} \approx 1$, the resonator operates in the Debye regime and dissipation is maximal as strain and stress are out of phase and a maximum of internal friction occurs. Common flexural mode TFGs operate in the Debye regime, limiting their Q (Figure 2.4). However, BAW resonators operate adiabatically, placing the Q limit much higher.

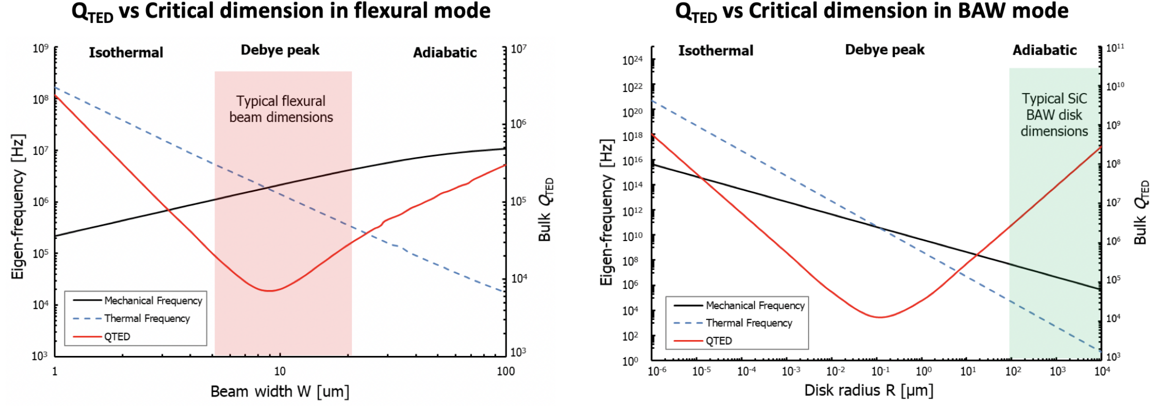

Figure 2.4. *Tuning fork gyros operate in the Debye regime where the thermal frequency lies near the resonant mechanical frequency. In contrast, BAW resonators operate adiabatically, allowing for much higher Q factors.*

To model TED, we introduce the concept of thermal modes [31], the eigen-solutions to the homogeneous heat diffusion equation:

$$k\nabla^2 T = c_v \frac{\partial T}{\partial t} \tag{2.11}$$

Separation of variables leads to the Helmholtz equation:

$$k\nabla^2 v_i(x,y,z) + \lambda_i c_v v_i(x,y,z) = 0, \int_V v_i(x,y,z) d\Omega = V \tag{2.12}$$

where v_i is the eigensolution and λ_i is the eigenfrequency. These v_i of Eq. (2.12) are referred to as thermal modes. Naturally, we can use these eigenvalues as the basis to expand solutions of the heat equation Eq. (2.11), where each eigenfrequency λ_i represents the characteristic decay time of the corresponding eigenmode v_i.

Deformation contributes a heat source term and modifies Eq. (2.11) accordingly [32]:

$$c_v \frac{\partial T}{\partial t} = k\nabla^2 T - \underbrace{3\alpha BT \left[\frac{\partial}{\partial t}\left(\frac{\delta V}{V}\right)\right]}_{\text{heat source}} \tag{2.13}$$

where α is the thermal expansion coefficient, B is the bulk modulus and $\frac{\partial}{\partial t}(\frac{\delta V}{V})$ is the rate of change in volume. If the change in temperature is insignificant relative to the bath reservoir, the heat source term is largely independent of the temperature change to first order. Thus, a linear transformation $T = T_{reservoir} + \theta$ yields the following equation:

$$c_v \frac{\partial \theta}{\partial t} = k\nabla^2 \theta - 3\alpha BT_{reservoir} \left[\frac{\partial}{\partial t}\left(\frac{\delta V}{V}\right)\right] \tag{2.14}$$

Ultimately, using general form of the time harmonic solution to the vibration equation allows us to express the heat source term in Eq. (2.14) as a product of a spatial term and a time harmonic term:

$$q = \underbrace{-3\alpha BT_{reservoir}\omega\varepsilon_V(x,y,z)}_{\text{spatial component}} \quad \times \quad \underbrace{\cos(\omega t)}_{\text{temporal component}} \tag{2.15}$$

where ε_V is the volumetric strain of the solid. Projecting the spatial component of q onto the thermal modes (v_i) of the system gives:

$$\begin{aligned} q &= \sum 3\alpha BT_{reservoir}\varepsilon_V(x,y,z)\omega a_i v_i(x,y,z) \\ &= \sum 3\alpha BT_{reservoir}\omega \underbrace{\left(\frac{1}{3\alpha BT_{reservoir}\omega}\frac{\int_V q(x,y,z)v_i(x,y,z)d\Omega}{\int_V v_i^2(x,y,z)d\Omega}\right)}_{a_i} v_i(x,y,z) \end{aligned} \tag{2.16}$$

Critically, the magnitude of the overlap integral a_i depends on the overlap of the spatial strain with the thermal mode. I.e. for a given mechanical strain distribution, its conflation with the thermal modes v_i will determine heat transfer q. Physically, one may intuit this as regions of compressive/tensile strain interacting with thermal pathways. As heat transfer results in entropy generation, further manipulation returns a general expression for the thermoelastic quality factor of a multi thermal mode system:

$$Q^{-1} \propto \sum_i a_i^2 \left(\frac{\alpha^2 E T_{reservoir}}{c_v} \frac{\omega \lambda_i}{\omega^2 + \lambda_i^2} \right) \tag{2.17}$$

Note that the term inside parentheses is equivalent to Eq. (2.10), Zener's expression for modal quality factor. We can see that quality factor is due to the interaction of the mechanical strain and its overlap with the thermal eigenmodes of the heat diffusion equation. Through COMSOL simulations and numerical computation, one may estimate and visualize the thermal eigenmodes and the strain of an arbitrary geometry. Diagrammatically this is depicted in Figure 2.5 for the $m = 3$ elliptical mode of a solid disk and in Figure 2.6 for a fixed-fixed beam. The beam exhibits significant TED as a confluence of significant modal overlap as well as operation in the Debye regime. However, the disk's mechanical strain interacts most heavily with the zeroth thermal eigenmode with $v_0 = 1$ and $\lambda_0 = 0\,\text{Hz}$, resulting in minimal dissipation. However, the introduction of release holes creates a multiplicity of strain sites, greatly exacerbating TED even in bulk resonators [33] and will be explored in subsequent chapters.

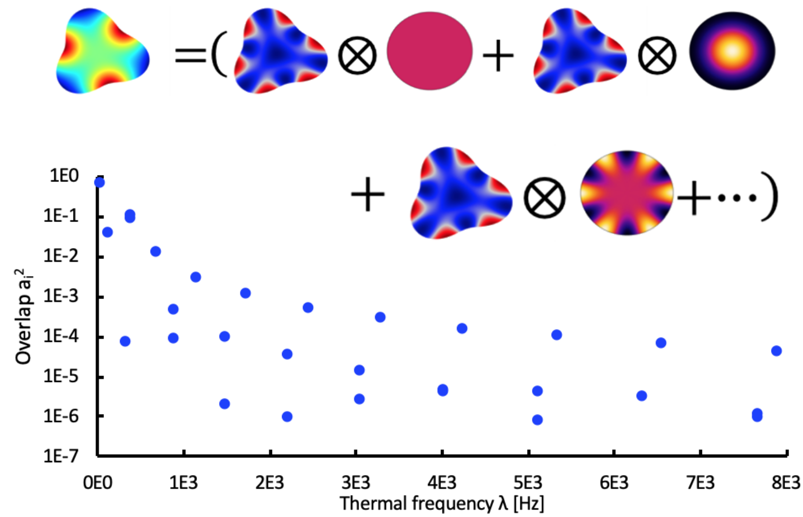

Figure 2.5. *The TED of a resonant mode can be modeled as the sum the overlap between the mechanical strain and thermal modes of the mode. In the case of the disk, there is a large overlap between the mechanical strain and the first thermal mode which has $\lambda = 0$, resulting in no dissipation.*

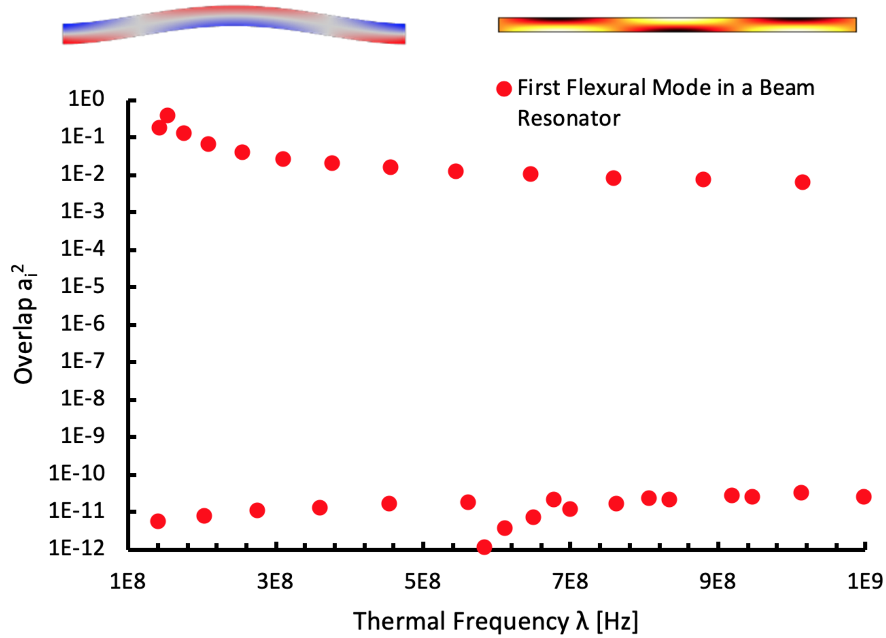

Figure 2.6. *The mechanical strain (top left) of the fundamental mode for a fixed-fixed cantilever beam interacts heavily with a thermal eigenmode (top right), resulting in large overlap integrals (red dots) and subsequently much higher TED. The alternating dots correspond to odd (high) and even (low) thermal eigenmodes.*

2.4 Extrinsic Dissipation Mechanisms

Extrinsic mechanisms describe dissipation pertaining to non-idealities in design; some such as anchor loss are necessary but in many cases can be cleverly mollified.

2.4.1 Anchor and Support Losses (ANC)

Q_{ANC} represents losses through the anchor of the device to the environment and is generally the most conspicuous loss mechanism for BAW devices. Ideally, the anchor is an infinitesimally small point forbidding strain energy from escaping the device. While shrinking the size of the pedestal support monotonically reduces anchor losses, clearly it cannot be made excessively small to ensure resilience against shock and vibration. Similarly, elongation of the pedestal offers a measure of isolation, again compromising structural integrity. In BAW disk resonators, anchor losses arise principally due to the material's anisotropy; the wineglass modes exhibit an asymmetric shear deformation, leading to elastic waves propagating down the pedestal and lost through the handle layer. Though analytical expressions have been derived, their utility is somewhat lacking. As bulk acoustic wave modes operate at high frequency, one can use perfectly matched layer simulations can give a lower bound of Q_{ANC} and should be liberally applied during design of high frequency resonators. To address anchor loss, prior work has implemented substrate-decoupling elements in the device layer to "levitate" the disk (Figure 2.7) [19, 34]; however, this comes at the expense of increased TED due to additional strain at the sites of the occlusions.

Other decoupling methods that have been demonstrated in the past place structures exterior to the body of the resonator to inhibit spurious modes and confine energy within

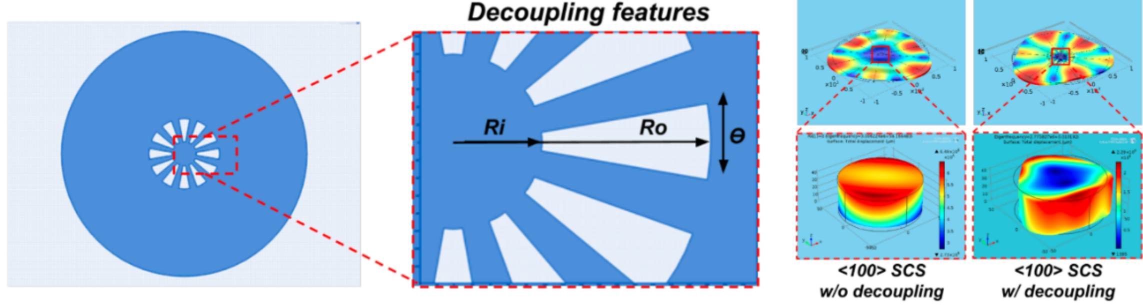

Figure 2.7. *Substrate decoupling for disk gyroscopes. Without decoupling features, large shear deformation is found at the anchor. Introducing substrate-decoupling features greatly mitigates deformation at the anchor, obstructing losses through the pedestal [19].*

it. For example, in lateral mode AlN-on-Si resonators, an array of coupled-ring structures– carefully designed to create a phononic bandgap surrounding the resonant frequency– improves Q factors by orders of magnitude over the same resonator simply anchored to the environment [35, 36]. This form of decoupling keeps the resonator free from defects or occlusions that enhance thermoelastic dissipation or could lead to spurious modes, creating a lossy resonator.

2.4.2 Other Dissipation Mechanisms

Squeeze-Film Damping Scaling laws down to the microscale conspire to make surface effects such as squeeze-film damping (Q_{SFD}) significant in MEMS applications and in fact, do represent a major source of loss [37, 38]. A key parameter when discussing squeeze-film damping is the cut-off frequency, where the viscous damping force equals the elastic force of the resonator [39]:

$$\omega_c = \frac{\pi^2 h_o^2 p_a}{12\mu W^2} \tag{2.18}$$

where h_o is the gap at steady-state, p_a is the ambient pressure, μ is the shear viscosity of the damping fluid, and W is the length scale of the surface exposed to the fluid. In bulk

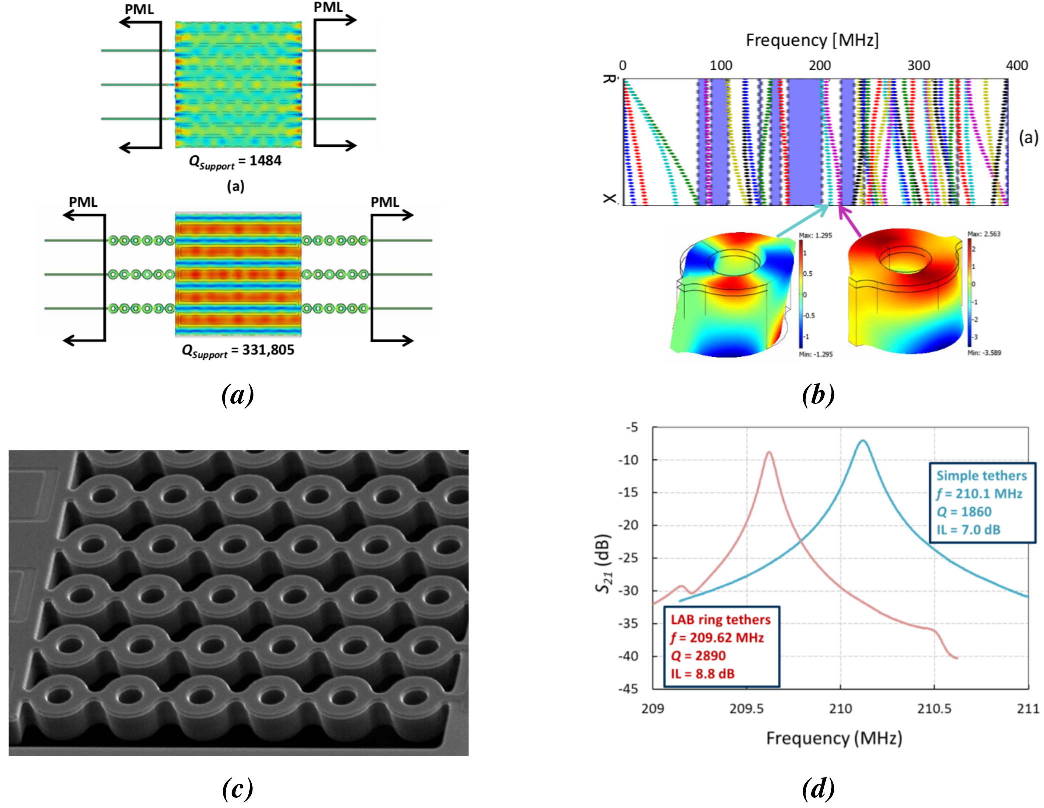

Figure 2.8. *(a) PML simulations of a lateral mode AlN-on-Si resonator. (b) Eigenfrequency simulations reveal band gaps forming along with two eigenmodes. (c) SEM of arrayed LAB tethers. (d)* S_{21} *measurements of two resonators with (left) and without (right) LAB tethers [35, 36].*

acoustic wave devices of relevance in this thesis with high equivalent stiffness, $\omega \gg \omega_c$ at even moderate pressures, allowing us to largely ignore SFD, though simulations are still performed.

Surface Loss Q_{SURF} encompasses losses arising from dissipation due to defects on the surface of the resonator, including but not limited to dangling bonds, adsorbed molecules, and microcracks and fractures [40, 41]. In particular, thin film materials epitaxially grown can suffer from interfacial defects arising from lattice mismatch with the substrate, introducing additional dissipation [42]. Grain boundary (in polycrystalline materials) and defects

can also be prominent sources of scattering and can induce significant dissipation. Therefore, using pure single crystalline bulk materials to fabricate resonators is highly desirable. In comparison to Si, SiC's chemical inertness and vastly larger Young's modulus make it an ideal material to mitigate any surface defects. Further, thin-film devices like shells [43] or cantilevers [41] are susceptible to surface effects with Q proportional to thickness. Coupled with the bulk nature of elliptical modes, thick silicon carbide resonators largely circumvent surface losses.

Phonon-electron loss—describing the acoustic phonon's interaction with the modified electron band due to deformation—is doping dependent resulting in ohmic losses due to undesirable flow of mobile charges [44, 45, 46]. In this work, this mechanism is ignore due to the doping concentrations and resistivities for CREE 4H-SiC wafers ($0.1\,\Omega - \text{cm}$). Other mechanisms in Table 2.1 are either unexplored or can be ignored in bulk silicon carbide resonators.

2.5 Silicon Carbide as a MEMS material

Already well established in high power electronics with wide bandgap (E_G), high breakdown field (E_b) and superb thermal conductivity k, silicon carbide is well-suited to transition as a MEMS material with amenable thermal, optical, mechanical and electrical properties. These are highlighted in Table 2.3 and compared with $(1\,0\,0)$ Si.

Mechanically, silicon carbide's low γ_{avg}, high stiffness (E_{avg}) and density offer not only low intrinsic mechanical dissipation (2.8), but also numerous advantages in sensor performance parameters with high frequencies and masses than silicon for similarly sized

Table 2.3: Bulk parameters comparing silicon and silicon carbide, values are reported for $T = 300$ K. $c_{l,t}$ are sound velocities for longitudinal and transverse waves, respectively.

Parameter		Silicon	4H-SiC	Notes
γ_{avg}		0.51	0.3	Higher Q_{AKE}, frequency, greater mechanical integrity, lower SFD, lower brownian noise
ρ [kg/m^3]		2320	3230	
E [GPa]		160	480	
c [m/s]	c_l	8433	12528	
	c_t	4447	7465	
c_v [J/(kg K)]		700	690	Lower Q_{TED}, but superior thermal management
k [W/(cm K)]		1.3	3.7	
α [ppm/K]		2.6	4.2	
E_G [eV]		1.12	3.26	Temperature and radiation hardness, chemical inertness
E_b [MV/m]		30	300	

devices (1.20b). Thermally, silicon carbide is beneficial for high temperature operation, with high thermal conductivities and relatively low thermal expansion capable of dissipating significant amounts of heat. However, this lowers Q_{TED}, making it poor for flexural mode resonators, though able to be sidestepped by using bulk acoustic wave modes to be explored in subsequent chapters.

CHAPTER 3

MONOCRYSTALLINE SILICON CARBIDE PROCESS TECHNOLOGY FOR FABRICATION OF THICK ELECTROSTATIC RESONATORS

Along with the advent of the Internet of Things, new frontiers in research and widespread interconnectedness comes demand for higher performance in more exacting environments. Silicon carbide thus becomes highly attractive for the reasons highlighted in section 2.5. Consequently, achieving fabrication and engineering prowess on par with silicon is highly desirable; however, a number of challenges stand in the way. Limited production—limited largely to 4" at the time of writing—render silicon carbide wafers regularly 20×–50× more costly than their silicon counterparts. With no loss of irony, properties that make it so desirable (hardness, chemical inertness) also conspire to complicate its growth, fabrication, and realization as a material for MEMS batch fabrication. Early efforts used chemical vapor deposition (CVD) to epitaxially grow thin films on silicon or 6H-SiC wafers to function as the device layer [47, 48]. These typically suffer from poor surface quality and other location defects that make them susceptible to surface effects, detrimental to Q [42]. Therefore, this chapter will explore the fabrication and micromachining of silicon carbide resonators in silicon carbide on insulator substrates with thick ultra-pure monocrystalline silicon carbide grown via the modified Lely process. Emphasis will be placed on the deep reactive ion etching of high aspect ratio trenches with smooth, vertical profiles.

3.1 Silicon Carbide: Growth and Crystallography

Unlike silicon which is grown in a melt via the Czochralski method, silicon carbide's high melting temperature and pressure (>3200 °C above 10 000 atm [49]) prohibit using traditional melt methods. Hence, SiC is grown using techniques based on vapor growth, high-temperature solution growth and their derivatives. As SiC sublimes relatively easily, physical vapor growth is favored and has become the principle method to form large SiC boules. The Acheson process was patented in 1892 and involved heating a mixture of salts in a graphite furnace to 2700 °C followed by a gradual reduction in temperature [50]; this method was inconsistent and yielded mostly polycrystalline 6H-SiC with large volume of defects, unsuitable for commercial production.

In 1955, the Lely method was developed with seed SiC lumps packed between two concentric graphite tubes. The inner tube is removed leaving an outer tube lined with porous SiC called the crucible. This is placed in an argon-rich environment and heated to 2500 °C at atmospheric pressure. At higher temperatures near the surface of the tube, the SiC powder at the wall sublimes; conversely, the SiC crystals start nucleating at the inner surface of the crucible and continue to grow as the process is prolonged. Similar to the Acheson process, this predominantly produced 6H-SiC crystals with a low yield of 3%, unsuitable for industrial or commercial application. However, the Lely method is ideal for producing ultra-pure seed crystals for other methods such as the modified Lely method.

In 1978, Tairov and Tsvetkov introduced the seeded sublimation growth technique, the modified Lely process [51], to date the only growth method implemented in industry. It was successful in suppressing spontaneous nucleation of species on the inner wall and

Table 3.1: Properties of common SiC polytypes with comparison to silicon [59].

Polytype	Si	3C (β)	4H	6H (α)
Crystal structure	Cubic	Cubic	Hexagonal	Hexagonal
Space group	$F d \bar{3} m$	$F \bar{4} 3 m$	$P 6 3 m c$	$P 6 3 m c$
Lattice constants [Å]	3.868	4.3596	3.0730	3.0810
			10.053	15.12
Density [kg/m^3]	2320	3230	3230	3230
Bandgap [eV]	1.12	2.36	3.26	3.05
Thermal conductivity [W/(cm K)]	1.3	3.6	3.7	4.9
Universal Anisotropy Index (section A.1)	0.287	0.536	0.130	0.133

controlling growth of the seed. Growth occurs at 1×10^{-4} atm with temperature from 1800 °C to 2600 °C with diffusion controlled transport facilitated by a temperature gradient between the source material and seed. Two configurations exist, differing by the locations of the source and boule; in the first, the seed was placed on a pedestal in the lower half of the crucible and was used with varying degrees of success [52, 53]. The second, much more commonly used today, places the source material at the bottom and foregoes a graphite crucible with yields above 90 % [54, 55].

Silicon carbide is a semiconductor that exhibits a large degree of polymorphism, existing in over 250 polytypes non-trivially contingent upon growth temperatures, seed orientation, and chamber conditions [56, 57, 58]; they're differentiated by the stacking orientation of the Si-C tetrahedrally-bonded bilayers. The most common ones are 3C, 4H and 6H, with the C and H designating their crystal symmetry: cubic and hexagonal, respectively. Table 3.1 shows select properties of these major polytypes.

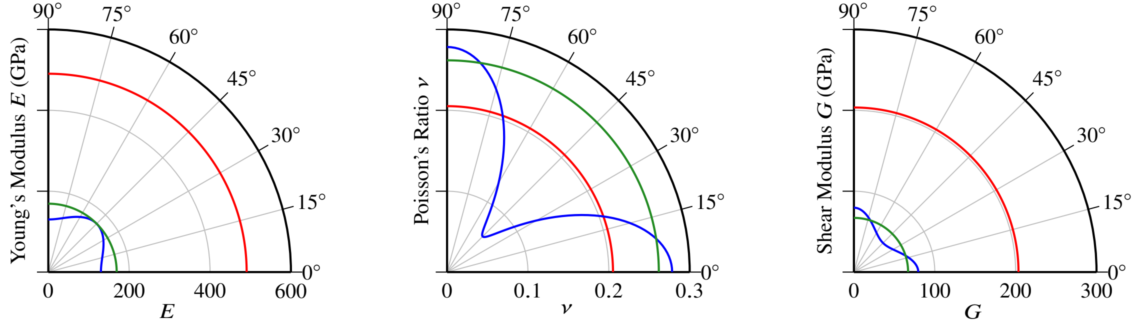

Figure 3.1. *Anisotropy (or lack thereof) of Young's modulus* E_1*, Poisson's ratio* ν_{12} *and shear modulus* G_{12} *in* $(0\,0\,0\,1)$ *4H-SiC (red),* $(1\,0\,0)$ *Si (blue) and* $(1\,1\,1)$ *Si (green). Here,* $0°$ *corresponds to wafer directions* $[1\,1\,\overline{2}\,0]$*,* $[1\,0\,0]$ *and* $[1\,1\,\overline{2}]$*, respectively. 4H-SiC's transverse isotropy renders its elastic behavior azimuthally invariant similar to* $(1\,1\,1)$ *Si. In contrast,* $(1\,0\,0)$ *Si exhibits variations up to* $45\,\%$*.*

3.2 Crystallinity and Degenerate Gyroscopic Modes

Critically, the substrate needs to support degenerate elliptical modes with the greatest amount of isotropy. In fact, materials with hexagonal symmetry are transversely isotropic (Figure 3.1)—rotationally invariant about the c-axis—and exhibit theoretical zero frequency splits for all elliptical modes, making them highly suitable for gyroscopic operation.

This is contrary to cubically symmetric materials such as $(1\,0\,0)$ Si which are only degenerate in odd-ordered elliptical modes (see section B.1). Figure 3.2 shows COMSOL simulation of a disk vibrating in its $m = 3$ elliptical mode for cubic and hexagonal materials; deformation is most distorted in cubic materials such as 3C-SiC and $(1\,0\,0)$ Si, virtually extinct in hexagonal 4H-SiC and theoretically non-existent in isotropic materials [60][1]. However, it's still important to grasp a substrate's anisotropy in all directions; one measure is the universal anisotropy index (see section A.1). To wit, 4H-SiC possesses the least

[1]Though ideal for anchor losses and cut misalignment immunity, bonding thick polycrystalline materials is prohibitively difficult and has not been demonstrated as of the time of writing. Further, polycrystalline materials suffer from their own pitfalls (dissipation, processing, growth quality, etc.).

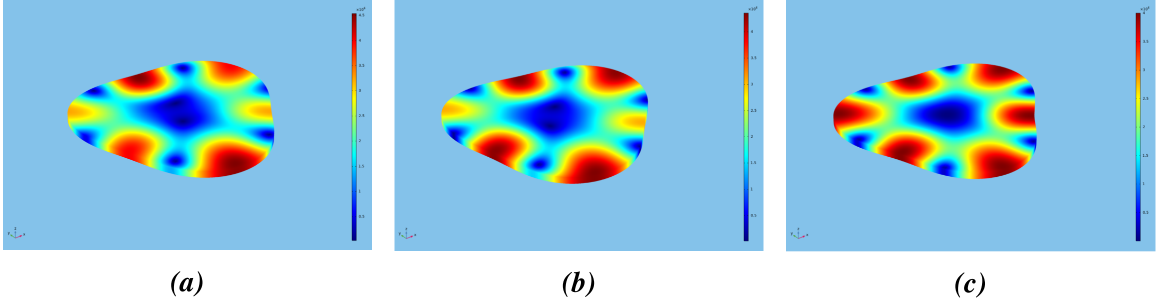

(a) (b) (c)

Figure 3.2. COMSOL simulated mode shapes for the secondary elliptical mode (m = 3) for (a) (1 0 0) Si, (b) (1 0 0) 3C-SiC and (c) (0 0 0 1) 4H-SiC. Referring to the heat map, significant material anisotropy in cubic materials such as (1 0 0) 3C-SiC and (1 0 0) Si manifests itself as non-uniform anti-nodal displacements. Transversely isotropic (0 0 0 1) 4H-SiC shows uniform displacement around the circumference of the disk.

anisotropy among common polytypes and far below that of silicon (Table 3.1).

4H-SiC's transverse isotropy can simplify electrode placement as the elliptical modes are radially isotropic. I.e. comparing Si's radial displacement in Figure 3.3 to 4H-SiC's in Figure 3.2c reveals that 4H-SiC can—in theory—utilize drive and sense electrodes at any arbitrary angular orientation (Figure 3.3). In practice, electrode implementations for (1 0 0) Si are far more complex [34, 61].

One common non-ideality is polar angle (the angle measured from the c-axis) mis-

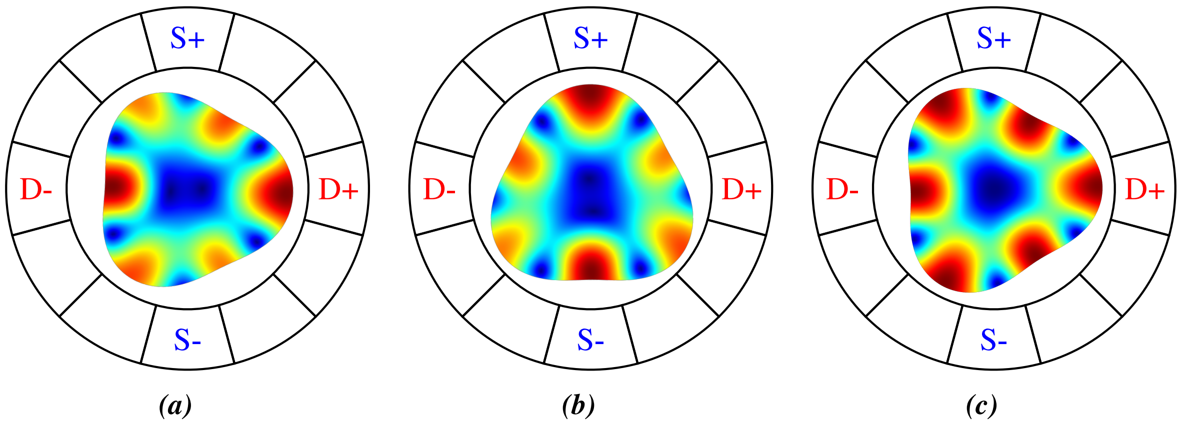

(a) (b) (c)

Figure 3.3. (a,b) (1 0 0) Si anisotropy results in non-uniform radial displacement and requires deliberate electrode placement for tuning, drive and pickoff. (c) On the other hand, (0 0 0 1) SiC could potentially simplify electrode placement configurations.

alignment following boule cut. While the effective stiffness changes comparably for both cubic and hexagonal materials, elliptical mode degeneracy remains high for 4H-SiC with induced frequency splits far lower than Si (Figure 3.4). Expressions for stiffness due to polar misalignment and elasticity frame transformations in general can be found in section A.2.

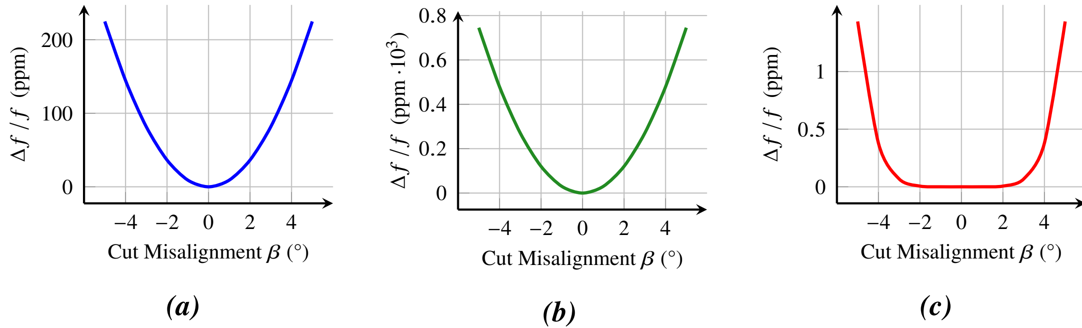

Figure 3.4. *COMSOL® simulation of the effect of polar cut misalignment on the frequency split of the degenerate $m = 3$ elliptical modes. (a) Significant non-degeneracy occurs in* (1 0 0) *Si with frequency splits in excess of* 100 ppm. *(b) This is significantly exacerbated in* (1 1 1) *Si with frequency splits approaching* 1000 ppm *whereas frequency split is lower by several orders of magnitude in SiC (c). The flatness between $-3°$ to $3°$ is likely due to meshing. Note that the three y axes are not commensurate with one another.*

This can be intuited by employing a 4° cut away from the (1 0 0), (1 1 1) and (0 0 0 1) planes for each substrate, respectively. In general, when the substrate is cut off-axis, the degenerate in plane Young's modulus E splits its degeneracy such that the two orthogonal components become $E_1 \neq E_2 \neq const$. In (1 1 1) Si, this discrepancy is substantial compared to (0 0 0 1) 4H-SiC resulting in significant disparity in manifest frequency splits (Figure 3.5).

3.3 SiC-on-Insulator (SiCOI) Platform

To enable batch fabrication of center-supported BAW disk gyroscopes, a silicon carbide on oxide on silicon (SiCOI) substrate is critical, analogous to silicon on insulator (SOI) substrates. Unlike SOI, no thick SiCOI is commercially available with device layers in excess

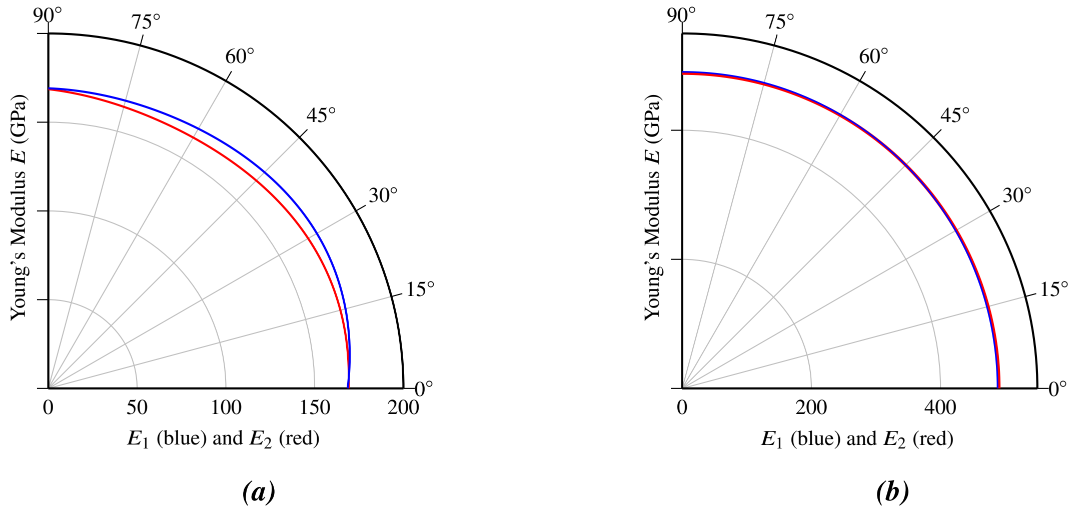

Figure 3.5. *(a) $E_{1,2}$ show large degree of splitting in $4°$ off-axis $(1\,1\,1)$ Si. (b) 4H-SiC remains virtually isotropic despite $4°$ wafer cut.*

of 10 µm, critical for structural integrity and performance. Consequently, it became necessary to develop custom-made SiCOI. Custom-made SiCOI wafers were bonded, grinded and polished following the same process as SOI fabrication. Ideally, a 4H-SiC handle layer can eliminate thermal expansion (α) mismatch during post-bond annealing. However, its extremely high Young's modulus can complicate wafer bonding [62]. Instead, silicon wafers are chosen as a handle layer. Wet thermal oxides were grown on both wafers as interlayers for bonding as well as buried layers for SiCOI substrates.

A 500 µm-thick 4H-SiC wafer from Cree has a Si-face $(0\,0\,0\,1)$ on one side whereas the other surface terminates with the C-face $(0\,0\,0\,\bar{1})$. As the C-face grows thermal oxide over eight times faster than the Si-face under the same wet oxidation conditions, it's chosen as the bonding face [64, 65]. Following RCA clean and thermal oxidation, the wafers are kiss polished to reduce surface roughness to below 1 nm RMS. After an O_2/N_2 surface plasma treatment, the Si wafers are then fusion bonded in an oven at 250 °C to the SiC wafer. Subsequently, bonded wafers are annealed again at 1100 °C to permanently

dehydrate and dehydroxylate the buried oxide (BOX) layer. Annealing the wafer pair improves the bond strength to ~2000 mJ/m^2 [66], close to the strength of conventional SOI wafers (~2600 mJ/m^2) Finally, the absence of residual air bubbles makes it possible to grind and polish the brittle SiC device layer to the desired thickness of 40 µm to 100 µm yielding the final SiCOI (Figure 3.6).

The process is non-trivial and initial yield of grinded SiCOI wafers was low (~ 30%). Measures such as pressurized bonding, edge-trimming [67] were introduced to reduce voiding and to mitigate any cracking due to chipping at the edges (Figure 3.7).

3.4 Fabrication of SiC Resonators

Fabrication of SiC resonators presents an inherently monumental challenge owing to SiC's chemical inertness, necessitating elevated powers, highly optimized gas flows and proper thermal management. The basic process flow is shown in Figure 3.8 with detailed process parameters in Appendix D.

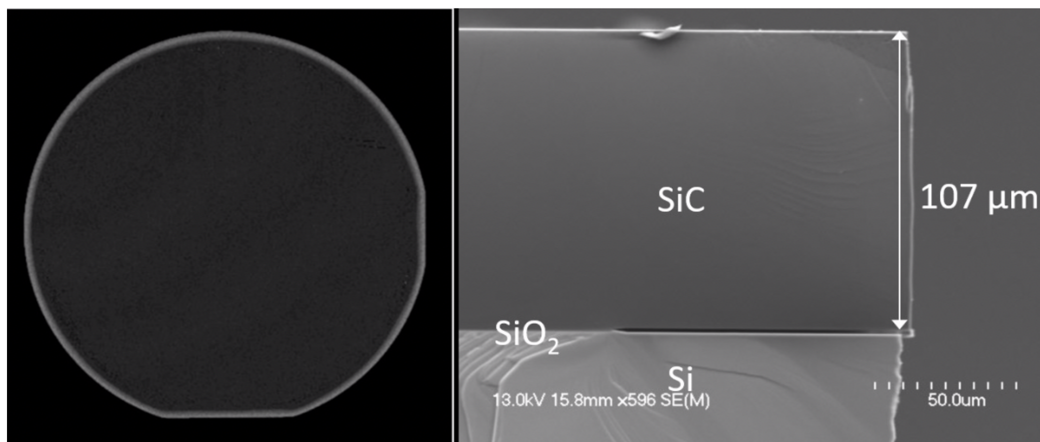

Figure 3.6. *(left) Surface acoustic microscope (SAM) image of a completely bonded SiCOI wafer without voids. (right) SEM of the HF-released (etch rate of* 6 µm/min*) SiCOI wafer [63].*

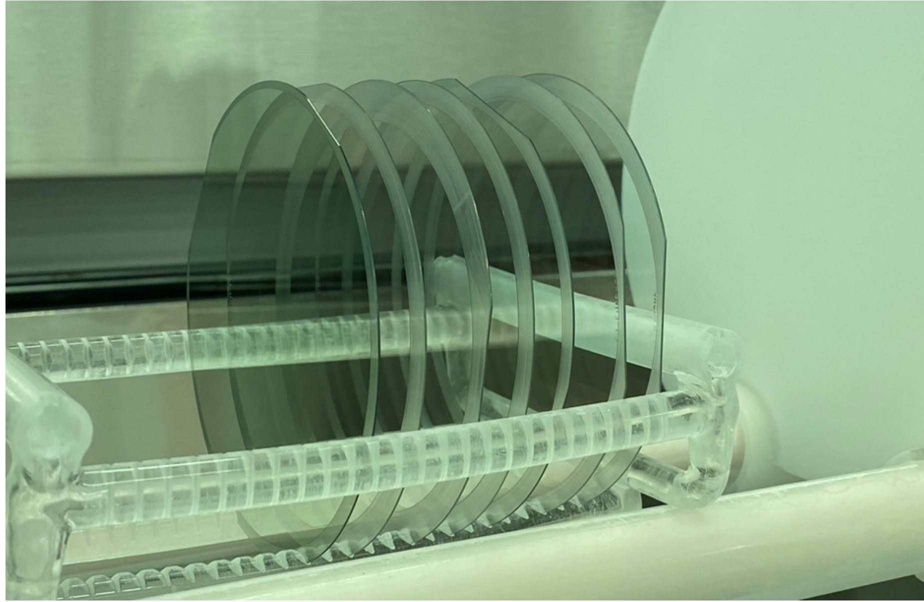

(a)

(b)

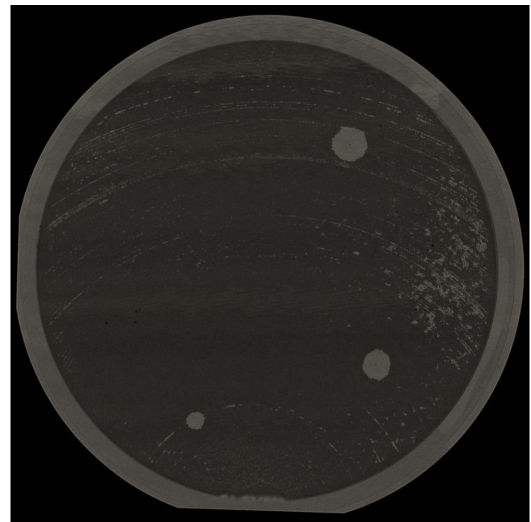

(c)

Figure 3.7. *(a) Edge-trimmed wafers prior to thermal wet oxidation. The darker wafer in front is a* 4° *off-axis wafer. (b) Pressure bonded wafers reduce voiding. (c) A successfully grinded wafer; edge trimming allows for grinding despite voids.*

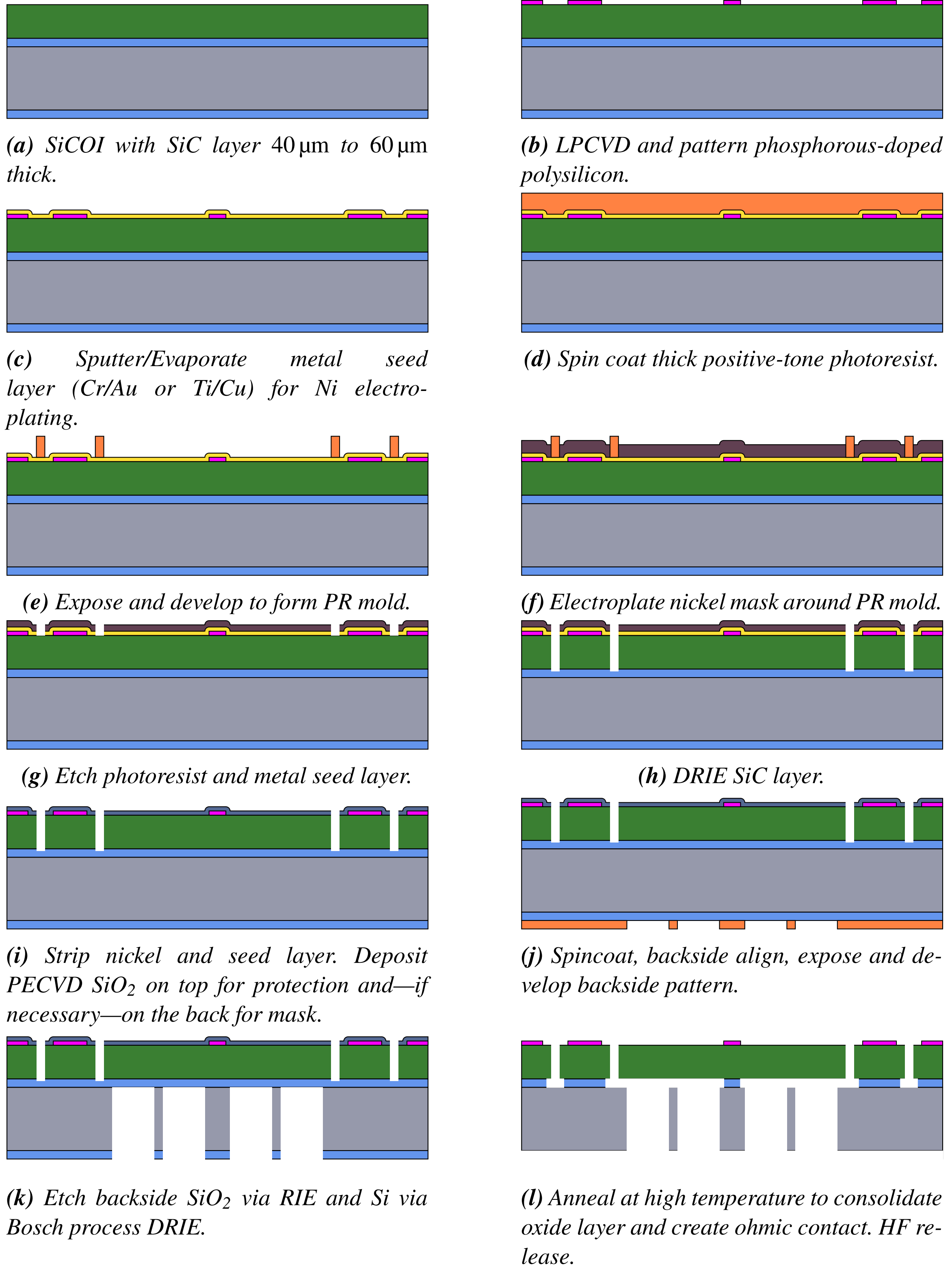

(a) *SiCOI with SiC layer* 40 µm *to* 60 µm *thick.*

(b) *LPCVD and pattern phosphorous-doped polysilicon.*

(c) *Sputter/Evaporate metal seed layer (Cr/Au or Ti/Cu) for Ni electroplating.*

(d) *Spin coat thick positive-tone photoresist.*

(e) *Expose and develop to form PR mold.*

(f) *Electroplate nickel mask around PR mold.*

(g) *Etch photoresist and metal seed layer.*

(h) *DRIE SiC layer.*

(i) *Strip nickel and seed layer. Deposit PECVD* SiO_2 *on top for protection and—if necessary—on the back for mask.*

(j) *Spincoat, backside align, expose and develop backside pattern.*

(k) *Etch backside* SiO_2 *via RIE and Si via Bosch process DRIE.*

(l) *Anneal at high temperature to consolidate oxide layer and create ohmic contact. HF release.*

Figure 3.8. *Basic process flow for a capacitive silicon carbide disk resonator with backside release pattern/PnC. Fabrication of other resonators can be derived from this one.*

Table 3.2: Inexhaustive review of masking materials used for deep reactive ion etching of silicon carbide.

Mask	Selectivity	Reference
Ni	20–90:1	[69, 70, 71, 72]
Cr	30:1	[73]
PECVD SiO_2	< 3:1	[69, 74]
Photoresist	1:4	[75]
ALD Al_2O_3	6–10:1	[69]
Sputtered AlN	16:1	[74]

3.4.1 Silicon Carbide Deep Reactive Ion Etch

SiC DRIE requires a hard mask capable of withstanding the harsh etch process without significant micromasking–where mask material is sputtered into trenches creating defects–while conferring good selectivity. Silicon oxide or photoresist, typically used as masking materials in the DRIE of silicon, shows little to no selectivity over SiC. For good selectivity, materials with low etch byproduct volatility are of principal interest and under active investigation. However, nickel remains the material of choice for its ease of thick deposition, good selectivity, and minimal micromasking relative to other materials. E.g. while some work shows copper or aluminum to offer better selectivity, they exhibit significantly greater micromasking [68]. Further, selectivity is highly dependent on etch conditions and chemistries which are contingent upon the desired etch profiles. As of the time of this writing, nickel is the only masking material capable of sufficient thickness, selectivity and etch quality for use in thick high aspect ratio silicon carbide trenches (Table 3.2).

We utilize the LIGA process to define and grow the metal mask (Figure 3.8(c-f)). A

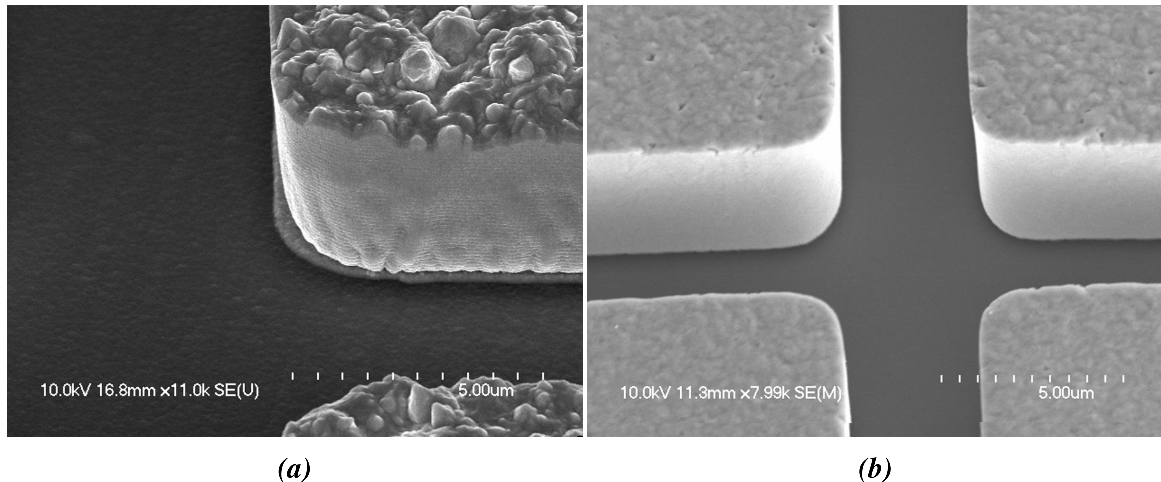

(a) *(b)*

Figure 3.9. *(a) Electroplated nickel on Cr/Au seed layer dry etched with transference of the PR's wavelength-limited scalloping. The lateral waviness at the bottom is due to the substrate's rough features, an artifact from the grinding process. (b) Wet-etched Ti/Cu seed layer shows a small gap between the nickel and substrate. The gap's effect on subsequent DRIE is disputed.*

seed layer composed of an adhesion layer of Ti or Cr (20 nm) and a conductive layer of Cu or Au (100 nm) is sputtered/evaporated. The choice is largely irrelevant for traditional processing though one should investigate chemical compatibilities for subsequent processing steps (e.g. noble metals like gold are typically far more inert). Next, thick (>10 µm) AZ-9260 photoresist is patterned to create a mold around which nickel is electroplated. A low-power high pressure O_2 plasma descum is performed in order to form polar hydroxyl groups on the surface to increase surface energy and hydrophilicity[2]. Nickel is electroplated under controlled temperatures and current densities (Table 3.3) to mitigate stress and improve uniformity and grain size [76]. When the nickel film has reached the desired thickness–determined through profilometry–the photoresist mold and seed layer are removed via acetone and either wet or dry chemistries (leaving the nickel unharmed) in preparation for SiC DRIE (Figure 3.9).

[2]Performed in a parallel plate RIE tool at 80 W RF power, 100 sccm O_2 and 80 mTorr.

Troubleshooting Nickel Electroplating

Nickel electroplating—in theory—is a fairly simple process with only a few equations truly governing it. The first is Faraday's law of electrolysis which gives the amount of material electroplated in terms of current:

$$m = \frac{QM}{Fz} \xrightarrow[\text{current}]{\text{constant}} \frac{ItM}{Fz} \tag{3.1}$$

where m is the mass dissociated at an electrode in g, $Q = It$ is the charge passed through the current in C, F is the faraday constant in C/mol, M is the molar mass and z is the valence number of the electroplated substance. For Ni, $z = 2$ [77]:

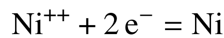

$$\begin{aligned} \mathrm{Ni} &= \mathrm{Ni^{++}} + 2\,\mathrm{e^-} \\ \mathrm{Ni^{++}} + 2\,\mathrm{e^-} &= \mathrm{Ni} \end{aligned} \tag{3.2}$$

In practice however, a huge number of issues complicate its implementation [78], a number of which will be discussed.

Defects due to Contamination The nickel electroplating solution used is Elevate® Ni 5910 nickel sulfamate RTU ("ready to use") which must be maintained properly in order to produce nickel masks with any semblance of reproducibility. Contamination intrinsic to the solution additives' interaction with the nickel anode can lead to significant mask defects which can lead to pin holes in the mask. *During* electroplating, solution additives serve to improve anode corrosion and dissolution. However, when not electroplating, these additives still react with the anode and produce contaminants; consequently, the anode should be

*Table 3.3: Typical solution composition and parameters used for Ni electroplating: Technic, Inc.'s Elevate Ni RTU nickel sulfamate solution. Parameters a typical user should monitor are in **bold**.*

Parameter	Value	Remark
Temperature [°C]	50-60	Minimizes stress and resistivity.
Current Density [mA/cm^2]	3-5	Allows for deposition rates 2 μm/h to 3 μm/h while maintaining film quality. Excessive current density can lead to burning due to water hydrolysis at the cathode.
pH	3.8	pH affects film greatly: ductility, presence of defects among others. Sulfamic acid crystals (70 mg/L) will lower pH by 0.1. Nickel carbonate will raise it.
Agitation via magnetic stirrer [rpm]	700	Critically important to replenish available Ni^+ at the substrate
Nickel, metal [g/L]	80	Available Ni^+ ions, this parameter is more relevant for large industrial-scale plating
Boric acid [g/L] (optional)	45	Acts as a pH buffer: boric acid consumes 2 OH^- hydrolysis products
Chloride/Bromide additives [g/L] (optional)	2.5	Used to improve anode corrosion during plating but can induce tensile stress. Not necessary if using sulphurized nickel anodes.
Brightener [mL/L] (optional)	10	Can be used to make finer grains at the cost of ductility, stress in the film and contamination.

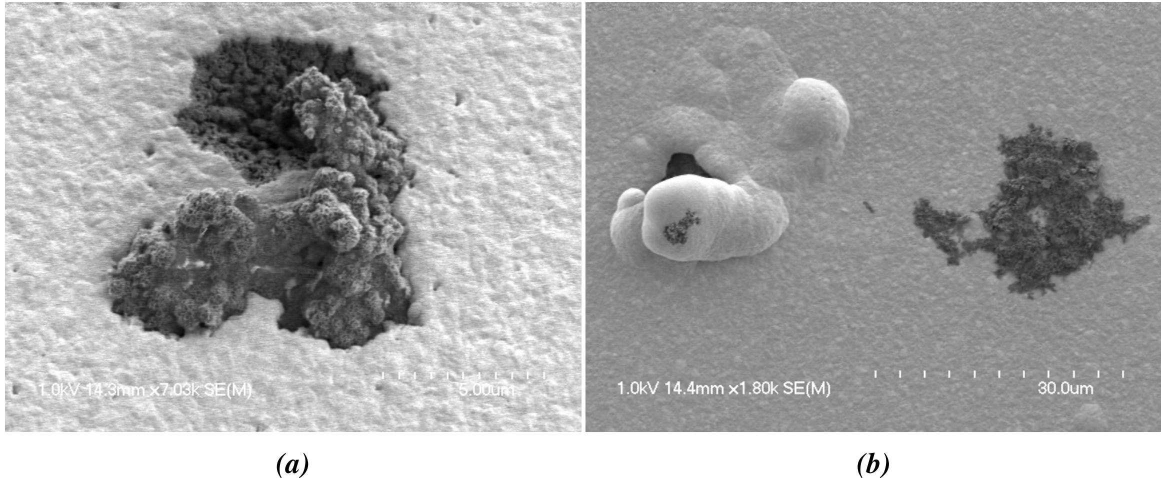

(a) *(b)*

Figure 3.10. *Various nickel defects arising due to contamination be it intrinsically (solution additives reacting with the nickel anode) or extrinsically introduced.*

removed from solution when not plating. Essentially, the nickel anode should be in the plating solution only *when* plating, and should be in DI water/air-dried when not. If one observes defects as in Figure 3.10, one may either replace the solution, or filter the solution via activated carbon or even pouring the solution through a texwipe (surprisingly effective). Further, electrolytic purification via a dummy plating run at low current densities should be performed.

Thickness Non-uniformity One may also observe non-uniformities in film thickness. Intrinsically, substrate edges will have increased growth rates due to higher electric fields and in theory, little can be done. In practice, this manifests itself as ~ 1 μm difference between the center and edge of a 4 inch wafer. Extrinsically, the cathode (substrate) and anode should be as parallel as possible to promote electric field uniformity. Additionally, the anode to cathode surface area ratio should be kept above unity with sufficient agitation. Micro-scale uniformity can be addressed by utilizing pulsed DC plating or even reverse plating to improve granular size at the cost of plating speed, it may also help with defects

by allowing more time for ions to be replenished in the surface's immediate vicinity.

3.4.2 Etch Chemistry and Parameters

DRIE of silicon carbide is multidimensional and non-linear phenomenological area of study spanning a huge parameter space. Various etch chemistries to etch silicon carbide exist: such as chlorine [79, 73] and bromine based chemistries [80]. However, fluorine-based chemistries—namely SF_6—are the most suitable for thick etching given the high volatility of its etch byproducts [81, 75]. Co-etchants such as Ar and O_2 are introduced to increase kinetic bombardment of the substrate and modify plasma chemistries, respectively. The effect of O_2 addition is disputed; it allows additional chemical pathways for volatilizing C in the forms of CO, CO_2 though there is consensus that there is a non-monotonic effect upon etch rate with increasing O_2 concentration [75, 82].

SiC was etched using a mixture of sulfur hexafluoride (SF_6), argon (Ar) and oxygen (O_2) gases under high DC bias voltage. Upon physical bombardment and dissociation, the C-atoms in the SiC react with the etching gas (SF_6) to form an inherent metallofluorocarbon passivation layer (NiC_xF_y) that deposits on the sidewall. This compound deposition enables anisotropic high-aspect-ratio (HAR) scallop-less trenches (~ 20:1) without alternating between etching and passivation used in the conventional Bosch process. Incidentally, a multiplexed etching process has been investigated with limited success [83]). However, with increasing aspect ratio, it's speculated that the composition of etch reactants and species changes drastically and passivation no longer forms leading to bowing. Notably, trench width greatly affects etch rate (Figure 3.11). When SEM inspection reveals that the trenches have reached the box layer, the remaining Ni mask and passivation layer on the sidewall

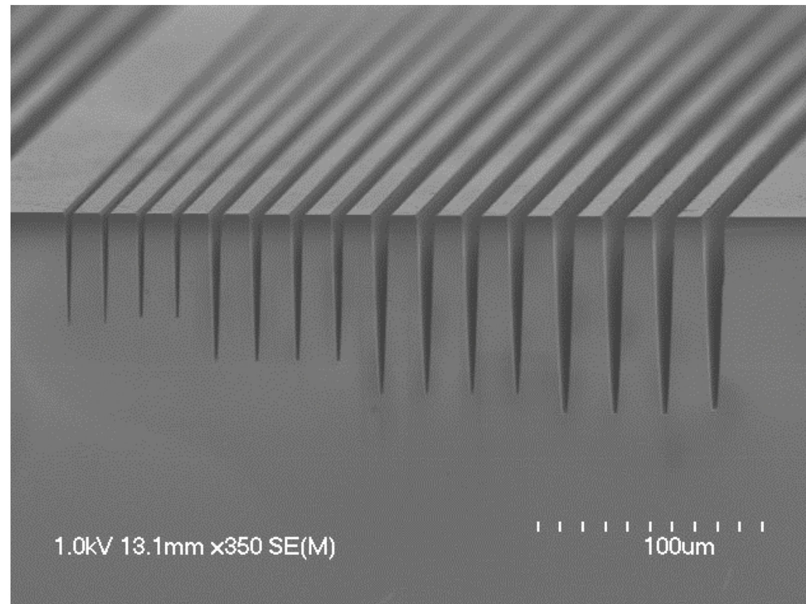

Figure 3.11. *As trench width decreases, etch rate decreases (right to left).*

on the trench are removed by wet chemistry: dilute nitric acid (HNO_3), acidic piranha solution (H_2SO_4/H_2O_2) and EKC265™ post-etch residue remover.

3.4.3 Effect of Process Parameters on DRIE

Two recipe paradigms were developed depending on the tool available. The older STS® AOE lacked proper thermal management, high power and a robust electromagnetic coil to inductively couple the plasma. Instead, it relied upon permanent magnets to augment the plasma density with limited efficacy and a clamping/cooling system with a frail o-ring that was attacked by the plasma. Perhaps most damning, etching silicon carbide leaves significant deposits on the chamber wall, requiring manual cleaning with ScotchBrite® to avoid damaging the aluminum chamber walls. The new STS AOE Pro tool addresses many of these issues: its coil and platen powers are able to go far higher, the chamber operates at higher temperature and the platen has improved cooling capabilities utilizing

Table 3.4: Partial list of parameters available in an ICP-DRIE system. Recipe values for AOE and AOE Pro highlight the respective tools' capabilities.

Parameter	AOE	Pro	Remark
Coil Power [W]	800	1800	Higher plasma density allows for increased SF_6 chemical etch but reduced DC bias.
Platen Power [W]	200	300	Increases anisotropy and bombardment kinetic energies.
Induced DC Bias [V]	280	120	A measure of the electric force felt by the heavy ions that are unable to respond to high frequency excitation. Arises due to high DC impedance at platen. The AOE Pro's small DC bias is a result of improved inductive coupling with the plasma.
Process pressure [mTorr]	8	8	Lower pressures increase mean free path of species, increasing anistropicity.
Platen Temperature [°C]	-10	20	Affects etch rate though effect is minimal in the range −10 °C to 40 °C assuming proper substrate mounting and fixture.
SF_6 flow [sccm]	40	250	New tool's higher plasma density motivated choice to increase SF_6 flow to improve etch rates.
Ar flow [sccm]	120	50	Ar flow for physical bombardment, reduced in new recipe to minimize passivation peeling.
O_2 flow [sccm]	0	25	In accordance with literature, set to 10% of SF_6 flow with minor effect on profile and etch rate.
4 µm-wide trench etch rate [nm/min]	450	900	New tool enables etch rates approaching 1 µm/min in narrow gaps.
Chamber wall temperature [°C]	100	120	Higher chamber wall temperature renders cleaning both less frequent and less manually intensive.

a seal-less design. All in all, the tool's improvements allowed for higher plasma densities, better cooling faculties and enabled a far more consistent etch run to run. Table 3.4 includes the silicon carbide etch recipes and delineates many of the differences between the two tools. The recipe developed on the old AOE employed a more physical etch, characterized by high Ar flow rates and induced DC bias voltage. Conversely, the new AOE pro saw a shift toward a more balanced approach, with increased SF_6 flow and higher coil powers to increase plasma density with improved results (Figure 3.12).

Effect of SF_6 Flow Rate While all parameters induced small variations in the resultant etch, within the AOE Pro recipe paradigm of Table 3.4, the most salient parameter with regards to etch rate is the SF_6 flow rate, with a strong positive correlation (Figure 3.13). It should be noted that the etch-rate is not simply a function of gap width and SF_6 flow, beyond a certain depth which seems to be positively correlated with flow rate, etching is limited and sidewall quality is degraded. In other words, one may not indefinitely etch without compromising the sidewall.

Interaction with the BOX Layer As in SOI etching, footing at the base of the trench can occur (Figure 3.14). As the buried oxide layer is insulating, incoming ions induce charge within it and cause subsequent ions to Coulomb scatter into the bottom of the trench. RF power is usually applied at 13.56 MHz (merely to conform to ISM application standards); however, in SOI etching using the Bosch Process, the platen is usually driven at 380 kHz to mitigate footing by reducing the frequency at which ions can strike the BOX. As neither the AOE nor AOE pro possess a low-frequency power supply, we had to make do with the

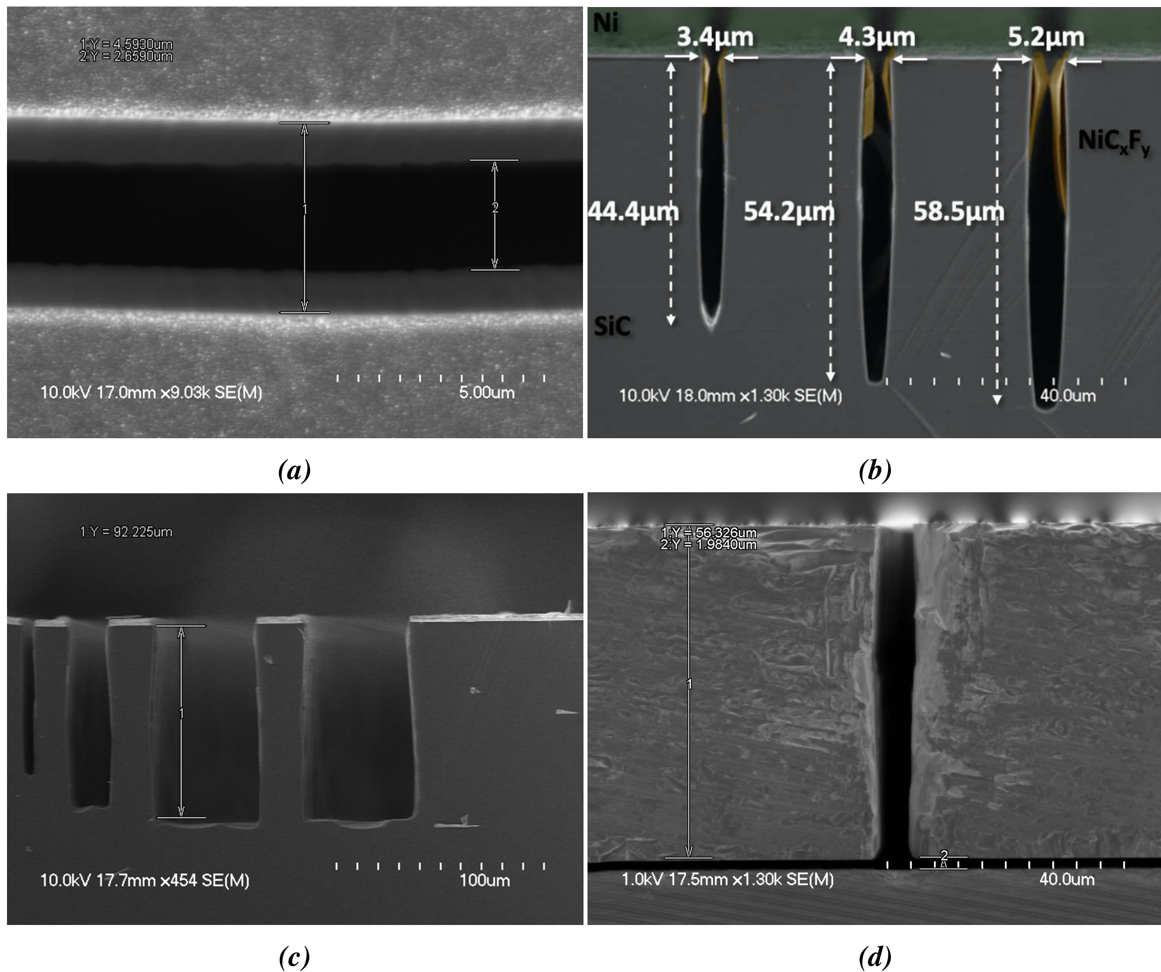

(a) *(b)*

(c) *(d)*

Figure 3.12. *AOE Pro recipe (Table 3.4)* 60 min*: (a) Passivation grows at* ~ 15 nm/min *(b) The recipe shows a fairly strong aspect ratio dependence for narrow trenches and only exhibits etch defects in* 3.4 μm*-wide trenches past* 40 μm*. Remaining nickel is shown in green with selectivities ranging from 15:1 to 30:1 for narrow trenches. (c) Wide trenches and features etch at a rate of* 1.5 μm/h *with minimal micromasking and an etch selectivity of ~ 45:1. (d) The same recipe employed on SiCOI with little to no difference in performance, showing that the recipe is robust to substrate changes.*

13.56 MHz power supply. Further, given that the BOX layer offers very little selectivity to SiC, it doesn't act as an etch stop as in traditional SOI etching (Figure 3.14); therefore, fabrication of SiCOI wafers should aim to have the lowest total thickness variation (TTV) across the wafer possible. This starts with purchasing low TTV silicon wafers, monitoring oxide thickness during oxidation and picking the correct grinding solution to offer the best

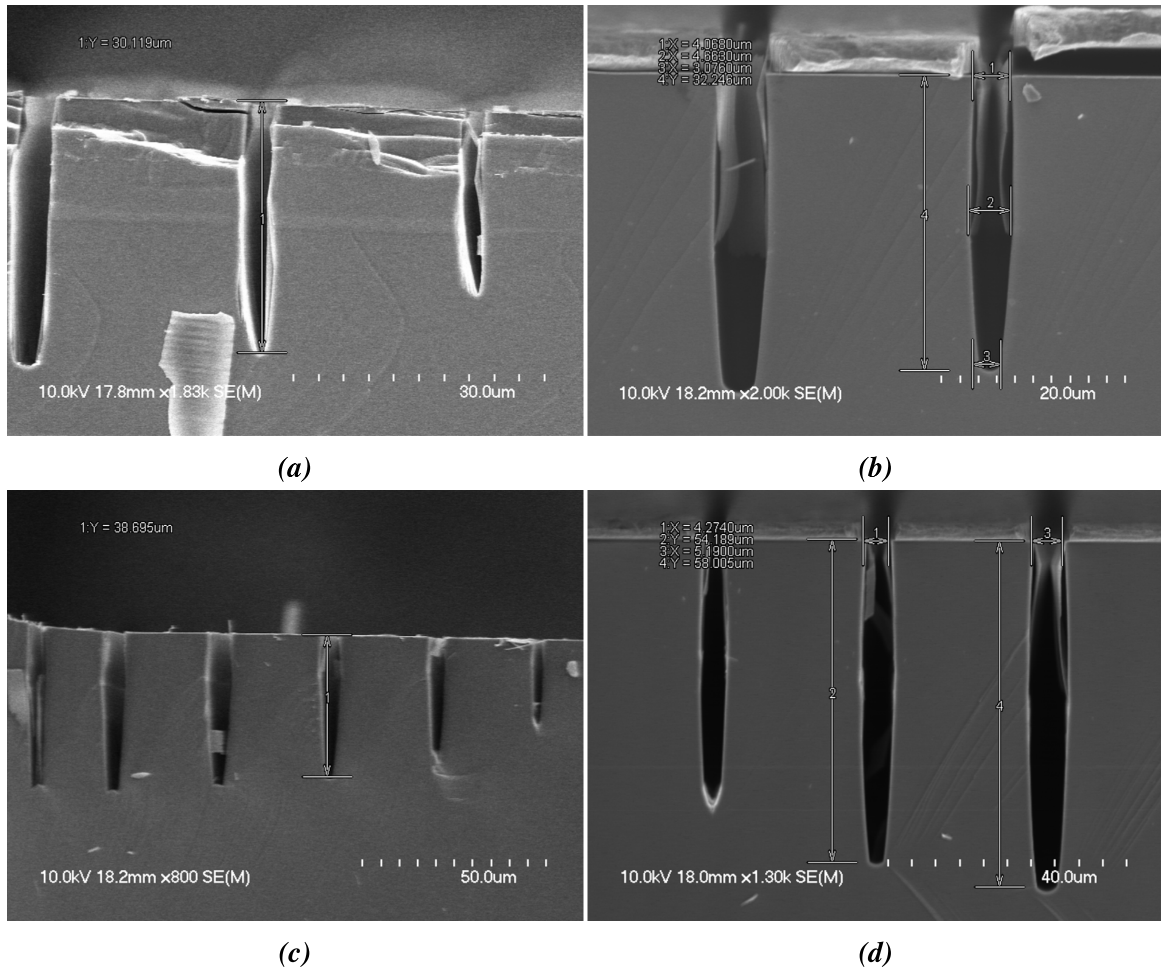

Figure 3.13. *Etch rates of a* 4 µm*-wide gap for different* SF_6 *flow rates (a)* 40 sccm*,* 90 min*:* 20 µm/h *(b)* 150 sccm*,* 45 min*:* 45 µm/h*, (c)* 200 sccm*,* 45 min*:* 50 µm/h *and (d)* 250 sccm*,* 60 min*:* 54 µm/h*. Runs at the tool's MFC-limited* 300 sccm *were attempted but were scrapped due to the tool's automatic pressure controller reaching its limit.*

SiCOI possible. Early SiCOI wafers possessed TTV of up to 10 µm; further development led to wafers with TTV below 1 µm.

3.4.4 Polysilicon Plug

The polysilicon plug enables polarization of a centrally-supported disk resonator without manual wire-bonding to the center of the disk; the flow is depicted in Figure 3.15. Prior to defining and etching the resonator, one etches trenches that form the outline of the center

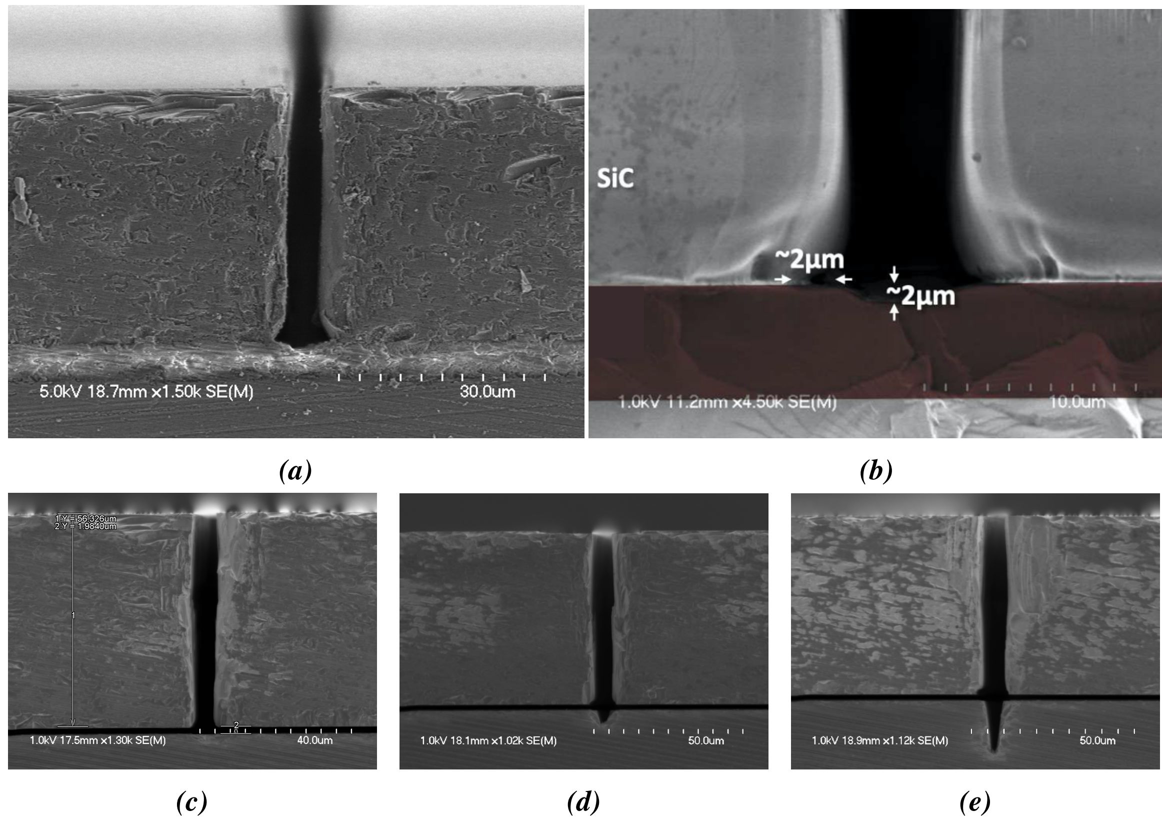

(a) ***(b)***

(c) ***(d)*** ***(e)***

Figure 3.14. *Etch interactions with the BOX layer: (a) footing occurs due to BOX charging. This effect is visible in SEM (bright interlayer) as incident electrons charge the BOX layer, adding electrons to the sample and distorting the image. (b) Close-up of the bottom of the trench with footing* ~ 2 µm *on each side due to over-etch. BOX is colored brown in post-processing. (c-e) Different locations in the same sample as Figure 3.12d showing overetches of* 0 µm*,* 5 µm *and* 15 µm*, respectively. TTV becomes incredibly important barring other developments in DRIE of silicon carbide.*

pedestal. LPCVD polysilicon of the appropriate dopant-type is deposited in an attempt to fill the trenches and form the plug; however, as corners possess the lowest nucleation barrier, trenches tend to pinch off, occluding further deposition and leaving a void. Etch backs are necessary to fill the plug well and without voids which can impact device performance. Following the final deposition, the process can continue from Figure 3.8(b). As the disk is subsequently aligned to the poly plug rather than the backside release structure to the disk, the pedestal is inherently better centered (< 1 µm vs ~ 2 µm to 5 µm with backside

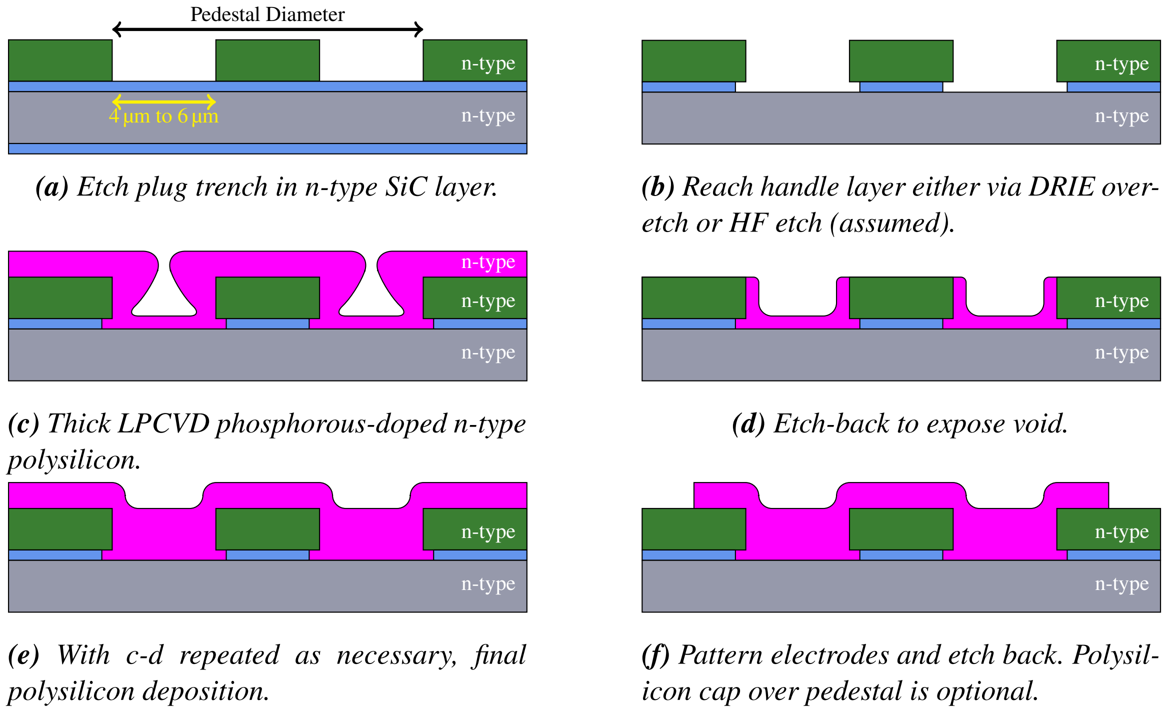

(a) *Etch plug trench in n-type SiC layer.*

(b) *Reach handle layer either via DRIE over-etch or HF etch (assumed).*

(c) *Thick LPCVD phosphorous-doped n-type polysilicon.*

(d) *Etch-back to expose void.*

(e) *With c-d repeated as necessary, final polysilicon deposition.*

(f) *Pattern electrodes and etch back. Polysilicon cap over pedestal is optional.*

Figure 3.15. *Process flow for polysilicon plug. Provides resonator polarization with additional benefit of augmented pedestal strength and HF resilience.*

alignment).

3.4.5 Sidewall Passivation

During the etch, passivation builds on the sidewall and can laterally shrink the trench width, reducing the aspect-ratio dependent etch rate and ultimately occluding the trench. Whereas resonators fabricated for optical laser doppler vibrometer (LDV) measurements have no trench width requirements, capacitive sensing demands narrow trenches as the resonator's motional resistance and insertion loss scale quartically with gap size [34]. This passivation is composed of nickel fluorocarbon polymers with no means of removing it via dry etch (Figure 3.16). However, Piranha and EKC265 are fairly aggressive but offer no selectivity to nickel.

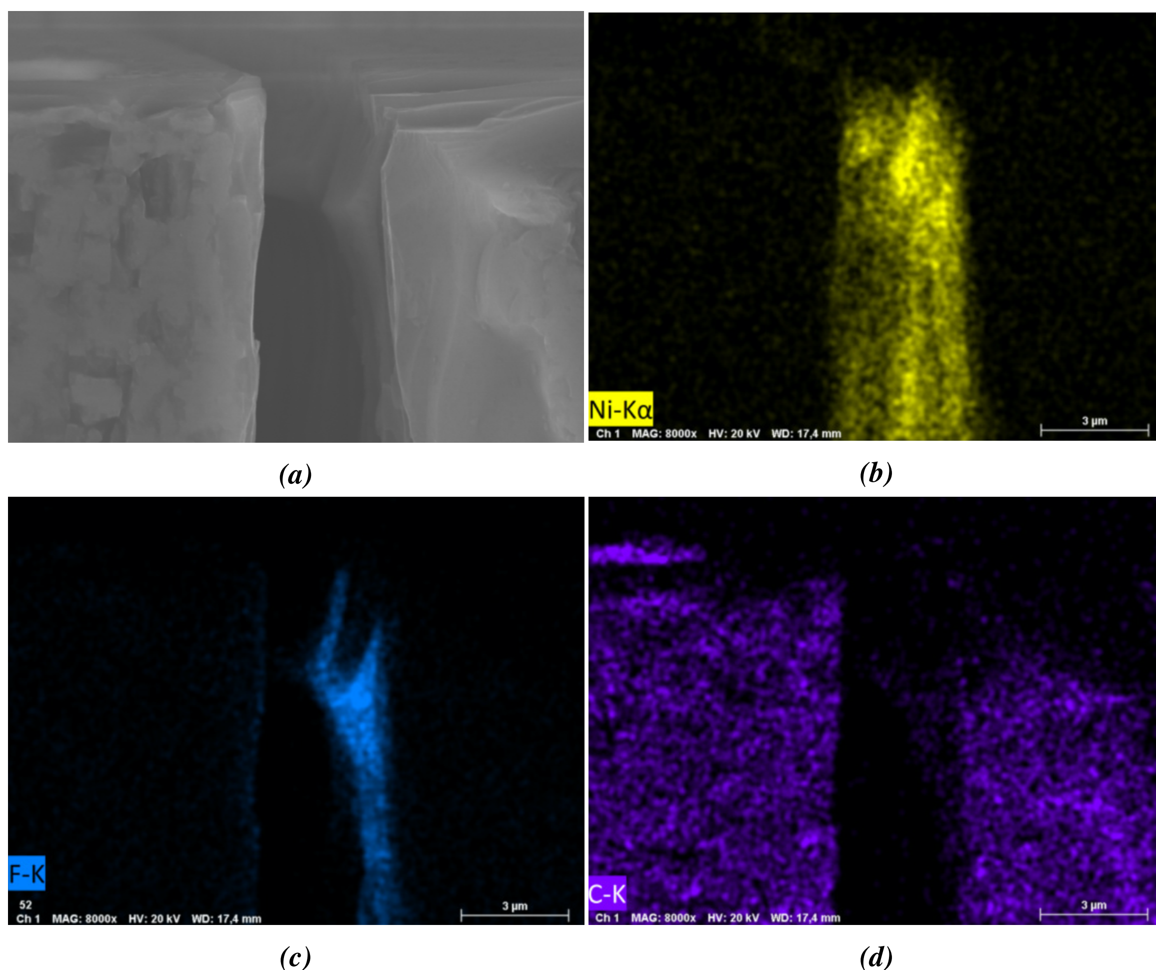

Figure 3.16. *Electron dispersive x-ray spectroscopy of sidewall passivation. Incident electrons are scattered and detected with each atom exhibiting a unique spectrum. (a) SEM of an etched high aspect ratio trench before cleaning. (b-d) Atomic count mapping for Ni, F, and C.*

Ex-situ Removal Consequently, in-situ removal of the passivation layer–without damaging the nickel layer–became a principal focus. We investigated several methods of fluorocarbon removal including: oxygen plasma [84], supercritical CO_2 [85], as well as hydroxylamine and TMAH based commercial solvents such as EKC 265, 652, and 162. Ultimately, EKC162™ showed efficacy, good repeatability, and excellent metal selectivity (Figure 3.17), enabling further etching. However, this method was utilized as a stop-gap measure and re-etching proved to be troublesome leaving damaged surfaces and sidewalls. Focus shifted

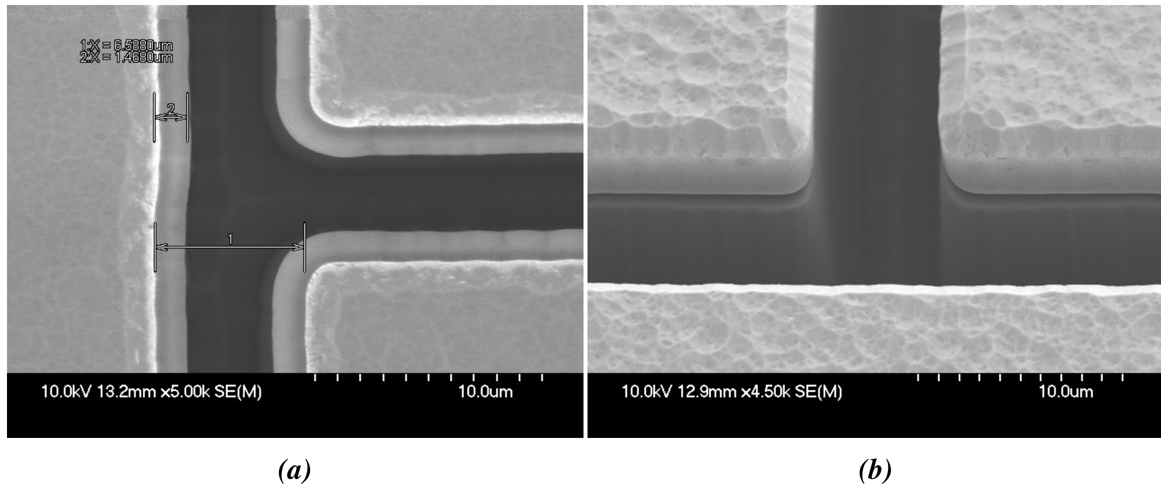

(a) ***(b)***

Figure 3.17. *(a) Passivation builds at* ~1 μm/h*, limiting the depth of the etch due to trench pinching and subsequent closing. (b) Following in-situ clean using EKC 162™ residue remover, the trench is cleaned with the nickel mask preserved.*

toward optimizing a recipe to etch deeper and narrower either by minimizing or belaying tapering (Table 3.4).

Passivation Peeling Any thin film deposition at $\Delta T = T_{dep} - T_{room}$ will suffer from internal stress due to thermal expansion mismatch; nickel fluorocarbon passivation on the sidewall is no exception. This passivation—once thick enough—begins to peel, causing plasma species to deviate from anisotropy and inducing sidewall damage. Notably—all other parameters held constant—reducing Ar flow virtually eliminated passivation peeling (Figure 3.18d).

3.4.6 Backside Etch and Release

The release holes/backside geometry in the silicon handle layer is then defined via backside alignment to the SiC device layer and through-etched by standard Bosch process in STS Pegasus with high coil power and a ramped platen power. As the SiCOIs were created using 380 μm to 500 μm thick Si handle layers, significant teflon can build up

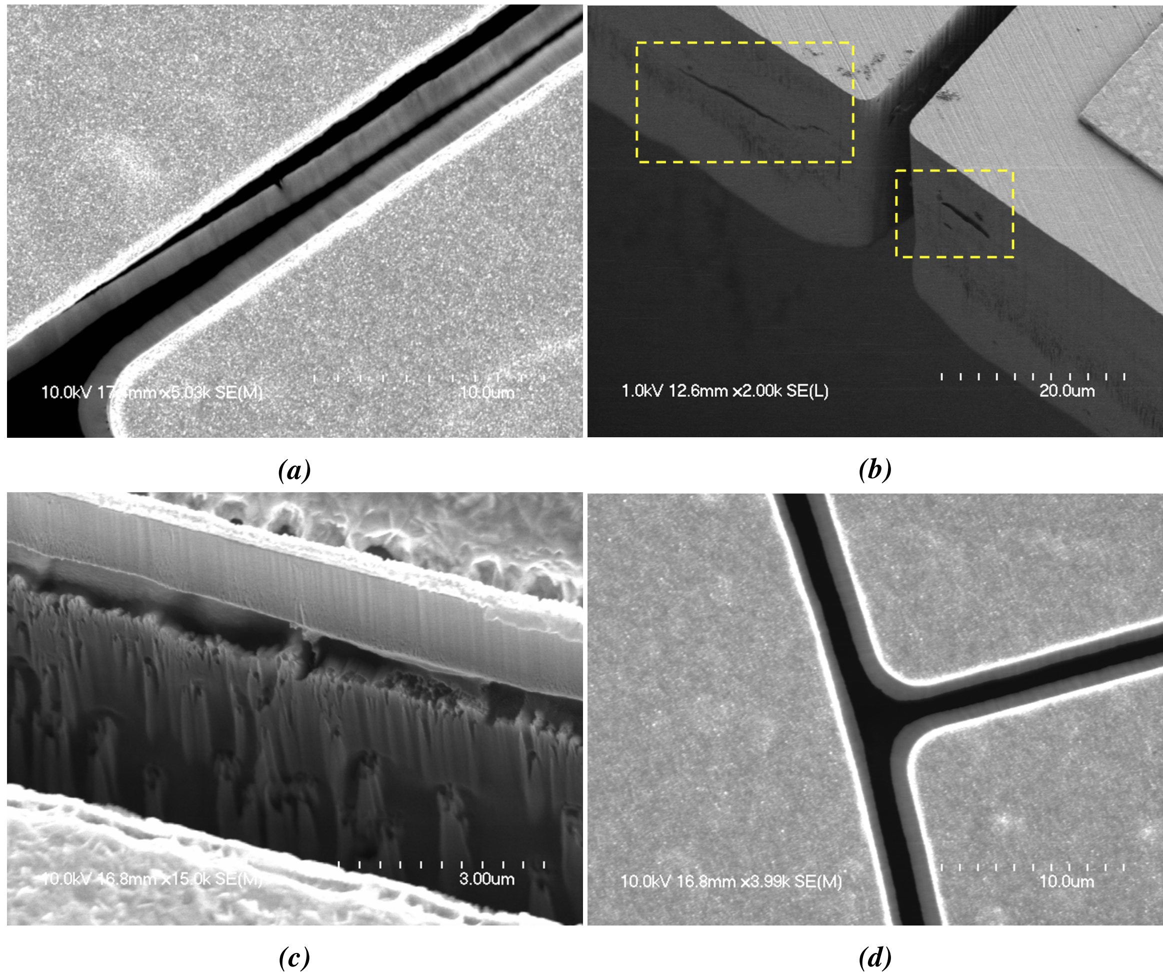

Figure 3.18. *(a) Passivation peeling after a certain deposition thickness. (b) Passivation charges and deflects incoming plasma species causing sidewall damage and daggering. (c) A particularly severe case. In this case, improper* ex-situ *cleaning exacerbated the passivation peeling problem. (d) Everything else constant, reducing the Ar flow removes peeling while maintaining etch depth and rate.*

requiring thorough cleaning lest it creates debris which can affect resonator losses as well as disrupt electrical transduction. The individual devices are then placed in HF which undercuts the buried oxide layer, releasing the device and enabling mechanical vibration.

3.4.7 Ohmic Contact Formation

Naturally, in order to function as a capacitive transducer, ohmic contact needs to be established between the interfacing circuitry and the device itself. Unlike in silicon, a

simple wirebond to the electrode doesn't suffice as a metal-semiconductor Schottky barrier is formed at the SiC interface precluding electrical transduction. Traditionally, ohmic contact has been established by annealing a refractory metal, thereby forming a silicide with a reduced barrier height [86, 87]. However, metals are generally incompatible with subsequent processing and are difficult to pattern and dry etch. More recently, contacts made with polysilicon have been shown to exhibit ohmic contact [88], forming an nN-heterojunction (Figure 3.19).

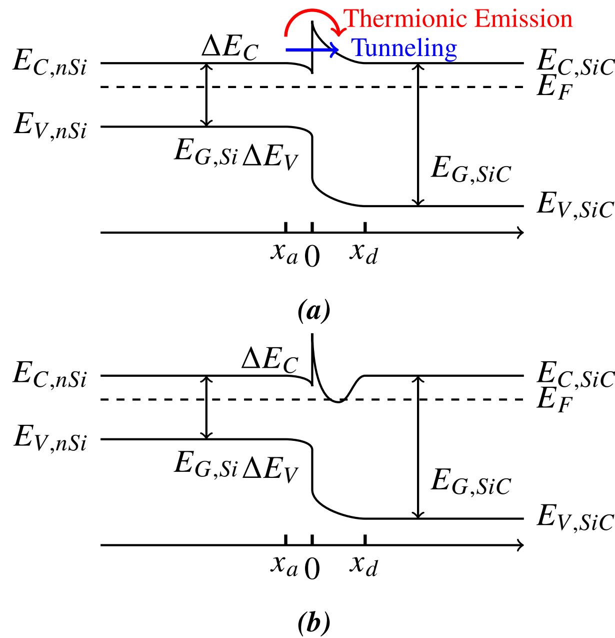

Figure 3.19. *(a) A straddling gap type n-N heterojunction with depletion width x_d and accumulation width x_a. The band discontinuities arise due to the mismatch between the valence and conduction bands of the two semiconductors, leading to a barrier height ΔE_C, the energy gap required for thermionic emission to occur. (b) Annealing at high temperatures aims to reduce effective barrier height by introducing carbon vacancies which act as electron acceptors.*

It's been shown that C vacancies C_V act as electron acceptors with ionization energy 0.5 eV below the conduction band whereas Si vacancies C_{Si} act as electron donors [89, 90, 91]. Thus rapid annealing at high temperatures to preferentially outdiffuse carbon is

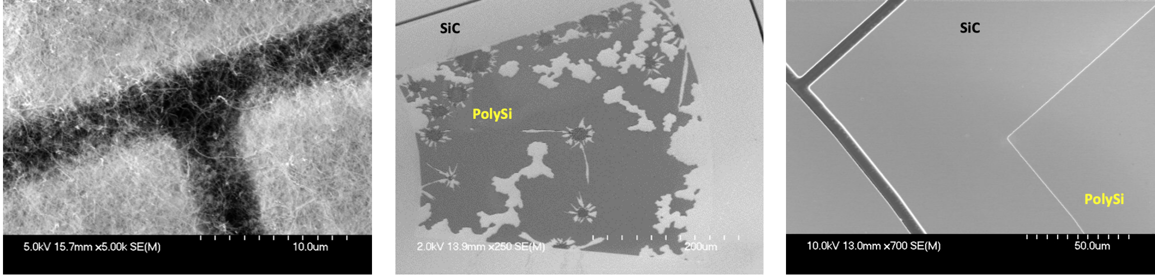

Figure 3.20. *(a) Nitridation of poly silicon in a nitrogen rich environment following rapid thermal processing at* 1200 °C*. (b) Significant damage to the polysilicon layer following HF cleaning and sonication. This affects not only ohmic contact, but roughness can make it extremely difficult to wirebond. (c) Depositing a PECVD protective film and limiting ambient N_2 flow prior to high temperature anneal can prevent nitridation.*

desirable to reduce effective barrier height ΔE_C (Figure 3.19). To that end, prior to all other processing, in-situ phosphorous doped n-type polysilicon is deposited via LPCVD and subsequently patterned via photoresist and dry-etched with SF_6 plasma. Finally, before HF release, the devices are annealed at 1200 °C for 5 min to allow diffusion of carrier species and outdiffusion of C to lower the Schottky barrier height [92, 93].

Nitridation of Polysilicon During high-temperature annealing at any step, one must be cognizant of the gas composition as silicon nitridation may occur at temperatures as low as 1100 °C and should be avoided at all costs [94]. Contingent upon tool capabilities, one can either reduce nitrogen flow or deposit a PECVD SiO_2 film can help prevent nitridation (Figure 3.20).

CHAPTER 4

SIC DISK RESONATORS FOR GYROSCOPIC APPLICATIONS

Silicon carbide is naturally well positioned to harness Q and translate it into high performance instruments and sensors. With that in mind, several disk designs were fabricated in ascending fabrication complexity with iterative simulation to understand and process results (Figure 4.1). These operate in the elliptical wineglass modes, with principal interest in the m = 3 gyroscopic modes, with intrinsically low thermoelastic, surface, viscous and mechanical losses.

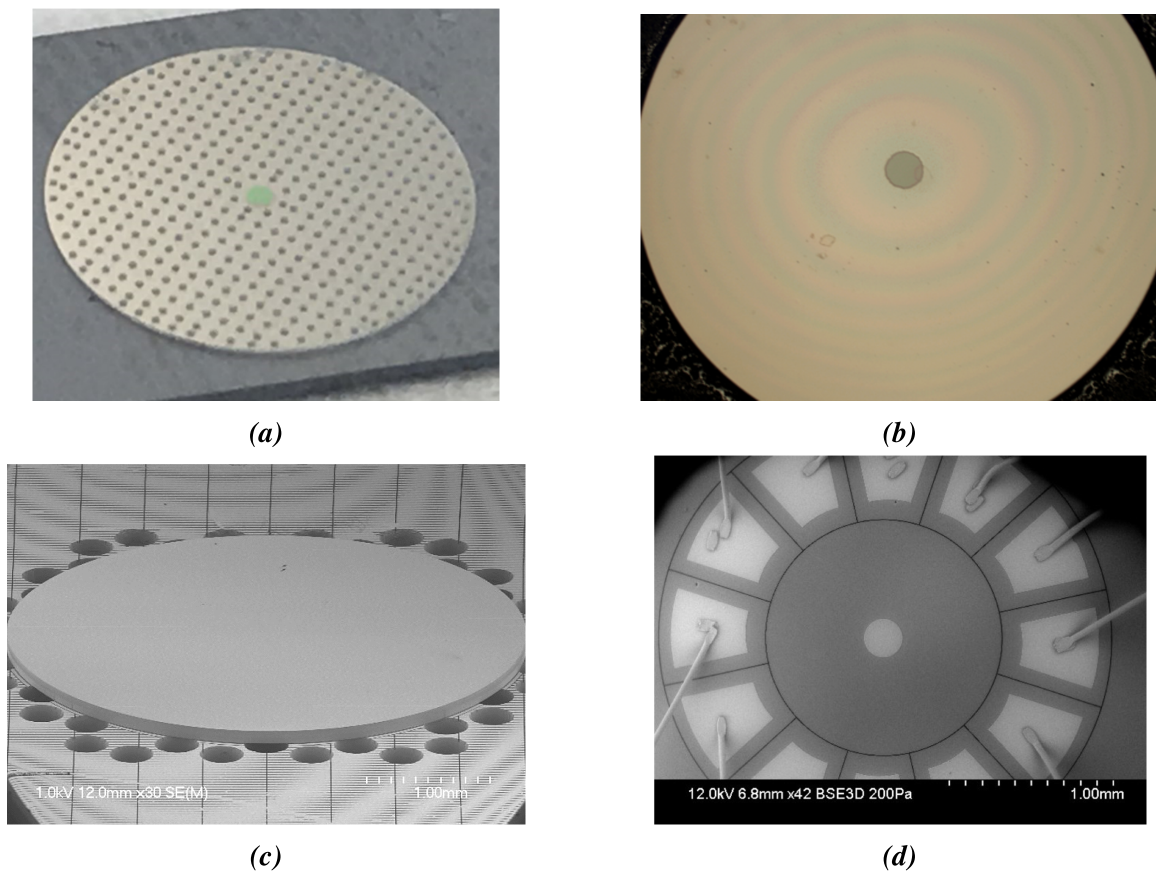

Figure 4.1. *Disks fabricated in chronological order: (a) perforated disks (b) Solid disks (c) solid disks on phononic crystal (d) capacitive disk on phononic crystal.*

The frequency of the wineglass modes can be calculated as follows, with full derivation in Appendix B:

$$f_m = \frac{k_m}{2\pi R}\sqrt{\frac{E}{\rho(1-\nu^2)}} \tag{4.1}$$

with k_m for different modes and materials in Table B.1.

4.1 Optically Transduced Disk Resonators

The first disks fabricated lacked backside alignment structures for release or substrate-decoupling and relied on either release holes or long releases, each with their own advantages and disadvantages (Figure 4.1(a,b)). These were largely proof of concept devices to corroborate simulation and design.

4.1.1 Disks with Release Holes

Disk resonators were fabricated after design and simulation in COMSOL multiphysics. Among the first were disks both with and without release holes which allow for simpler fabrication circumventing backside alignment and etching. Further, release holes are defined concurrently with the disk itself so as to produce a self-aligned oxide pedestal (Figure 4.2).

The disks are glued to shear-mode piezo-stages (Steminc®). The devices are placed in a vacuum chamber pumped down to sub-mTorr levels to obviate any loss by air damping. To measure frequency response, the S_{21} parameter is obtained by a network analyzer (Keysight®) which drives the piezo-stage via an amplifier. The velocity is then measured by a laser Doppler vibrometer (LDV, Polytec®) through the vacuum chamber's viewport and subsequently interfaced back with the network analyzer. The set up is depicted

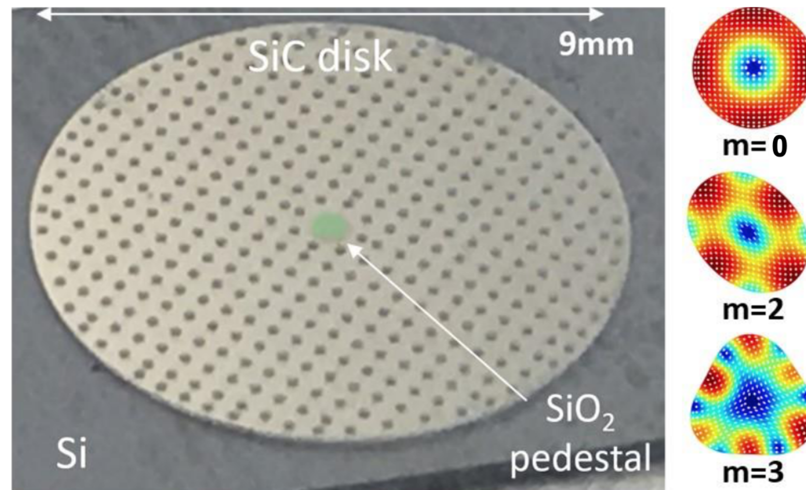

Figure 4.2. *Optical image of fabricated disk with release holes* 200 µm *wide in radius. Elliptical wineglass mode shapes simulated via COMSOL® are depicted on the right; the silicon oxide pedestal is shown in green [63].*

in Figure 4.3. Similarly, to perform ring-down measurements, the device is actuated at its resonance frequency and the driving signal is abruptly terminated. The device response is recorded, and its decay time is used to determine the mode's Q factor. Incidentally, the instrumentation was the largest factor determining design parameters; i.e. the amplifier and piezo-stage had operational frequencies below 1 MHz, setting the device diameter to 9 µm.

Frequency differences between measurements and COMSOL simulations range from 3.9%–6.1% as depicted in Figure 4.4(a). While the $m = 3$ modes are inherently degenerate

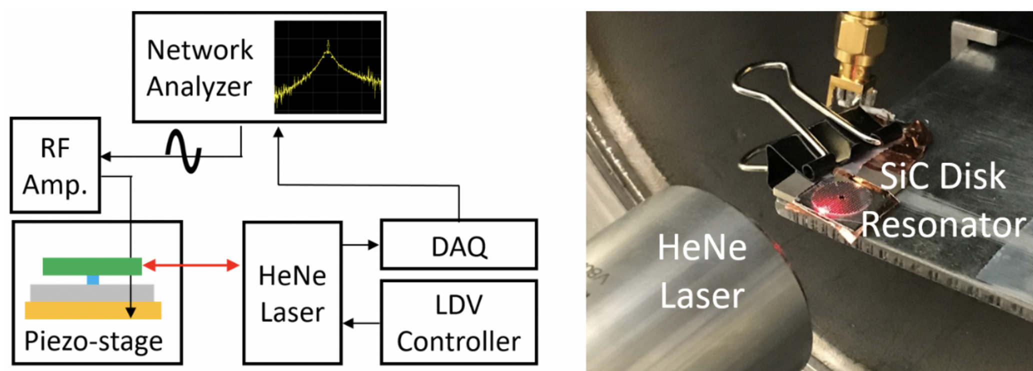

Figure 4.3. *Schematic (left) and photograph (right) of the LDV measurement setup [63].*

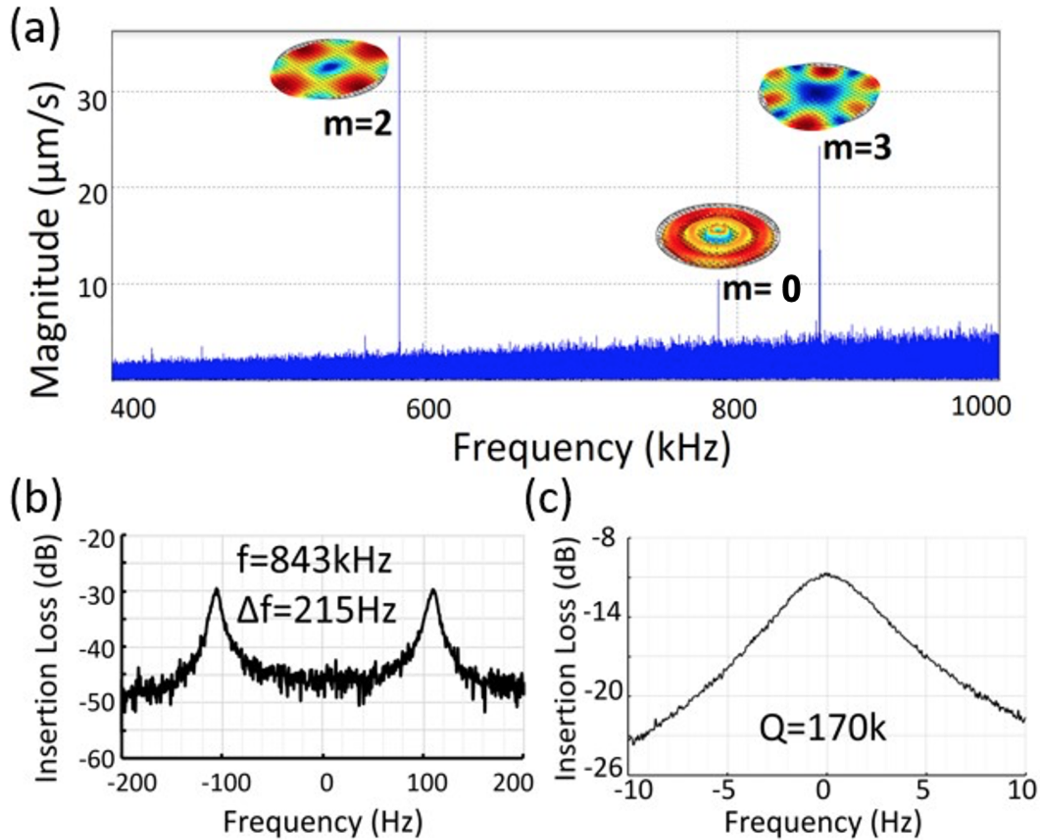

Figure 4.4. *(a) LDV spectrum of the perforated SiC disk with simulated mode shapes, (b) two degenerate peaks from the* $m = 3$ *modes, (c) its magnified view [63].*

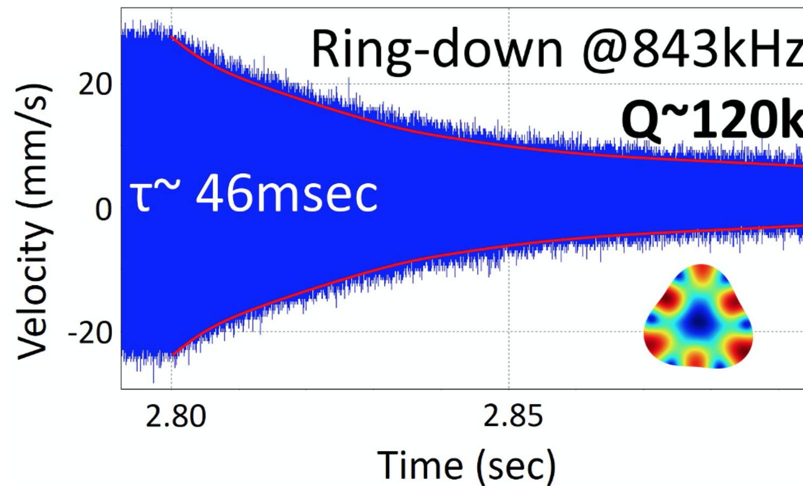

Figure 4.5. *Ringdown measurement of the fabricated disk. The amplifier is switched off at* 2.8 s *and the time response is measured. Eq.* (2.3) *yields a Q of* 120k*, matching simulation well.*

and mode-matched, the addition of release holes not only reduces their resonance frequencies but also induces a small frequency split. In Figure 4.4(b,c), two degenerate $m = 3$ Coriolis-coupled bulk elliptical modes in disk resonators have a resonance frequency of $f_{m=3} = 843\,\text{kHz}$, a Q of 170×10^3 and a frequency split of 215 Hz, equivalent to 255 ppm. The first elliptical modes ($m = 2$) show a resonance frequency of $f_{m=2} = 585\,\text{kHz}$, a Q of 59.7×10^3 and a frequency split of 62 kHz, equivalent to 10.6%. Since the $m = 2$ mode contains relatively large amounts of strain energy concentrated near the pedestal, the mode is particularly susceptible to fabrication errors (e.g. misalignment). As depicted in Figure 4.4, the height of its peak reflects its greater displacement relative to the other measured modes, corroborating theory [95].

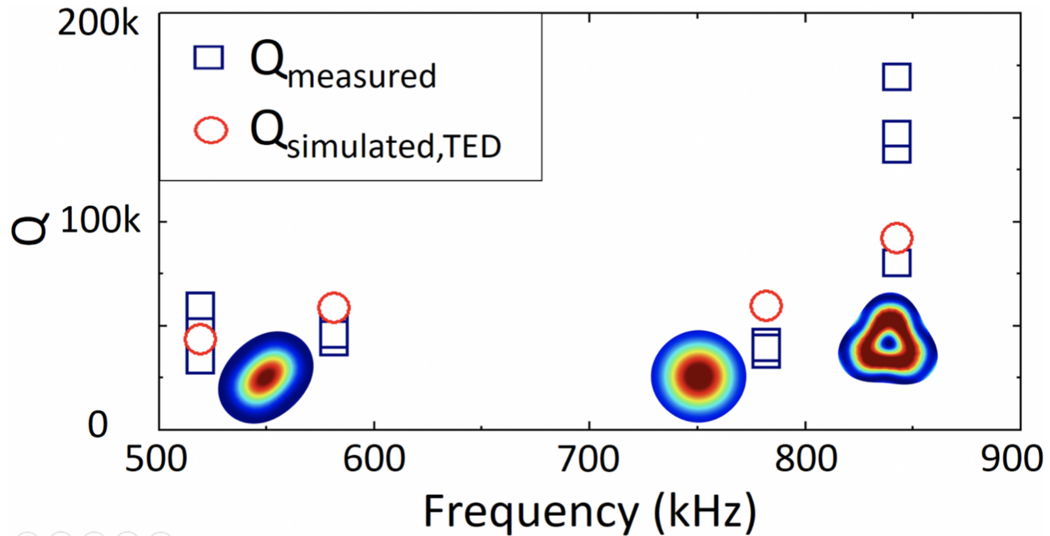

Figure 4.6. *Comparison between measurements and simulations. The strain energy density is concentrated near the pedestal for the first two elliptical modes resulting in lower $Q_{ANC(m=0,2)}$ compared to the m = 3 modes [96, 97].*

To determine the principal dissipation mechanism in these disk resonators, the simulated values of Q_{TED} of their respective BAW modes are depicted in Figure 4.6. Support losses, contingent upon the pedestal dimensions and other design considerations are simulated to be

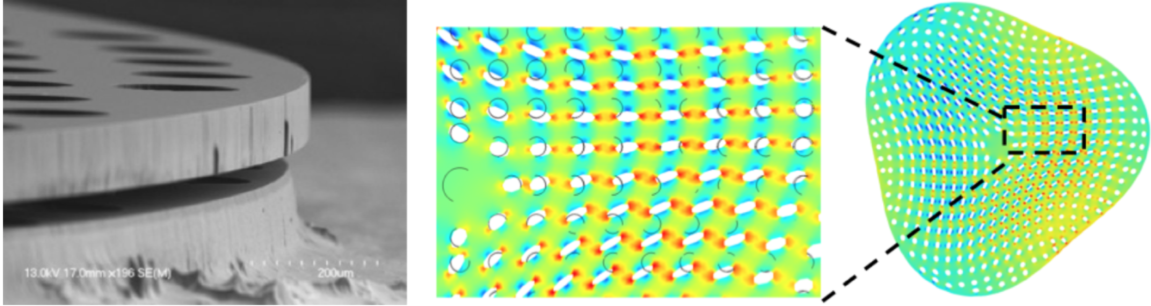

Figure 4.7. *SEM of* 9 µm *disk with release holes (left). COMSOL thermoelastic dissipation eigenmode simulation shows significant temperature and strain gradients due to introduction of release structures, reducing Q-factor from* $>100 \times 10^6$ *in a solid disk to* 170×10^3 *in a perforated disk.*

an order of magnitude higher than measured. In this analysis, the simulation overestimates the TED because of meshing that grossly approximates fabrication imperfections near the release holes. Most of the measured Qs are near the simulated Q_{TED} implying that devices are TED limited, given the added strain induced by the release holes (Figure 4.7). The highest measured Qs for the degenerate $m = 3$ mode are 170k and 135k across 6 measurements. At the time, this was the highest Q measured in SiC disk resonators, which had been limited to 51k in previous work [98].

4.1.2 Solid Disks

The next effort sought to investigate anchor loss and investigate higher Q by maintaining the disk's integrity. In centrally supported disks, the pedestal—as the mediator between the disk and the substrate itself— plays an enormous role in the disk's anchor loss [96]. Intuitively, a wider pedestal can be imagined as a greater conduit for in-plane elastic waves to couple to out-of-plane vibrations and drain energy out of the disk into the substrate; conversely, a narrow pedestal limits the window for strain energy to escape but harms structural integrity and can lead to device imbalances for electrical transduction. Akin to

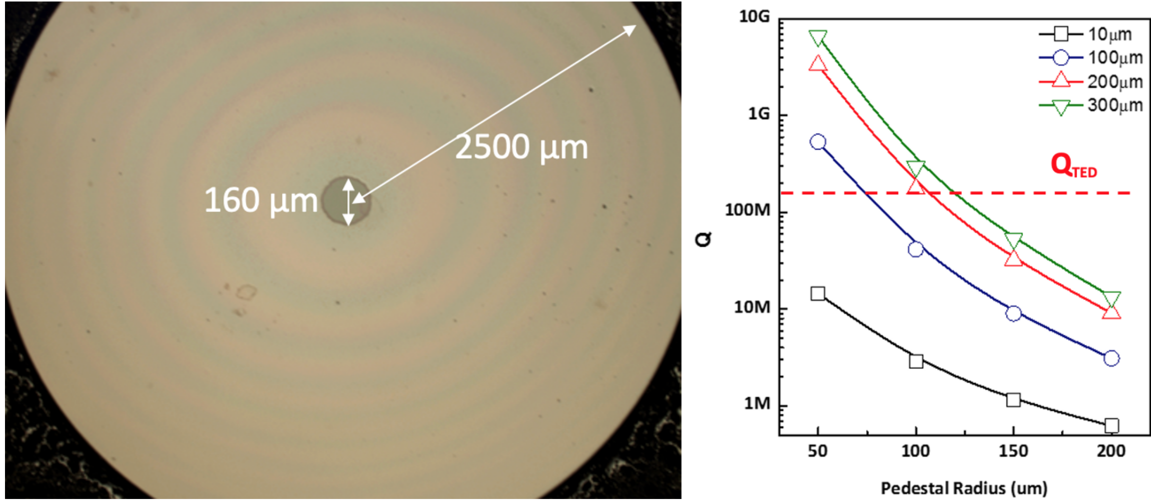

Figure 4.8. *(left) Optical image of a disk* 5 µm *in diameter and a pedestal* 80 µm *in radius with* 50 µm *misalignment due to spatially varying HF etch rates during release. Note the periodic color fringes due to constructive and destructive wave interference at the BOX layer; this indicates disk bending. (right) Curves of constant pedestal height plotting* Q_{ANC} *for varying pedestal radii. The dashed line in red is the* Q_{TED} *for the disk, unperturbed for variations at this size.*

a transmission line, Q_{ANC} varies periodically with pedestal height on the order of acoustic wavelength of the mode of interest. As our SiCOI substrates have a BOX layer on the order of several microns—a far cry from the typical acoustic wavelengths ~2 µm—this is largely ignored. TED and PML simulations were performed for a disk 5 µm in diameter across a variety of pedestal conditions (Figure 4.8).

As this device lacked both release hole perforations and backside holes, the release occurred over a period of eight hours, compared to thirty minutes for the previous disk with release holes. Non-uniform HF etch leads to a rather large pedestal misalignment of 50 µm as etch reagents and products have to diffuse in and out respectively. Misalignment is vastly detrimental to mode split and gyroscopic operation, though not impactful to a single mode's Q in this investigation. A variety of modes were measured optically (Figure 4.9,Figure 4.10) in a manner similar to devices in subsection 4.1.2 with measured Qs exceeding 2×10^6 for

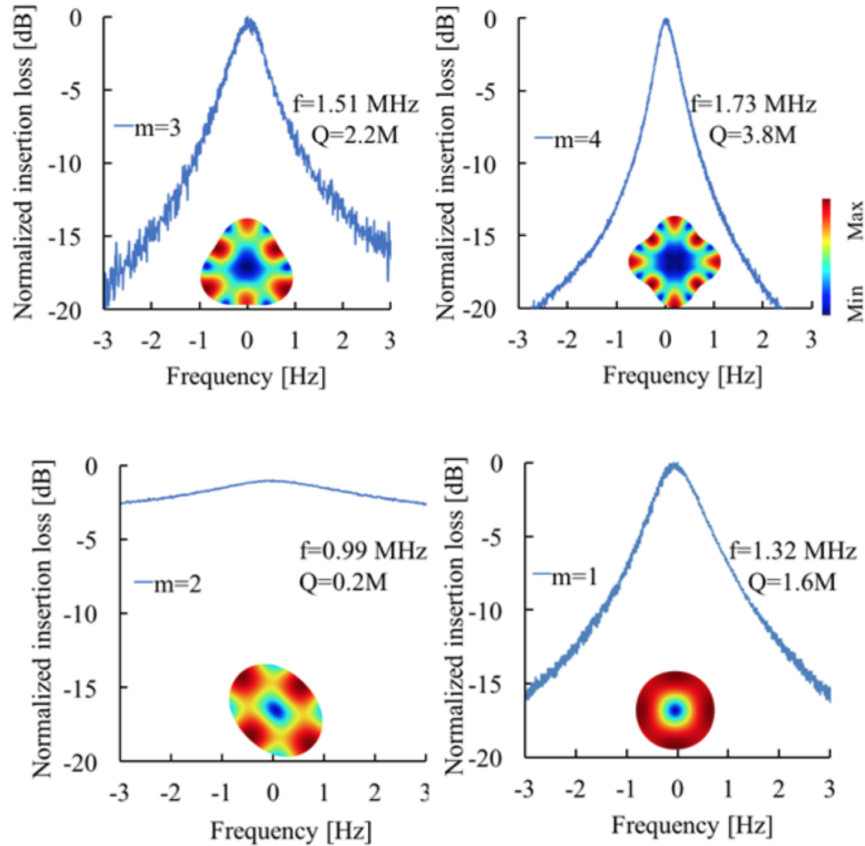

Figure 4.9. *Optically measured modes in a* 5 μm *diameter disk with neither frontside nor backside release holes. Qs are limited by anchor loss to the substrate and generally increase with increasing mode number (counter-clockwise from bottom left).*

the $m = 3$ elliptical mode.

4.2 Substrate Decoupled Disks: Design and Simulation

As depicted in Figure 4.10, solid disks without proper acoustic engineering suffer wildly from anchor losses and are the limiting agent in all of the measured elliptical modes. As such, limiting anchor loss becomes the task at hand in the effort to create ultra-high Q resonators. With a disk resonator centrally-anchored upon a matched handle layer composed of a phononic crystal structure, one can largely circumvent anchor losses, scaling a significant barrier toward inertial grade SiC BAW gyroscopes.

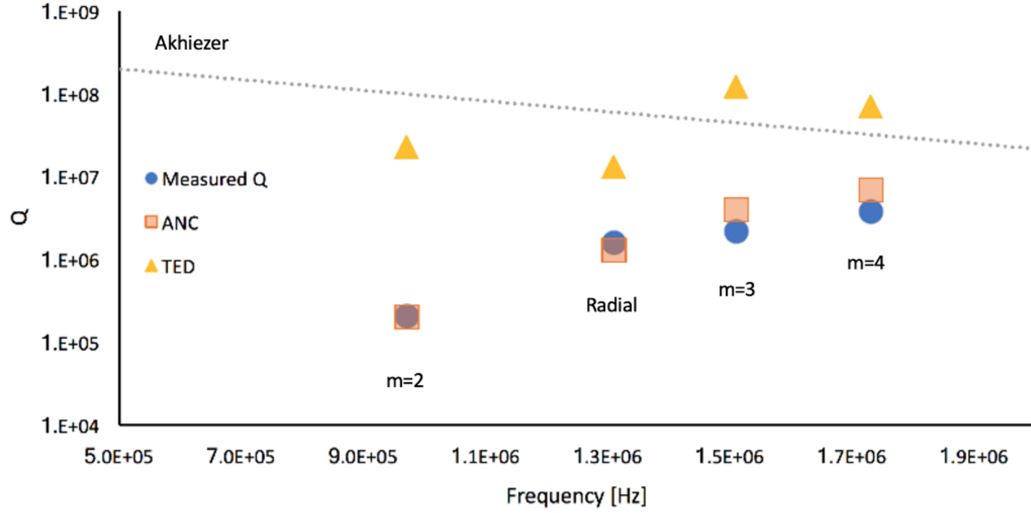

Figure 4.10. *Measured values of bulk elliptical modes compared with simulation of various damping mechanisms (ANC, TED, AKE). Q is limited by anchor loss in devices without substrate decoupling or frontside release holes. Grey dotted line depicts the Akhiezer fundamental limit.*

4.2.1 3D Substrate Decoupling for Anchor Loss

A phononic crystal (PnC) is a structure composed of stacked acoustically mismatched layers (superlattice) or a tessellation of periodic inclusions in an elastic medium. Analogous to a photonic crystal for electromagnetic radiation, the mismatch of acoustic impedance between the layers or inclusions reflects waves, introducing wave interference which creates the band gap of the PnC [99]. Prior to developments in micro and nanofabrication techniqutes, the majority of previously reported phononic crystal devices have been constructed manually, assembling scattering inclusions in a viscoelastic medium, predominantly air, water or epoxy, resulting in large structures limited to frequencies below 1 MHz [100]. However, recent work has explored applications including but not limited to: thermal phonon control for high ZT thermoelectrics for energy and cooling applications [101, 102, 103], acoustic isolation in MEMS [35, 36, 104], acoustic waveguides and focusing [105, 106, 107],

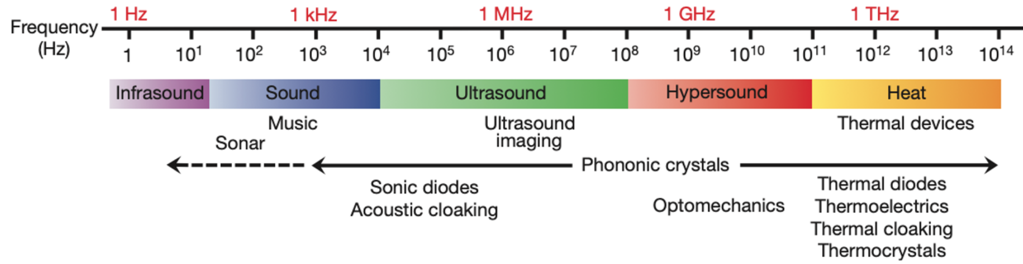

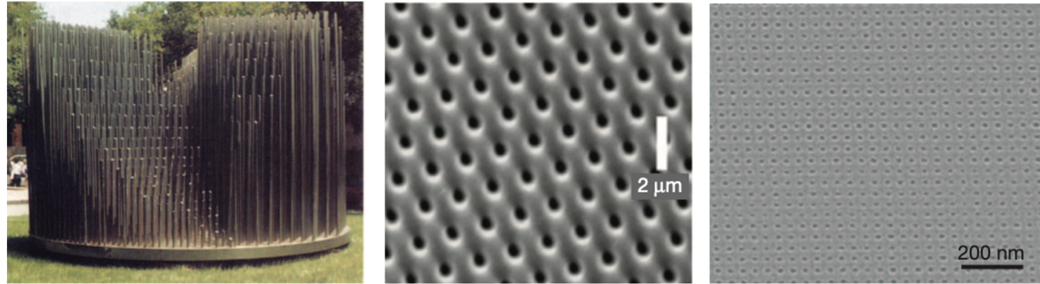

Figure 4.11. *(top) Phononic crystals have potential application across the phononic spectrum. Bottom left: periodic distribution of hollow stainless-steel cylinders, with a diameter of* 2.9 cm*, simple cubic symmetry and a unit cell of* 10 cm *exhibits attenuation peaks from* 1 kHz *to* 5 kHz *[100]. Bottom middle: epoxy with circular occlusions forming a triangular lattice fabricated via interference lithography with bandgaps* 1 GHz *[111] Bottom right: silicon nanomesh fabricated on SOI to mitigate thermal transport [102].*

and negative refraction for acoustic imaging [108, 109]. Theoretically and experimentally demonstrated, one may utilize a variety of solid and fluidic media to create stop bands in heterogeneous structures across the phononic spectrum (Figure 4.11). Further, while creating stop bands in fluids has been shown to be relatively straightforward, solids—which support both transverse and longitudinal waves—require more careful consideration [110].

Two critical parameters determine the behavior and characteristics of the band gap [112]: the center frequency and band gap width. The center frequency is defined principally by the characteristic unit cell length a, typically on the order of the propagating wave's wavelength. The width of the band gap is heavily affected by the acoustic impedance discrepancy between the propagating medium and the inclusions. I.e. the reflection and transmission coefficients can be expressed as a function of the two complex acoustic impedances ($Z_{1,2}$) of the two

media composing the interface:

$$
\begin{aligned}
R &= \left(\frac{Z_2 - Z_1}{Z_2 + Z_1} \right)^2 \\
T &= 1 - R
\end{aligned}
\tag{4.2}
$$

Caveat: for effective wave interference, the total size of the metamaterial structure must be below the phonon mean free path $l = v\tau_{phph}$, where v is the group velocity and τ is the phononic relaxation time [99]. This is typically only relevant for thermal vibrations which scatter strongly whereas acoustics and electromagnetics (incidentally) largely avoid this problem. Given that $\tau \propto 1/\omega$ and that devices in this work operate at low MHz frequencies with large group velocities exceeding 5000 m/s in silicon, we can safely ignore this consideration [113].

Using COMSOL, we can calculate and visualize the acoustic dispersion characteristics (i.e. frequency with respect to wavelength) within the periodic structure. This is accomplished via modified eigenvalue simluation based on Bloch-Floquet wave theory [114] across the irreducible Brillouin zone of the lattice following high symmetry lines, with the eigenmodes subsequently mapped onto momentum space yielding the bandgap (Figure 4.12).

For a given material composite, the filling factor (the ratio of the area of the inclusions to the area of the unit cell) is the primary parameter influencing the width of the gap. A structure's bandgap behavior can be described by its $f \cdot a$ product [Hz · m], as wavelength and frequency are inversely proportional. With increasing filling factor, the bandgap widens. Our design implements a honeycomb lattice, previously shown to offer the widest bandgap

at the lowest filling factor [115], conferring exemplary decoupling while maintaining device robustness.

The PnC design addresses the in-plane components of the energy lost to the substrate.

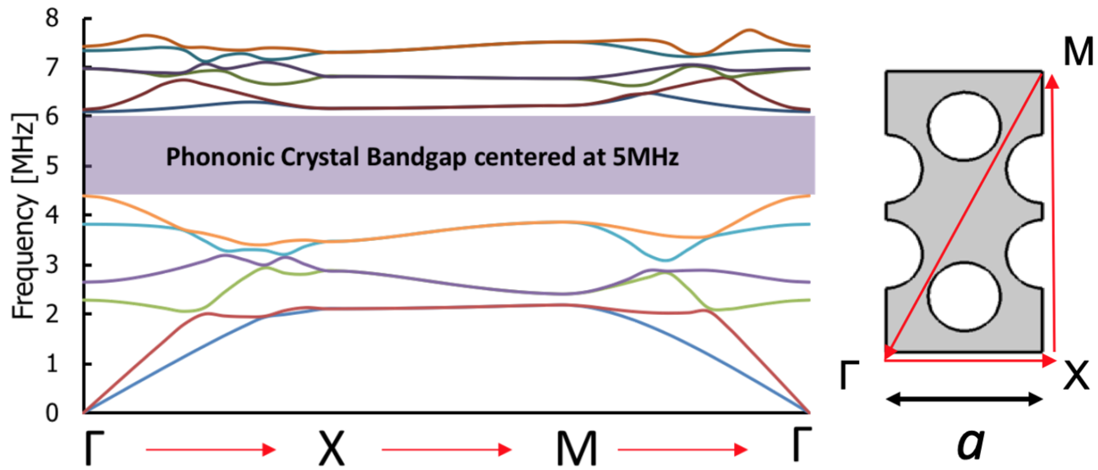

Figure 4.12. *(left) Eigenmode simulations using Bloch-Floquet boundary show a bandgap centered at* 5 MHz *for* $a = 420\,\mu\text{m}$ *for the honeycomb unit cell. (right) The unit cell with high symmetry points* Γ*, M and X. The eigenmode frequencies are found along paths between these points, garnering a complete picture of wave propagation within the cell. For illustrative purposes, the unit cell is depicted in real space and* ***not*** *k-space.*

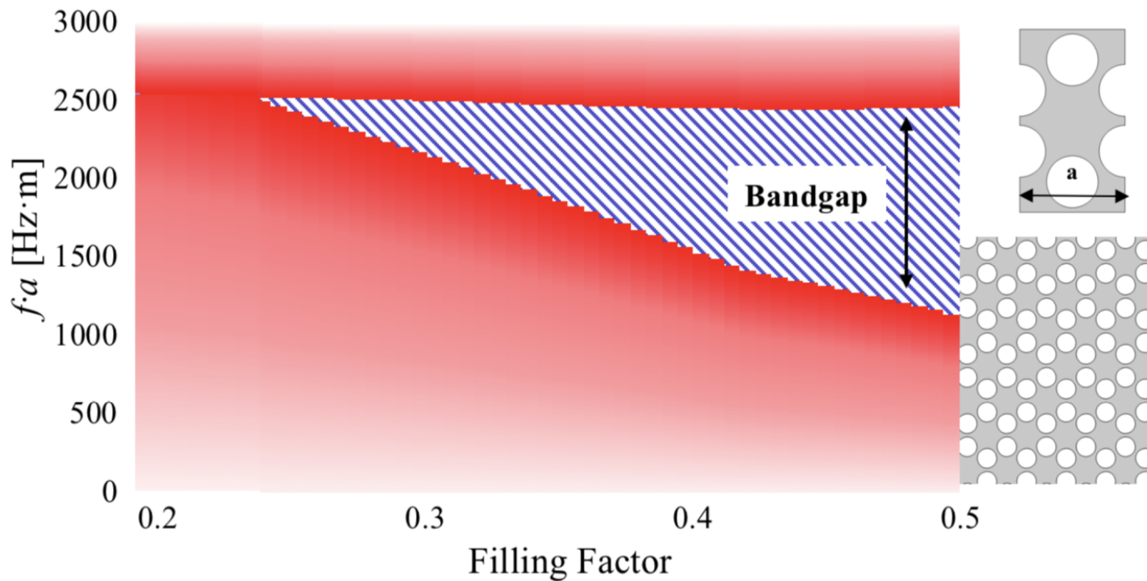

Figure 4.13. *The honeycomb lattice (right) offers the widest bandgap at the smallest filling factor. The unit cell, when placed in a rectangular lattice, creates a honeycomb tessellation (bottom right) [70].*

However, without proper vertical out–of–plane decoupling, anchor loss remains a significant issue. To enable vertical confinement, it is critical to match the thickness of the silicon handle layer to the quarter wavelength of the acoustic wave [116], determined by its frequency and the speed of wave propagation in silicon (Figure 4.14). By suspending the device in air to maximize acoustic impedance mismatch, the quarter wavelength roughly creates a standing wave with node and antinode at the surfaces of the handle layer, confining energy and elevating Q_{ANC}.

In perfectly matched layer (PML) simulation, the tandem of quarter wavelength matching and the PnC offer excellent substrate decoupling. Critically, placing more PnC unit cells in the decoupling layer offers greater opportunity for propagating waves to reflect and interfere, improving energy confinement. With a sufficient number of unit cells placed around the anchor of the disk, the disk can be made substrate "deaf," leaving the device limited exclusively by intrinsic dissipation mechanisms i.e. TED and AKE (Figure 4.15).

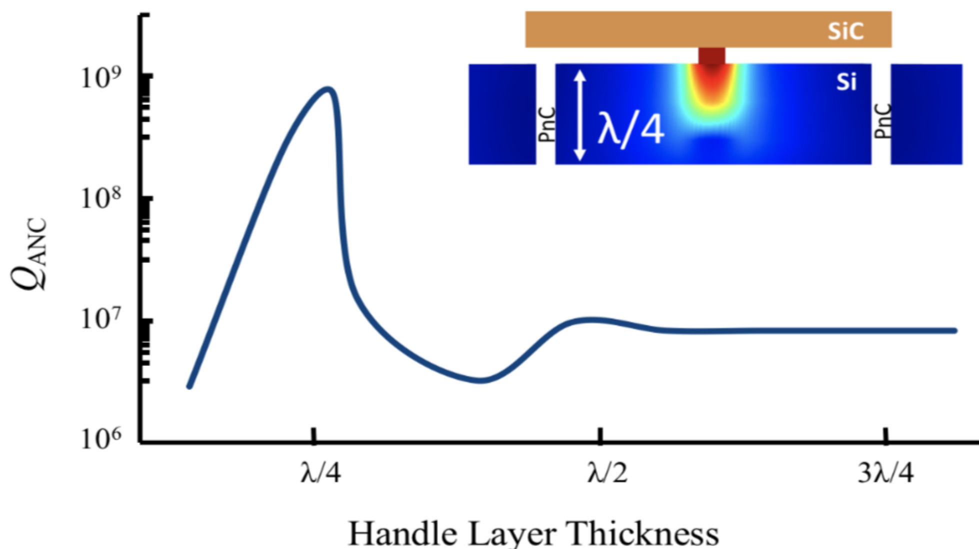

Figure 4.14. *Handle layer thickness affects Q_{ANC}. At $\lambda/4$, wave interference creates a standing wave with a node at the suspended end of the device. In concert with a PnC, anchor loss can be made negligible [70].*

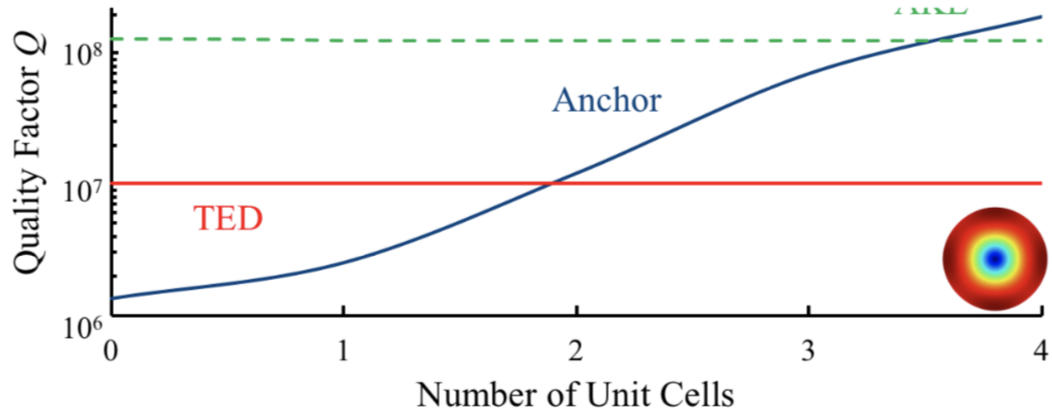

Figure 4.15. *As more unit cells are added, Q_{ANC} (blue) surpasses Q_{TED} (red) and finally Q_{AKE} (dashed green). In a* 1540 µm *diameter disk, radial mode at* 5 MHz *is TED limited [70].*

4.2.2 Results

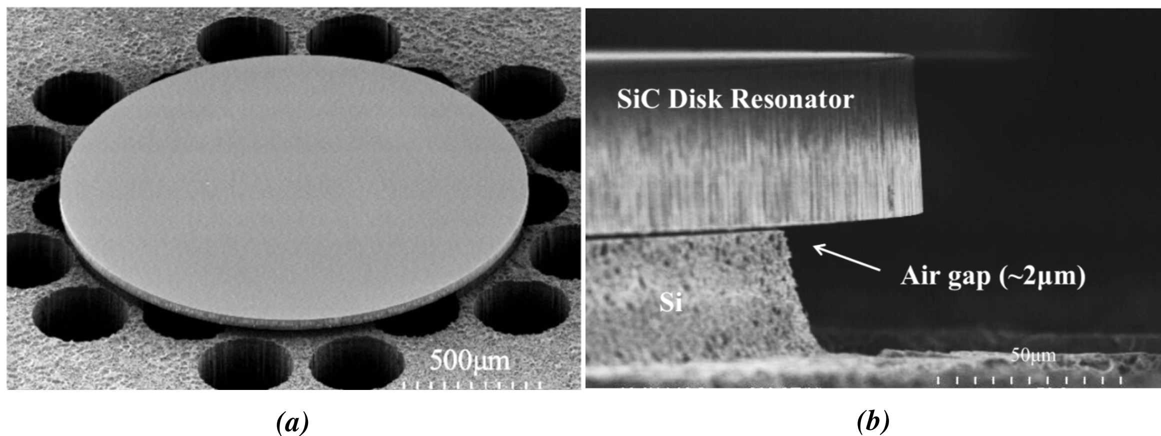

(a) ***(b)***

Figure 4.16. *(a) SEM of BAW SiC disk resonator (*100 µm *thick,* 1540 µm *diameter) anchored upon a phononic crystal of three unit cells. The radial mode resonates at* 5 MHz.*(b) The device rests upon the silicon handle layer with* 2 µm *gap determined by the thickness of the BOX layer. The lack of an etch stop manifests itself as over-etch into the silicon handle layer [70].*

Three devices of varying diameter were fabricated and tested (Figure 4.16), each aiming to position the radial, $m = 3$, and $m = 4$ modes at 5 MHz (1.56 mm, 1.7 mm, 2.21 mm respectively). The handle layer thickness of 500 µm determined the target operating frequency of 5 MHz with the PnC cell length $a = 420$ µm and a filling factor $\beta = 0.45$. Notably,

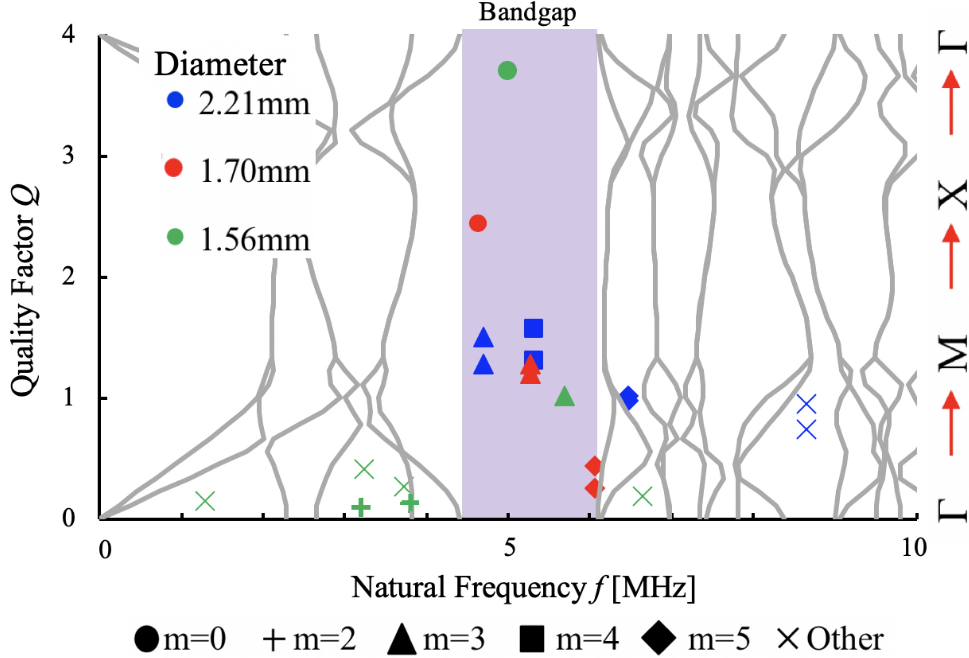

Figure 4.17. *Simulated dispersion curves (gray) depict frequencies of allowed propagation across the first Brillouin zone. Measured Qs of bulk modes across devices of varying size inside and outside the bandgap (purple). The breathing mode (m = 0) exhibits Q of* 3.7×10^6 *(green circle), perfectly coinciding with* $\lambda/4$ *frequency at* 5 MHz. *Modes operating away from the* $\lambda/4$ *frequency (m = 3 modes at* 5.3 MHz*) suffer in performance [70].*

the 1.56 mm disk displayed a breathing mode Q of 3.7×10^6 precisely at 5 MHz (Figure 4.18). Simulated with $Q_{ANC} = 350 \times 10^6$ and a limiting $Q_{TED} = 14 \times 10^6$ at 5 MHz, the Q discrepancy arises due to sidewall defects (discussed later). In contrast, recall the disk from subsection 4.1.2 (5 mm diameter) anchored upon an unmodified silicon substrate with smaller anchor diameter (3% of the device diameter) which demonstrated a Q ~1×10^6 at 1.7 MHz. Despite its larger size (less TED) and diminished pedestal area, the lack of any substrate decoupling bounds its Q to smaller values.

Measurement is predominantly similar to previous optical testing, though the device now demands new 5 MHz $LiNbO_3$ shear mode actuators from Boston Piezo-Optics® migrated to a network analyzer as the LDV's built-in fourier software lacked the required frequency

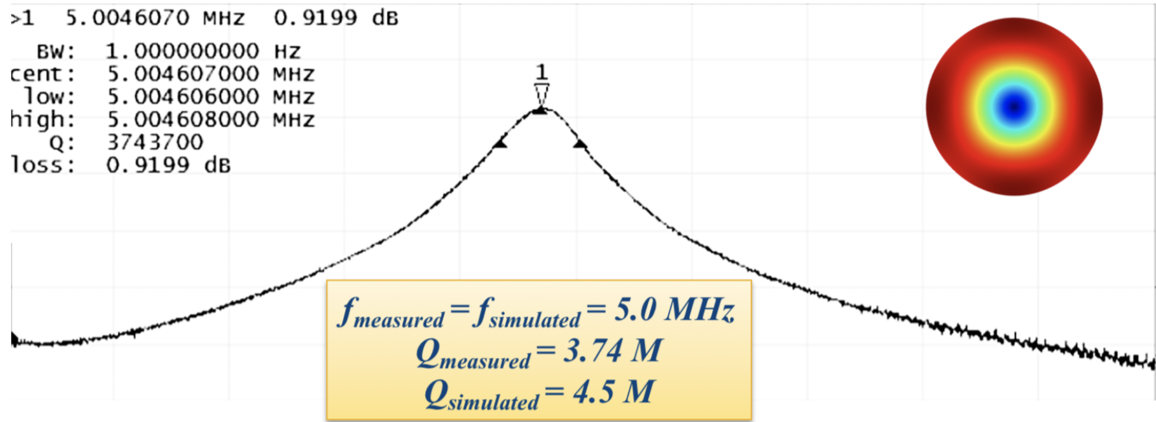

Figure 4.18. *Radial mode frequency response of a* 1540 µm *diameter disk with $f \cdot Q$ product of* 1.85×10^{13} Hz. *Measured Q and f corroborate simulation well. $Q_{simulated}$ incorporates fabrication defects [70].*

resolution necessary to measure such high Q-factors. Vibrational modes inside the bandgap show noticeably higher Qs relative to modes exterior to the gap (Figure 4.17), though the radial mode outperforms the others. While the radial mode frequency was accurately simulated, other bulk elliptical mode frequencies systematically diverged from simulation, again up to 6%. Nevertheless, measured frequency splits (Δf) are low for measured degenerate elliptical modes (Figure 4.19), showing 4H-SiC's suitability for mode-matched Q-amplified gyroscopic operation.

The resonance modes, while substrate-decoupled, deviate slightly from TED simulation, which is the predicted limiting mechanism. Upon examination, the disk showed fabrication non-idealities such as horizontal and vertical striation. Previous work has shown defects and asperities in shell resonators contribute significantly to TED [117]. While shells with surface roughness show Qs below 100×10^3 [43], attributable to a high surface area to volume ratio, the effect of surface defects on disks is less explored.

SEMs of the sidewall of these disks show striations on the micron scale. Q_{TED} monoton-

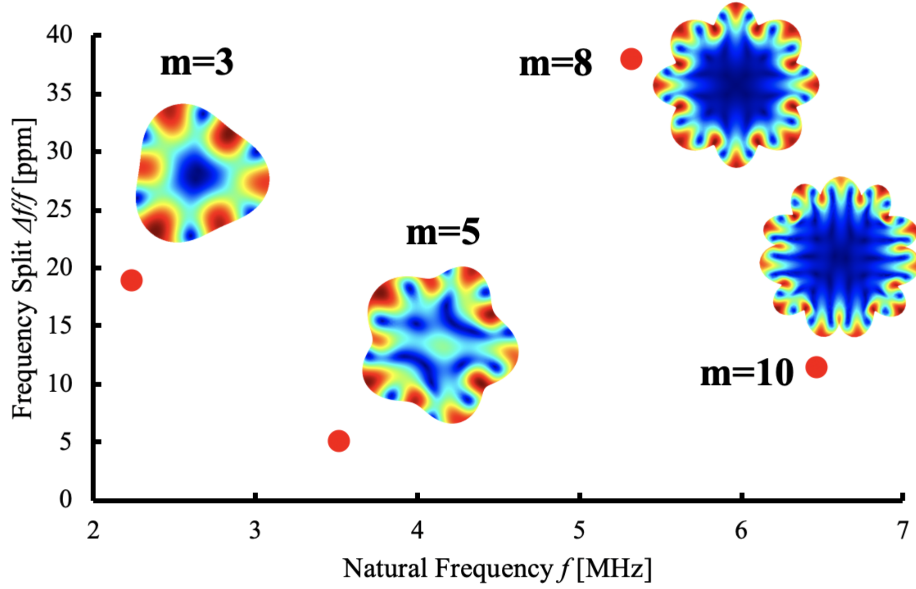

Figure 4.19. *Measured frequency split* $\Delta f/f$ *of several bulk elliptical modes below* 40 ppm. $m = 3$ *modes exhibit* 18 ppm *frequency split [70].*

ically decreases with increasing size, flattening to Qs in the millions. Horizontal striations appear when etching is disrupted and restarted, more easily obviated. Vertical striations however, could arise from a fusion of different sources: non-uniformities in the nickel mask that propagate during DRIE, in combination with charging in the passivation layer that segregates and directs plasma species imperfectly, result in a striated sidewall. In simulation, striations are modeled as a hemi-cylindrical defect on the sidewall of the disk, introducing additional strain coupling to thermal fields (Figure 4.20a). Current fabricated SiC disk resonators show defects ranging from 1 μm to 3 μm in lateral dimension (Figure 4.20b). TED simulations incorporating these defects yield a Q_{TED} of 4.5×10^6 for the radial mode at 5 MHz (Figure 4.18), confirming measurement as a TED limited mode.

Discrepancies in Q–particularly for the $m = 3$ modes–can be attributed to anchor losses due to fabrication and material non-idealities affecting the handle layer thickness, the disk frequency, and the PnC itself. Measured and simulated frequencies differ by up to 6‰;

e.g. the $m = 3$ degenerate modes were measured to be at 5.3 MHz rather than 5 MHz as simulated (Figure 4.17). Due to strong $\lambda/4$ dependence, operating at 5 MHz ($c = \lambda \cdot f$) is critical; in this case, resonance at 5.3 MHz rather than 5 MHz reduces Q_{ANC} by a factor of 3 (100M → 35M). Additionally, the dimensions of the tethers between occlusions in the PnC should be tightly controlled to avoid spurious modes in the handle layer near 5 MHz. As opposed to other bulk elliptical modes, the radial mode showed the greatest consistency with simulation in terms of f and Q. Potential sources of this disagreement such as residual stresses during fabrication or material properties will be explored and discussed in Chapter 5.

Further optimization of the DRIE step was necessary to mitigate any sidewall defects loading Q_{TED}. Another batch of disks showcasing more resonant modes within the bandgap were fabricated to attempt to exhibit higher Q-factors. A 4.05 mm diameter disk vibrating in the $m = 8$ elliptical mode showed a Q near 18×10^6, optically measured at 5.3 MHz for a $f \cdot Q = 9.5 \times 10^{13}$ Hz, (Figure 4.21). Its frequency spectrum shows a clear peak in Q factors of various elliptical modes within the bandgap, demonstrating the effect of the phononic

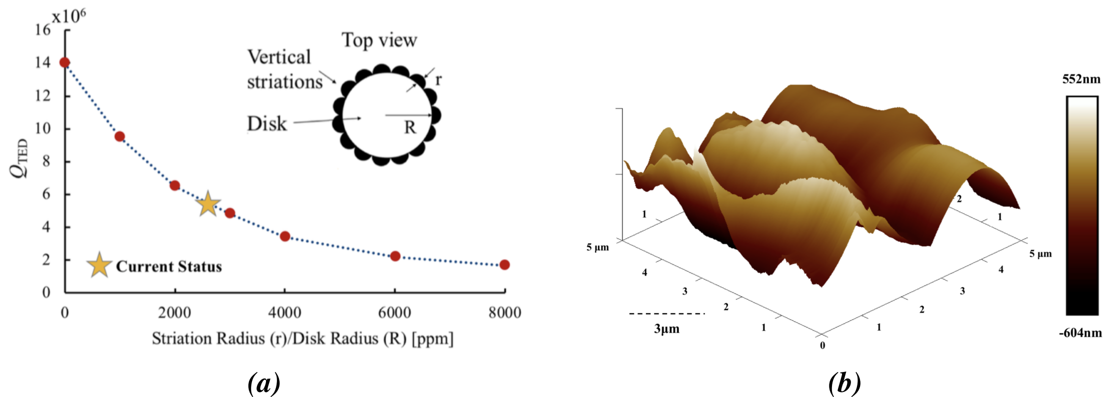

Figure 4.20. *(a) With increasing striation radius/disk radius ratio, simulations show a precipitous reduction in Q_{TED} of the radial mode. (b) Atomic force micrograph of the sidewall of the disk showing striation and roughness on the micron scale [70].*

crystal centered at 5 MHz (Figure 4.21b).

Measuring this Q required the resolution of many experimental challenges. Despite its extremely high Q factor, the resonant peak was rather difficult to actuate given its isolation from the piezostage due to the phononic crystal. Consequently, it was necessary to apply copious amounts of power to the actuator, producing temperature and frequency instability.

In general, higher order elliptical modes possess lower anchor losses, with the bulk of their deformation concentrated near the circumference rather than the near the center support. Simulation comparing the $m = 3$ and $m = 8$ modes across fabrication variations such as disk size (thus, frequency), and handle layer thickness corroborate this, demonstrating

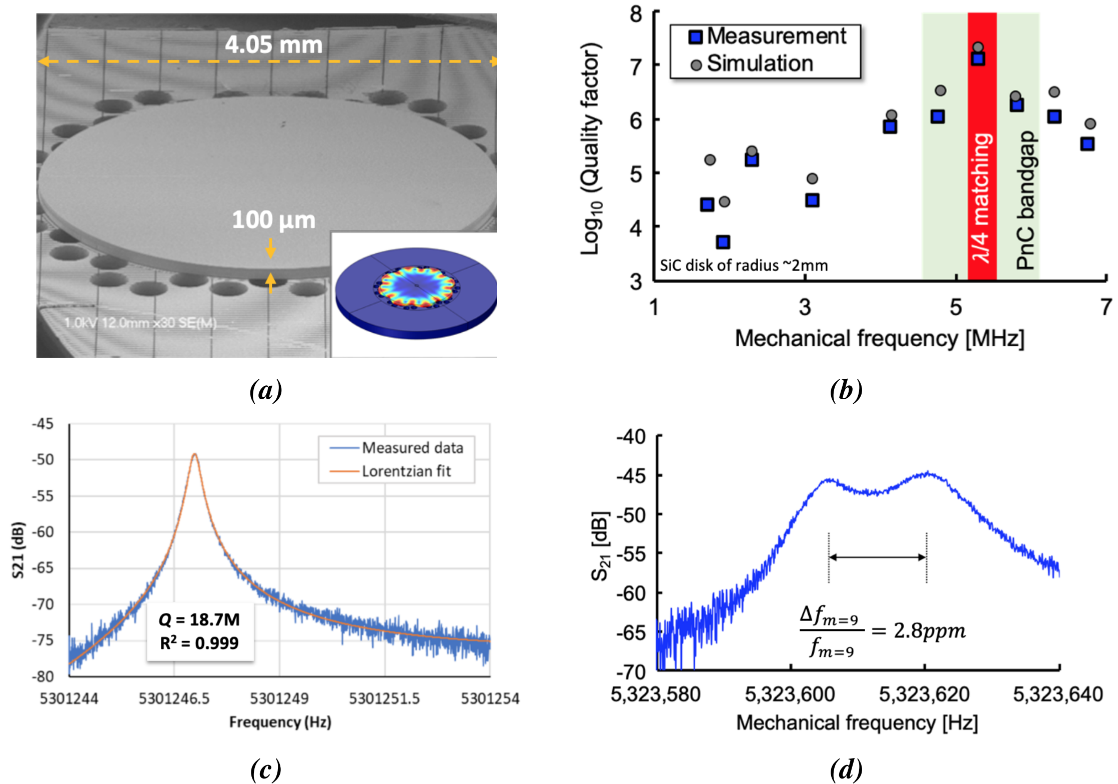

Figure 4.21. *(a) SEM of* 4.05 µm *diameter SiC disk resonator with simulated $m = 8$ mode shape (inset). (b) Spectrum of measured elliptical modes showing the highest Q within the bandgap and—more specifically—the $\lambda/4$ matching. (c) $m = 8$ resonant mode with a measured Q of* 18.7×10^6 *corresponding to* $f \cdot Q = 9.5 \times 10^{13}$ Hz. *(d) Frequency split of odd-numbered elliptical modes are low; in this case,* 2.8 ppm *for the $m = 9$ mode [71].*

the relative difficulty in measuring the same Q in the $m = 3$ mode. A better understanding of SiC's elastic matrix, unqualified control of SiCOI specifications, as well as a fully developed fabrication process flow will allow for experimental confirmation.

4.2.3 Experimental Confirmation of Transverse Isotropy

Referring back to section 3.2, 4H-SiC is a transversely isotropic material. A 1.64 mm-diameter disk on PnC (Figure 4.22) demonstrates this with frequency splits below 10 ppm for odd-ordered modes and 150 ppm for even-ordered modes (in Si, even-ordered modes have frequency splits in excess of 10 000 ppm).

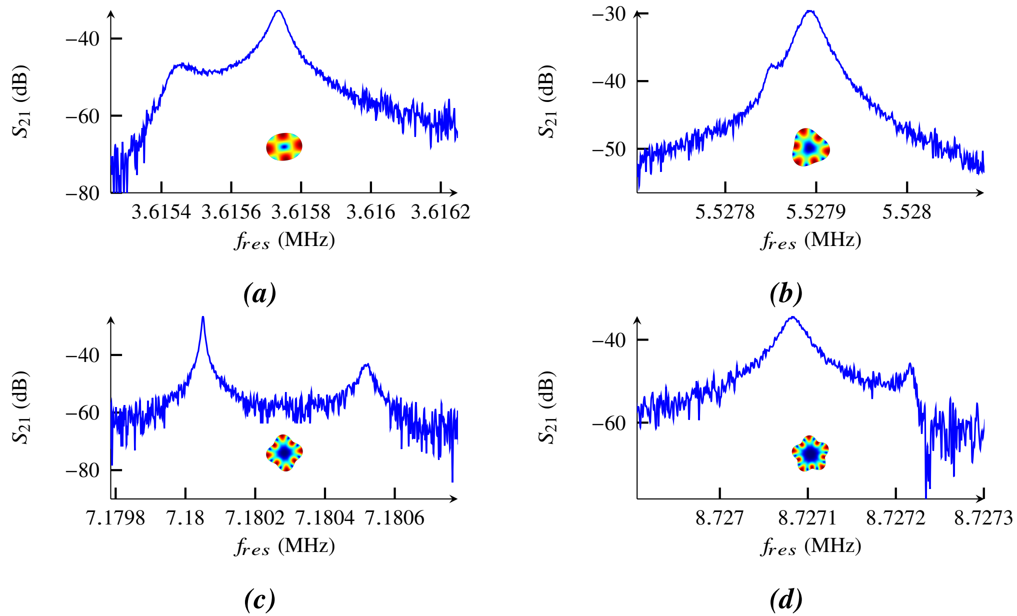

Figure 4.22. *Optically measured peaks in a* 1.64 mm *diameter disk exhibiting small frequency splits below for both even and odd-ordered modes (a)* $m = 2$ *mode at* 3.61 MHz *with* $\Delta f/f = 110$ ppm. *(b)* $m = 3$ *mode at* 5.52 MHz *with* $\Delta f/f = 9$ ppm. *(c)* $m = 4$ *mode at* 7.18 MHz *with* $\Delta f/f = 63$ ppm. *(d)* $m = 5$ *mode at* 8.73 MHz *with* $\Delta f/f = 14$ ppm.

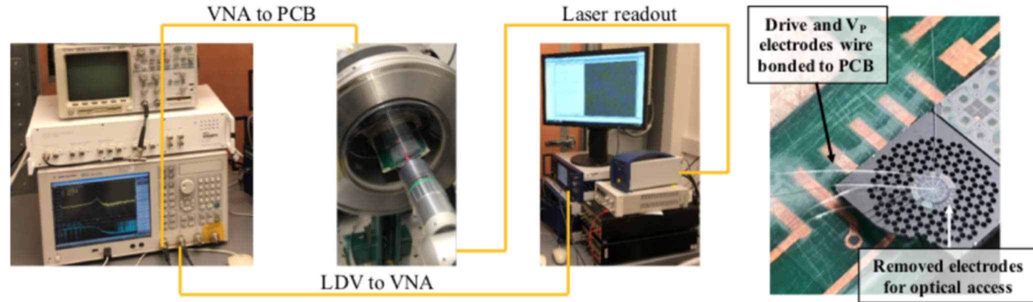

Figure 4.23. *Setup for capacitive actuation and optical readout along with optical image of disk [122].*

4.3 Capacitively Transduced Disk Resonators

Fabrication non-idealities like crystal misalignment or imperfections introduced that occur during lithography and etching introduce frequency split as well as cross-coupling between the two resonant modes, compromising mode-matched Q-amplified performance. Consequently, it's necessary to place electrodes around the disk to enable gyroscopic operation, allowing for transduction of the Coriolis-coupled modes as well as the ability to tune the frequencies via the spring-softening effect [118]. This section will review efforts to fabricate and measure capacitively transduced disks and their associated challenges.

4.3.1 Capacitive Actuation and Optical Sensing

The first efforts toward capacitive transduction actually used optical sensing via LDV due to its greater sensitivity (Figure 4.23). Again, this was meant more as proof of concept; though optical sensing has been demonstrated in integrated Coriolis force gyroscopes [119], this would add significant complexity. Incidentally, SiC is an exemplary optical material used in power electronics and under active investigation for high energy optics due to its wide bandgap, and advantageous thermal properties [120, 121].

With aspect-ratio limited capacitive gaps > 9 µm in a 100 µm thick SiC device layer, motional resistances would be enormous and inaccessible to even TIA-assisted capacitive transduction. Therefore, optical pickoff coupled with capacitive actuation allowed for measurement of 1.64 mm diameter disks with a variety of modes (Figure 4.24). As the introduction of gaps adds appreciable fabrication complexity affecting sidewall profile, roughness and quality, measured and expected Q values were low, but frequency splits were well in-line with prior measurement.

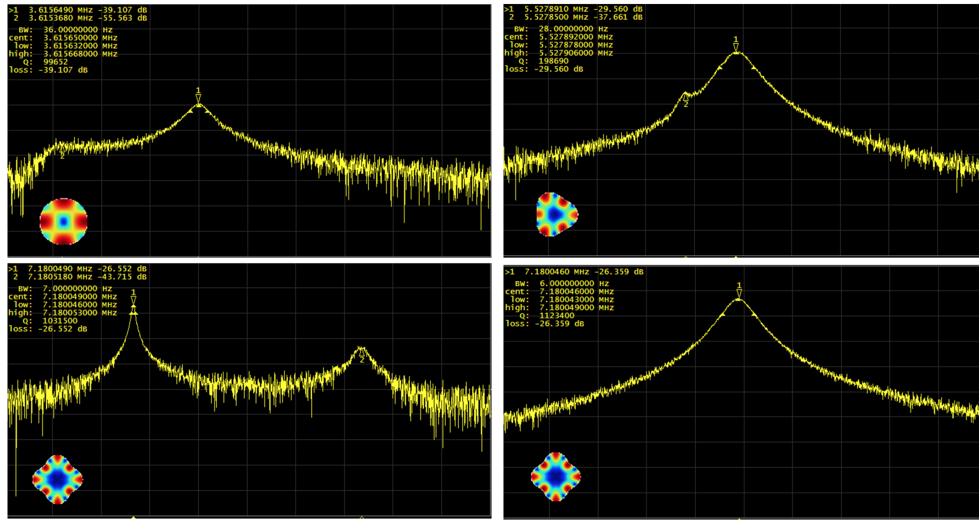

Figure 4.24. *Optically measured peaks show low frequency splits and good frequency agreement with simulation. (top left)* $m = 2$ *mode with* $Q = 99 \times 10^3$ *and* $\Delta f / f = 50$ ppm. *(top right)* $m = 3$ *mode with* $Q = 199 \times 10^3$ *and* $\Delta f / f = 8$ ppm. *(bottom)* $m = 4$ *mode with* $Q = 1.1 \times 10^6$ *and* $\Delta f / f = 65$ ppm.

4.3.2 Capacitively Transduced Disks on PnC

Continuing development of the fabrication of SiC and its associated challenges enabled higher aspect ratio gaps for full capacitive transduction of SiC disk resonators (Figure 4.25). The design parameters are delineated in Table 4.1 with an expected TED-limited Q of 45×10^6 though fabrication imperfections will serve to dampen practical measure-

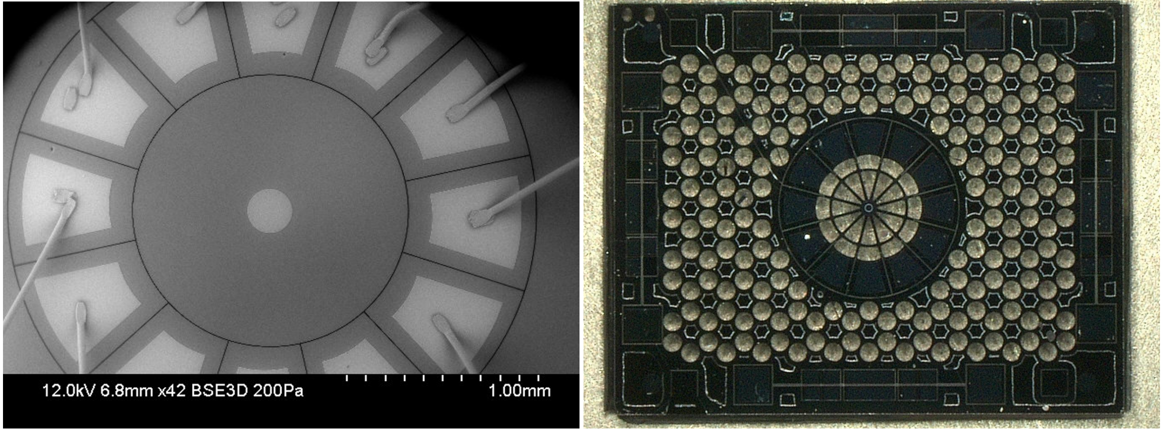

Figure 4.25. *(a) Variable-pressure SEM (to minimize charging) of capacitive disk with wirebonded drive and sense electrodes for degenerate $m = 3$ modes; the poly plug cap is in the center. (b) Optical image of the disk. SiC's wide bandgap and the device layer's smoothness renders it transparent to visible light revealing the PnC and the spoke release configuration below the disk. Fixed-fixed cantilever test structures surround the device.*

ment. Note that availability of phosphorous doped n-type silicon wafers with ultra low total thickness variation enforced the handle layer thickness to 380 µm heavily influencing the rest of the design flow. In Table 4.1, one may imagine the design flow from top to bottom with the handle layer thickness determining disk frequency, radius and PnC dimensions. Iterative simulation/calculation of expected Q should follow each design step.

Critically, measurement of these disks takes place on a PCB with input buffers and transimpedance amplifier (TIA)-assisted sensing necessary to contend with the inherently high R_m in BAW disks. Combined with a TIA, insertion loss of the resonator becomes:

$$IL = 20 \log_{10} \frac{R_m}{R_f} \tag{4.3}$$

where R_m is the motional resistance of the resonator and R_f is the TIA feedback resistor. Figure 4.26 illustrates the basic setup: the device is suspended via copper tape to further

Table 4.1: Device parameters and Q simulation for fully capacitive disks with 3D substrate decoupling fabricated on SiCOI.

Parameter	Unit	Value
Silicon handle layer thickness	µm	380
Silicon carbide device layer thickness	µm	55
Frequency of $m = 3$ mode ($f_{m=3}$)	MHz	6.3
Disk radius (R)	µm	720
Pedestal radius	µm	50
PnC unit cell length (a)	µm	360
PnC filling factor (β)	1	0.47
Gap size	µm	4.5
Anchor/Support Loss (Q_{ANC})	1	2×10^9
Squeeze film damping sub-mTorr (Q_{SFD})	1	1×10^9
Bulk TED (Q_{TED})	1	20×10^6
Surface TED ($Q_{SurfTED}$)	1	10×10^6
Polarization Voltage (V_P)	V	25
Predicted motional resistance (R_m)	MΩ	16

enhance any substrate decoupling and electrically polarized via poly plug (subsection 3.4.4). Additionally, poly plug self-aligns the pedestal to the disk in the same lithography layer, greatly minimizing pedestal misalignment.

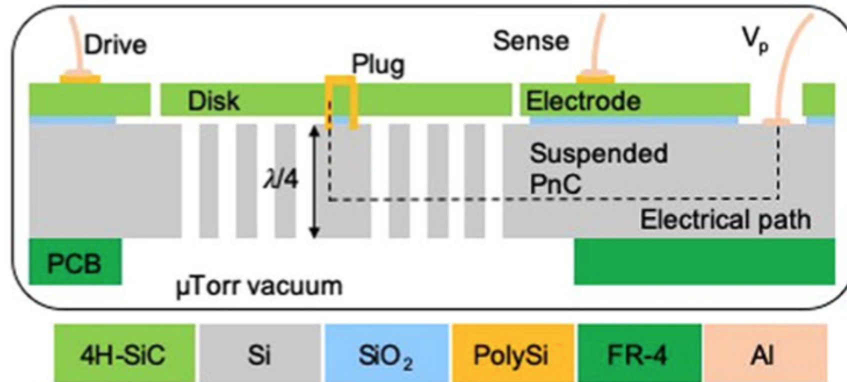

Figure 4.26. *Schematic for capacitive transduction of a disk resonator in 4H-SiCOI substrate [71]. The poly plug allows application of V_P without requiring wirebonding to the center of the disk.*

To test the disks, pairs of electrodes 180° apart were iteratively wirebonded to test for electrical shorts and—if open—used for drive and sense to measure the disk's S_{21} response

through a network analyzer. Electrodes are always utilized in pairs: if the electrode needs to be shorted to V_P due to some fabrication non-ideality, its sister electrode needs to be biased accordingly to maintain the disk's balance.

Six disks were successfully tested with Q-factors of the $m = 3$ modes consistently above 2×10^6. Figure 4.27 shows the electrical frequency measurement of an average capacitive SiC BAW disk resonator. The highest Q measured in a capacitive disk is 3.8×10^6 with frequency variations within ±40 ppm across all devices, demonstrating that the frequencies are remarkably robust to process variations. The average $m = 3$ frequency split measured was 26 ppm with the smallest measured as-born $m = 3$ frequency split at 13 ppm, likely resulting from symmetry-breaking fabrication imperfections. These low intrinsic frequency splits bolster 4H-SiCOI substrate's amenability to support degenerate Coriolis-coupled secondary elliptical modes in center-supported disk resonators. Other vibrational modes were probed, though due to the electrode configuration tailored for the $m = 3$ mode and low Qs (presumably anchor loss limited), results were limited. That said, the 5.5 MHz radial mode was measured with Qs approaching 750×10^3, lower than the $m = 3$ modes due to the resonance frequency lying outside the 1.5 MHz-wide PnC bandgap centered on 6.29 MHz.

4.4 Sources of Frequency Split

Frequency splits can arise from a number of sources: release holes which change the effective stiffness non-uniformly (subsection 4.1.1), fabrication non-idealities, etc. As described in section 3.2, elliptical modes in 4H-SiC should show no frequency splits and in fact do show smaller frequency splits of 22 ppm than their Si counterparts [19, 60]. This

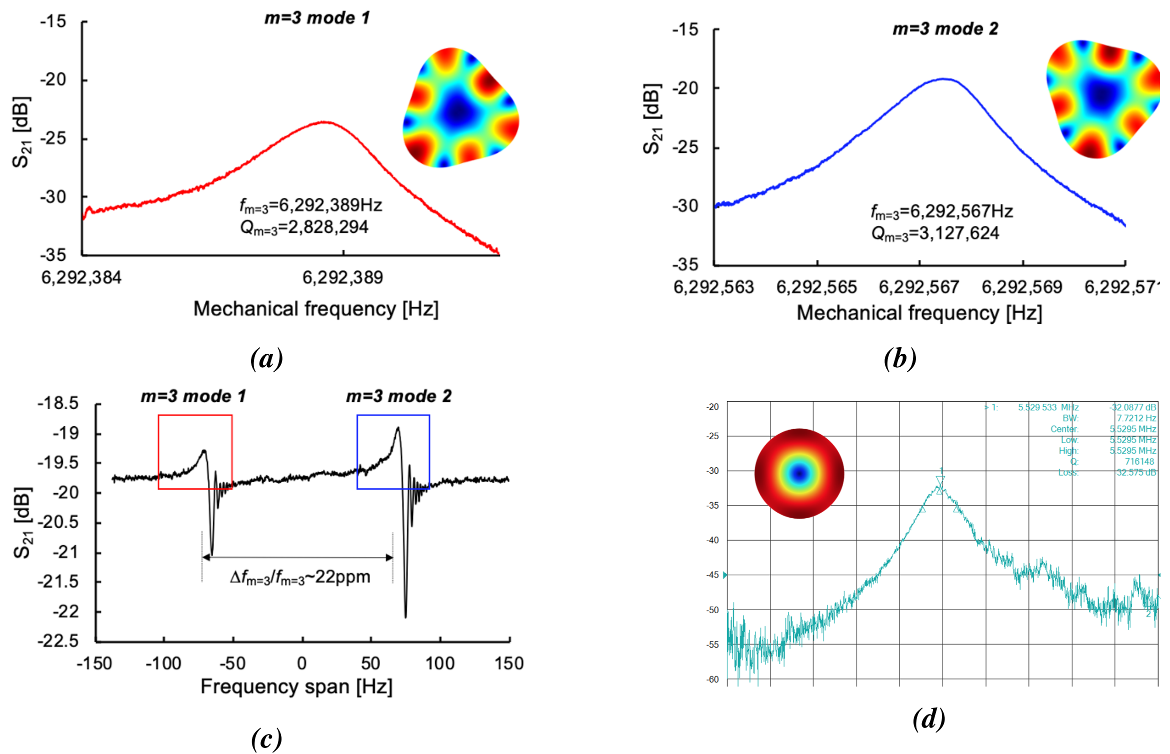

Figure 4.27. *(a,b) Degenerate* $m = 3$ *elliptical modes with* Q *in excess of* 2.8×10^6*. (c)* S_{21} *frequency response showing an as-born* $\Delta f / f$ *of* 22 ppm*. (d) Frequency response of radial mode at* 5.5 MHz *with* $Q = 750 \times 10^3$*, mirroring simulation well.*

raises the question as to the provenance of frequency splits Δf in hexagonal silicon carbide.

CHAPTER 5

ULTRA-HIGH Q ELECTROSTATIC SILICON CARBIDE LAMÉ MODE RESONATORS

Micromechanical resonators with ultra-low dissipation play a critical role in a plethora of applications including, but not limited to: navigation in extreme, GPS-occluded environments and low-power precision timing references. Silicon (Si) is currently the preeminent choice for batch fabrication of micromechanical resonators, largely owing to its ease of fabrication and wafer-level patterning with nano-scale precision [7]. However, ultra-low dissipation in Si has plateaued, reaching an $f \cdot Q$ of 2.8×10^{13} Hz at 120 K [123]. With the demand for MEMS instruments ever growing, monocrystalline silicon carbide (SiC) is making its case as a promising material to surpass this most basic limit placed upon Si, as its fundamental quantum Akhiezer ceiling is a staggering 30× higher than that of Si [20].

In Chapter 4, disk resonators operating in their bulk elliptical modes show relatively high Q, but are highly susceptible to surface roughness effects [71]. Square resonators serve as an ideal test vector to elucidate the limits of mechanical dissipation and the suitability of thick on-axis monocrystalline 4H-SiCOI substrates for high-precision SiC MEMS instruments. Additionally, square resonators can also divulge information regarding the mechanical properties of 4H-SiC, something that is nowhere near as well understood as silicon, the preeminent integrated MEMS material. This chapter will explore the design and fabrication considerations of square resonators in thick SiCOI substrates with a heavy focus upon the Lamé mode.

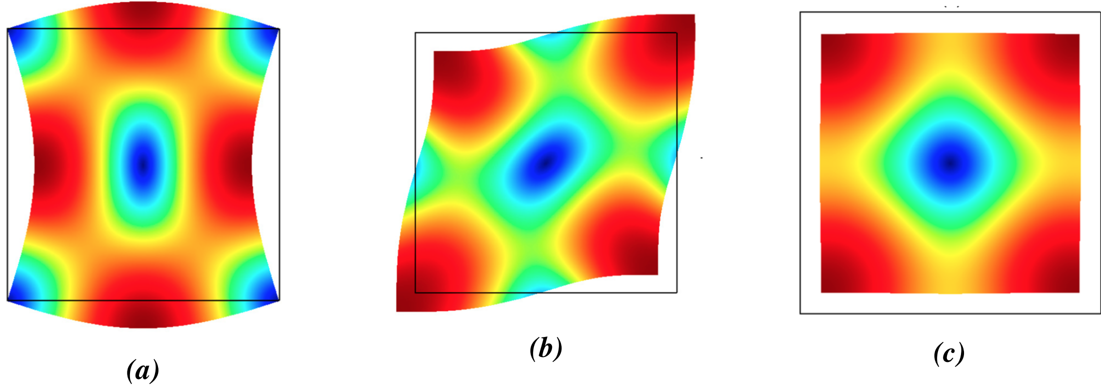

Figure 5.1. *(a) Lamé mode with four nodal points ideal for anchoring. (b) Face shear mode. These two modes characteristically show simultaneous contraction and expansion between two orthogonal axes. (c) Square extensional mode with uniform displacement analogous to the radial breathing mode in disks.*

5.1 Theory and Background

Square resonators exhibit several notable vibrational bulk modes: shear modes such as the Lamé [124, 125, 126, 127] and face-shear modes [128], and a bulk extensional mode [129] depicted in Figure 5.1. The square extensional mode (Figure 5.1c) is analogous to the radial breathing mode in disks and has a resonance frequency strongly dependent upon its Young's modulus. In contrast, the Lamé and face shear modes support transverse acoustic waves rather than longitudinal, with its resonance frequency—in isotropic media—principally governed by the shear modulus rather than its Young's modulus [130, 131]:

$$f_{resonance} = \frac{\beta}{\lambda}\sqrt{\frac{C_{eq}}{\rho}} \tag{5.1}$$

where β is a geometric constant, λ is the acoustic wavelength, C_{eff} is the equivalent stiffness and ρ is the material density (mode-specific expressions are shown in Table 5.1).

Table 5.1: Parameters for resonance frequencies for various bulk modes depicted in Figure 5.1. C_{eq} expressions for both cubic materials [131] and hexagonal materials are listed.

Mode	β	λ	$C_{eq}^{(c)}$	$C_{eq}^{(h)}$
Lamé 0°	1	$\sqrt{2}L$	C_{44}	$\frac{1}{2}(C_{11} - C_{12})$
Lamé 45°	1	$\sqrt{2}L$	$\frac{1}{2}(C_{11} - C_{12})$	$\frac{1}{2}(C_{11} - C_{12})$
Face Shear (FS)	1.283	$2L$	C_{44}	$\frac{1}{2}(C_{11} - C_{12})$
Square-Extensional (SE)	1	$2L$	$C_{11} + C_{12} - \frac{2C_{12}^2}{C_{11}}$	$C_{11} + C_{12} - \frac{2C_{13}^2}{C_{33}}$

5.2 Design and Fabrication

The square resonator's Lamé mode is of principal interest owing to several properties: its four nodal points are located at the corners, where the structure can be conveniently clamped to counteract anchor loss. According to Equation (2.17), this zero strain ε gives it theoretically infinite Q_{TED} though material/structural defects and the introduction of tethers will practically limit Q_{TED}. Additionally, the Lamé mode confers conspicuous advantages as its pure shear-wave nature limits the number of phonon branches and available dissipation paths, suppressing its Akhiezer damping in the mode-dependent formulation [22].

Material-dependent, TED is exacerbated in SiC—nearly 5×greater than in Si—and demands proper engineering of the resonator to negate these effects. However, at every point within the plate, the in-plane strain components are equal and opposite and sum to zero, rendering the Lamé mode isochoric (constant-volume) with virtually no TED according to Equation (2.17). To wit, the Lamé mode resonator's simulated Q_{TED} remains robust despite defects and asperities (Figure 5.2) though in practice the addition of tethers will hinder Q_{TED}.

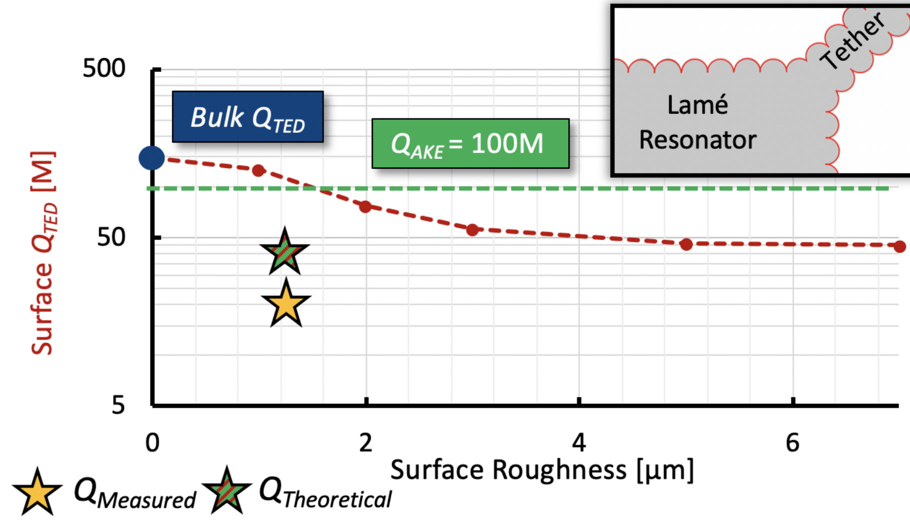

Figure 5.2. 65 µm-*thick Lamé mode resonators exhibit high bulk (blue) and surface (red)* Q_{TED} (148 × 10^6 *and* 50 × 10^6, *respectively). (inset, in red) Roughness is modeled as uniform sidewall asperities. In practice, the as-born roughness of the sidewall is chaotic and difficult to simulate. The quantum Akhiezer limit (green) is* ~100 × 10^6 *at* 6.27 MHz *for a* $Q_{Theoretical}$ *of* 45 × 10^6 *for an acoustically decoupled device.*

Critically, prerequisite to probing the Akhiezer limit one must carefully deliberate and consider the common limiting mechanisms plaguing micromechanical resonators: thermoelastic dissipation (TED), anchor losses (ANC), air squeeze-film damping (SFD), and surface loss. To that end, the square resonator operating in its bulk Lamé mode offers salient advantages, an excellent test vehicle for exploring fundamental dissipation limits.

The thick monocrystalline SiCOI substrate offers inherent advantages over amorphous or grown thin-film substrates. Amorphous materials are limited in thickness and rife with intrinsic material defects while interfacial defects that arise during growth processes threaten Q-factor [42]. Conversely, forming SiCOI substrates through fusion bonding of n-doped (~0.1 Ω · cm) monocrystalline 4H-SiC wafers (sourced from Cree®) largely circumvents these issues.

Other sources of dissipation such as squeeze-film damping and surface losses that

plague low-frequency flexural type resonators are largely avoided. The bulk wave nature of the Lamé mode and SiC's high stiffness (~3× higher than Si) relax vacuum requirements and mitigate air damping while rendering surface losses negligible [43].

Finally, anchor loss is a conspicuous source of dissipation as vibrational energy is lost from the resonator through the tethers to the substrate. Addressed in the following section, we implement a one dimensional (1D) phononic crystal tether to confine energy within the resonator itself.

5.2.1 Phononic Crystal Tethers

One may eliminate anchor loss by asymptotically narrowing the tethers until energy may not propagate to the substrate. Naturally, this significantly compromises structural integrity and can introduce unpredictable spurious mode interactions undermining both frequency measurement and capacitive transduction. However, wider tethers drastically deteriorate not only anchor loss, but the strain and displacement at the resonator and tether interface introduce significant amounts of TED. I.e. a perfect square SiC resonator without tethers possesses a Q_{TED} of 1×10^9, rather than 50×10^6–150×10^6 with tethers as in Figure 5.2.

In this work, the side-supported Lamé resonator requires only in-plane decoupling; we augment the tethers with square-shaped unit cells of critical dimension on the order of the quarter wavelength ($\lambda/4$) of the shear Lamé wave (Figure 5.3).. Several combinations of resonator orientations and unit cell periodicity were implemented; PML simulation of tethers with one (1100 µm long) and two (1900 µm long) unit cells grant $Q_{ANC} = 40 \times 10^6$ and 5×10^9, respectively. Given negligible anchor loss, the final device yields a $Q_{Total}^{-1} = (Q_{TED}^{-1} + Q_{AKE}^{-1})$ of approximately 45×10^6 (Figure 5.2).

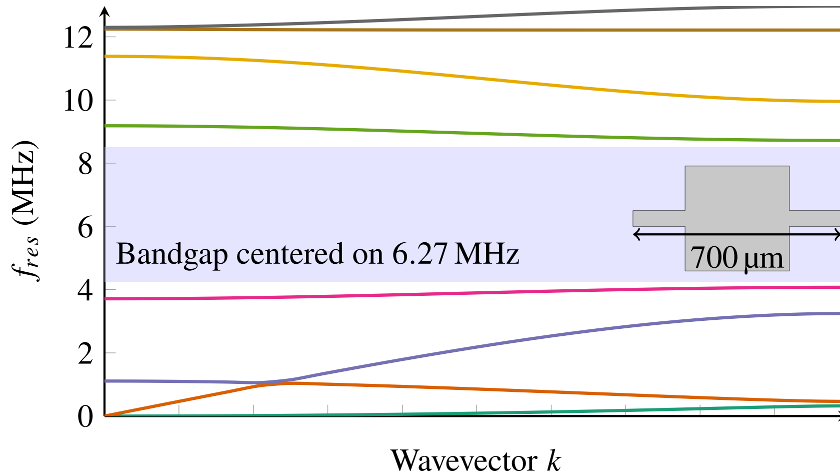

Figure 5.3. *Eigenfrequency simulation with Bloch-Floquet boundary conditions in a 1D PnC. Allowable eigenmodes surround a bandgap centered on* 6.27 MHz *in a* 700 µm *long unit cell (inset).*

Mitigating anchor loss provides a two-fold benefit: enabling high Q and suppressing any spurious modes due to the tether and surrounding substrate. Proper substrate decoupling design not only enables transduction via high Q but also instills confidence in frequency measurement by narrowing the resonance linewidth and suppressing spurious modes.

5.2.2 Process and Fabrication

SiCOI substrates with 65 µm n-type 4H-SiC device layer on a 380 µm Si handle layer separated by a thermally-grown silicon dioxide interlayer were custom-made in a process slightly modified from [63]. Critically, as the C-face of SiC oxidizes 10× faster than the Si face, care must be taken to match the concavities of the SiC and Si wafers to facilitate fusion bonding; any voids in the buried oxide layer compromise subsequent grinding. More specifically, when grinding the SiC layer below 100 µm, any non-idealities in bonding may lead to cracking and wafer failure.

Aluminum wire bonding directly to SiC forms a Schottky barrier, exhibiting diode-like

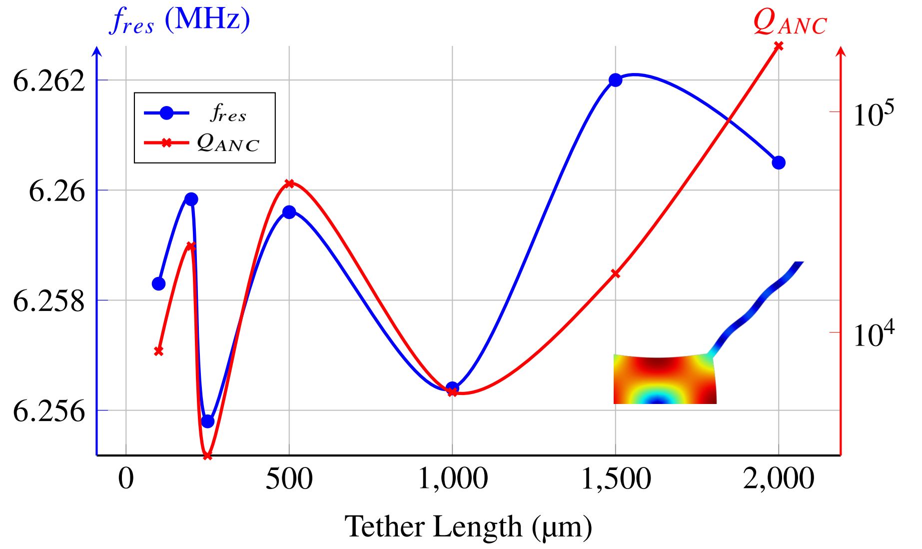

(a)

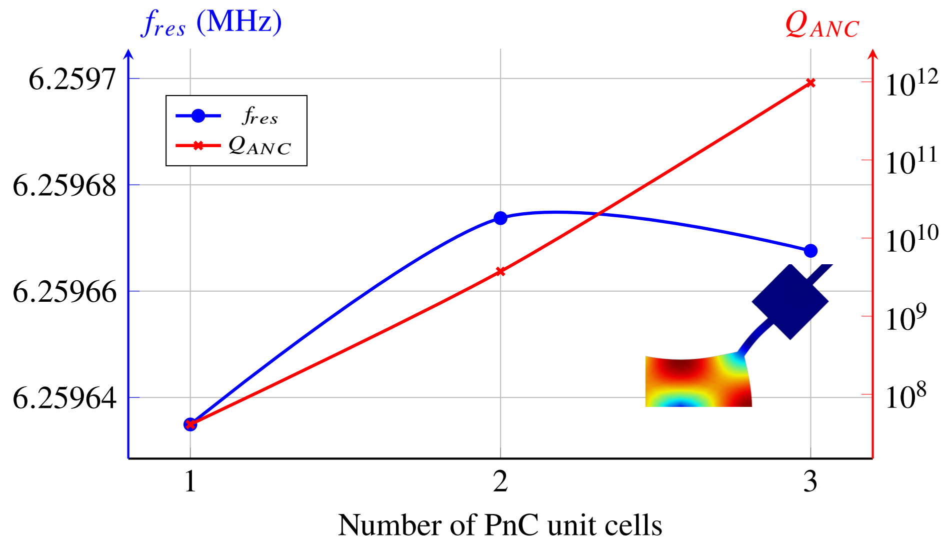

(b)

Figure 5.4. *(a) Perfectly matched layer eigenfrequency simulation of the Lamé mode with a plain tether (inset). The tether introduces spurious eigenmodes and waviness; consequently, varying tether length has a highly volatile effect on both f_{res} and Q_{ANC}. Further, absolute Q_{ANC} never exceeds 1×10^6. (b) The introduction of the PnC (inset) confers frequency robustness; the variation is on the order of* Hz *and can likely be attributed to meshing variation. Additionally, there is a clear positive monotonic relation between the number of unit of cells and Q_{ANC}. For comparison, the lengths of one, two and three unit cells are* 1100 μm, 1900 μm *and* 2700 μm, *respectively with Q_{ANC} exceeding 1×10^9 with two or more unit cells.*

behavior. Therefore, in order to electrostatically transduce the device, LPCVD n-type poly silicon is deposited and subsequently patterned to form thick SiC electrodes conferring ohmic contact to SiC [93, 132]. While certain metals–notably nickel (Ni)–also provide ohmic contact, polySi's high temperature robustness grants the SiCOI platform process compatibility.

High fidelity patterning and growth of the nickel mask for SiC DRIE follows LIGA protocol. Following deposition of a Cr/Au seed layer, the 900 μm × 900 μm square resonators are defined in a maskless aligner with 5 μm wide trenches. Electroplated Ni is then grown in a nickel sulfamate bath for minimal film stress. The etch step takes place in an STS AOE using a mixture of sulfur hexafluoride (SF_6), argon (Ar), and oxygen (O_2) with a large DC bias voltage (Figure 5.5).

Carbon atoms in the SiC react with SF_6, forming a metallofluorinated passivation layer ($Ni_xC_yF_z$). This passivation closes the trench and limits the achievable aspect ratio. Consequently, ex-situ passivation removal is necessary to sufficiently etch the device layer

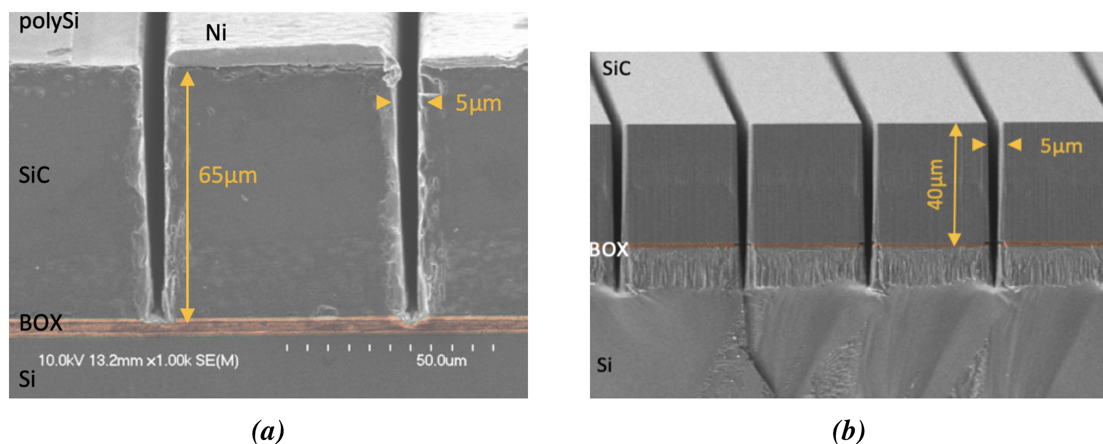

(a) *(b)*

Figure 5.5. *(top) An electroplated Ni mask is used for DRIE of* 5 μm-*wide smooth, vertical trenches in thick SiCOI substrates. Missing nickel on the left and SiC damage in the cleave plane are artifacts of the dicing process. (bottom) Without ex-situ passivation removal during etching, trenches are smooth with* 50 nm *surface roughness.*

and reach the BOX layer to allow for release. Use of Cr/Au as the seed layer is critical here as etch residue etchants lack selectivity to other commonly used seed layer metals such as Ti/Cu. The remaining nickel mask, seed layer and any remaining deposition on the sidewall are removed via diluted HNO_3 and Piranha solution.

The cavity is then defined via backside alignment to the SiC layer and etched by a standard through-wafer Bosch process in STS Pegasus. Attention to the cleanliness following this etch is essential as teflon–if not properly removed–will severely exacerbate anchor losses in the final device. To skirt complications of wafer bowing due to SiC and Si's thermal expansion disparity, the devices are then diced and thermally annealed at die level. This serves to consolidate the BOX layer and allow the LPCVD polysilicon to provide ohmic contact, and must be done in an inert gas setting to prevent polysilicon nitridation.

5.3 Results

The first capacitive monocrystalline SiC Lamé mode resonator with micron-scale transduction gaps were fabricated, capable of achieving $f \cdot Q$ exceeding 1.25×10^{14} Hz (Figure 5.6) along with its design parameters (Table 5.2).

The device is mounted on a PCB and interfaced with a trans-impedance amplifier (TIA) with feedthrough cancellation circuits to compensate for the relatively high motional resistance (>1 MΩ) of the device, owing to 5 μm wide transduction gaps. The resonator is configured with the drive and sense electrodes wire bonded 180° apart from one another to allow for optimal transduction (Figure 5.6b). The PCB is then placed in a vacuum chamber and pumped down to sub-mTorr pressures, though simulation shows the chamber requires

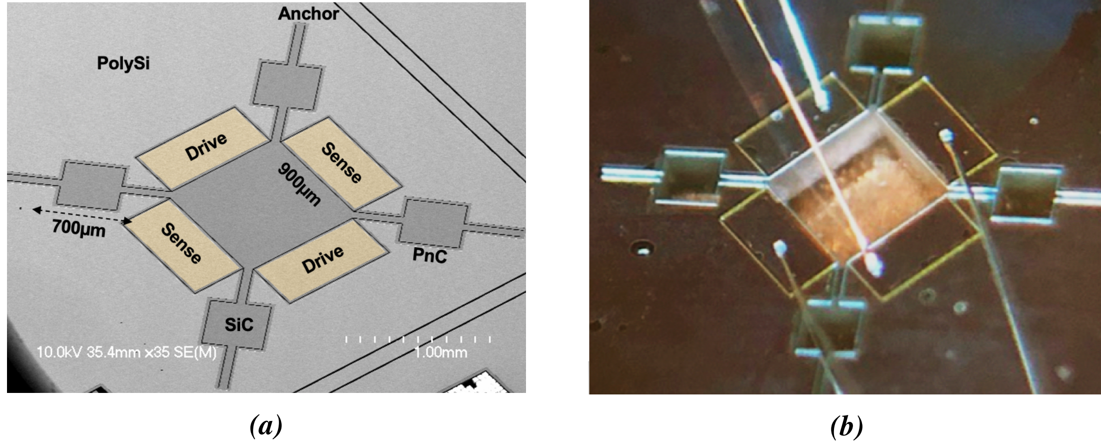

(a) *(b)*

Figure 5.6. *(a) SEM of an on-axis 4H-SiC Lamé mode resonator with phononic crystal (PnC) tether. A thin layer of LPCVD polysilicon (colored yellow) ensures ohmic contact between the wire bond and the electrodes. (b) Optical view of the transparent SiC square resonator above the Si cavity. The cavity facilitates release of the solid square resonator; the copper tape is visible below.*

Table 5.2: Device parameters and simulation for fully capacitive Lamé mode devices in thick 4H-SiCOI.

Parameter	Value	Unit
Silicon handle layer thickness	μm	380
Silicon carbide device layer thickness (h)	μm	65
Length of Lamé mode (L)	μm	900
Simulated frequency of 0° Lamé (f_0)	6.3	MHz
Tether width (t_w)	μm	60
PnC unit cell length (a)	μm	700
Gap size (g)	μm	5
Anchor/Support Loss (Q_{ANC})	1	5×10^9
Squeeze film damping sub-mTorr (Q_{SFD})	1	1×10^9
Bulk TED (Q_{TED})	1	100×10^6
Surface TED ($Q_{SurfTED}$)	1	45×10^6
Polarization Voltage (V_P)	V	15
Predicted motional resistance (R_m)	MΩ	1.7

Table 5.3: Comparison between Akhiezer-limited Lamé mode resonators in Si and this work in SiC.

Mat.	Freq.[MHz]	$Q[\times 10^6]$	$f \cdot Q[1 \times 10^{13}$ Hz]
Si [123]	20	1.44	2.88
Si [136]	6.89	3.24	2.23
Si [137]	4.13	5.34	2.20
SiC	6.27	20	12.50

no lower than 1 Torr to achieve Q_{SFD} greater than 1×10^9. Polarizing the resonator to 15 V, the Lamé mode is electrostatically driven with a V_{RMS}<100 mV with a motional resistance of 1.7 MΩ predicted by[1]:

$$R_m = \frac{1}{4} \frac{\sqrt{k_{eq} m_{eq}} g^4}{Q \varepsilon_o (hL)^2 V_P^2} \tag{5.2}$$

where the mode's effective stiffness is $k_{eq} = \pi^2 t G_{xy}$ and the square's effective mass is $m_{eq} = \frac{\rho t L^2}{2}$ [133, 134, 135].

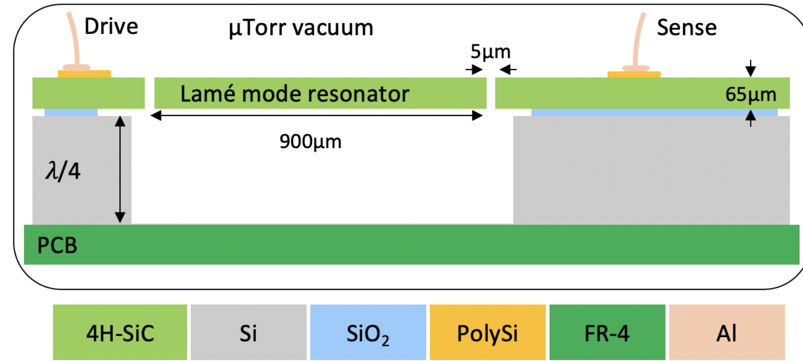

Figure 5.7. *Cross-sectional schematic of the electrostatic transduction of a SiC-on-Insulator Lamé mode resonator. The cavity below the resonator obviates surface tension effects during drying that potentially crack the tethers.*

The resonator displacement is placed on a PCB, wirebonded and placed in a vacuum chamber (Figure 5.7). The device is capacitively sensed and amplified via TIA with a feedback resistor of 100 kΩ and the S_{21} frequency response read out by a network ana-

[1]The factor 1/4 accounts for the use of two pairs of electrodes.

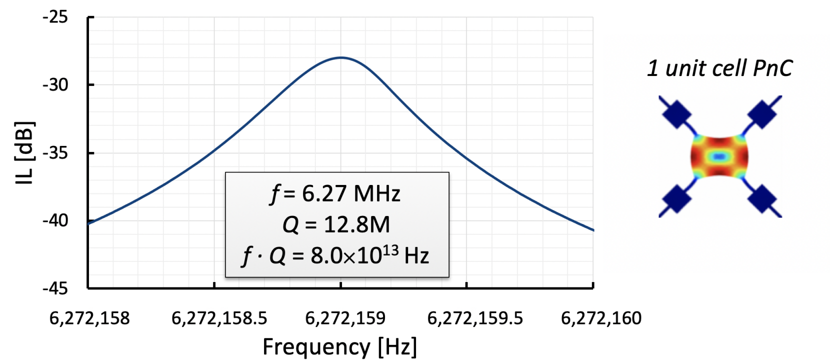

(a)

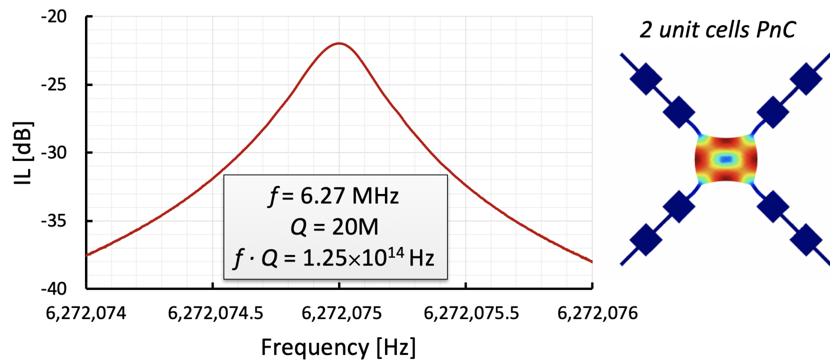

(b)

Figure 5.8. *(a) The fabricated square resonator with one PnC cell exhibits a maximum Q of* 12.8×10^6 *for an* $f \cdot Q = 8.0 \times 10^{13}$ Hz. *(b) A similar square resonator with two PnC unit cells showed a higher Q of* 20×10^6 *yielding an* $f \cdot Q = 1.25 \times 10^{14}$ Hz, *over 4×higher than Si's quantum Akhiezer limit.*

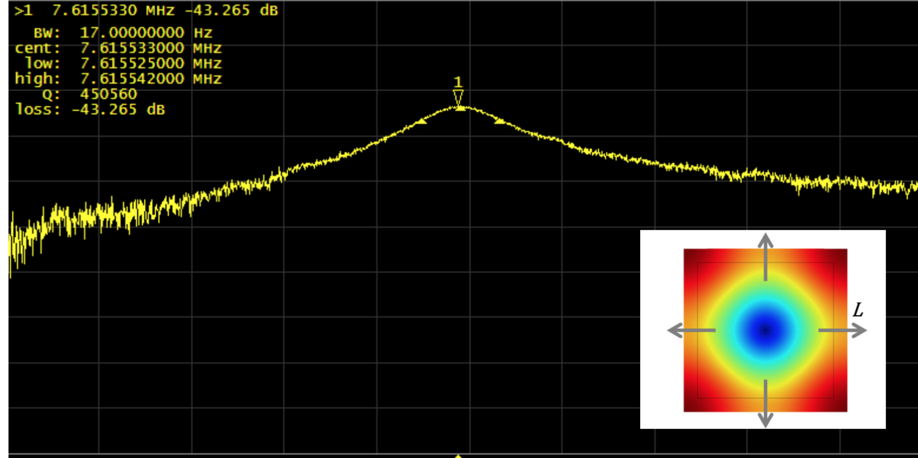

Figure 5.9. *Square extensional mode measured in the same devices show a Q of* 450×10^3 *at* 7.61 MHz*, agreeing with simulation. Strong displacement at the corner tether locations leaks energy readily (inset).*

lyzer (Figure 5.8). The square resonator with two PnC cells exhibits a Lamé mode with Q of 20×10^6 yielding an $f \cdot Q = 1.25 \times 10^{14}$ Hz at 6.27 MHz, over 4 × higher than Si's Akhiezer limit; the one PnC cell showed a maximum of 12.8×10^6 for an $f \cdot Q = 8.0 \times 10^{13}$ Hz at 6.27 MHz, nearly 3 × higher than Si. Using measured insertion loss, the back calculated values of motional resistance (R_m) and Q corroborate measurement well; i.e. a 65 µm-thick 6.27 MHz Lamé resonator with 5 µm-wide transduction gaps, and a Q of 20×10^6 should measure ~21 dB of insertion loss, compared to 23 dB from measurement. While 20×10^6 was the highest measured, devices of different orientation consistently showed Lamé modes in excess of 10×10^6, still exceeding Si's Akhiezer limits by a wide margin (Table 5.3). Other resonant BAW modes were measured such as the square-extensional mode at 7.6 MHz, though the 1D PnC tethers are not optimized for the mode's particular operational frequency, resulting in low measured $Q = 450 \times 10^3$ in accordance with COMSOL simulation (Figure 5.9).

At such high Qs, thermal stability affecting the frequency of the device becomes an

important consideration for proper measurement. As $Q \propto 1/BW$ (bandwidth), a slight shift in the frequency during measurement can alter the Q measurement. All care and consideration was taken to try to stabilize temperature before measurement to strive for the greatest accuracy. Ringdown measurements would do well to corroborate measurement, but the high Q, shifting peak, and capacitive feedthrough from the gaps among the device and handle layers render phase-based lock-in prohibitively difficult.

The temperature coefficient of frequency (TCF) of the Lamé mode was measured in an environmental chamber from −45 °C to 85 °C, exhibiting a TCF of $-12\,\text{ppm}/°\text{C}$ (Figure 5.10). In accordance with similar work in literature [138], this result is nearly 3× lower than that of Si's.

The record high $f \cdot Q = 1.25 \times 10^{14}\,\text{Hz}$ measured from electrostatically transduced SiC Lamé mode resonators reveal thick monocrystalline 4H-SiC-on-Insulator (SiCOI) substrates are well-positioned to explore new frontiers in MEMS instruments and sensors, well surpassing Si's intrinsic quantum limit. The Lamé mode resonators provide an ideal test vehicle for probing fundamental phonon-phonon dissipation limits and the low TCF of $-12\,\text{ppm}/°\text{C}$ offers insight into the SiCOI's suitability as a high performance, versatile platform for a myriad of sensors, instruments, filters and references.

In this work, Si is used as the SiCOI's handle layer to reduce development cost; replacing Si with SiC will render the SiCOI substrates amenable to temperatures exceeding 900 °C [139, 140]. Further, SiC's wide bandgap allows electronics to operate at temperatures far exceeding the limits of Si, opening doors for an all-SiC MEMS chip and electronics platform that can suitably address high-end emerging markets in demanding, extreme environments e.g. in underground drilling bits.

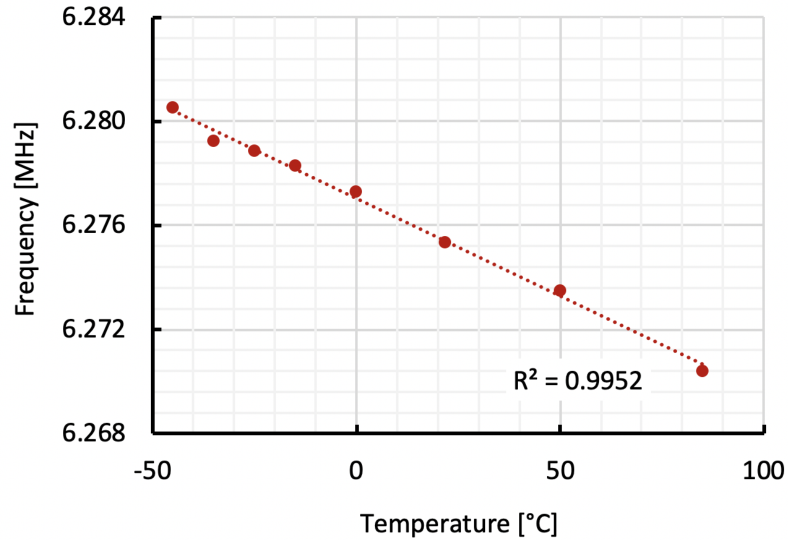

Figure 5.10. *TCF of 4H-SiC monocrystalline Lamé mode resonators is* $-12\,\text{ppm}/°\text{C}$ *with good linearity.*

5.4 4H-SiC Elasticity: FEA Simulation Vs. Reality

Throughout this work, finite element analysis via COMSOL® has been a critical tool in motivating and validating design. COMSOL can simulate both isotropic and anisotropic media and accepts arbitrary elasticity matrices. COMSOL has built-in values for (100) Si which are well vetted and investigated but lacks those for 4H-SiC, necessitating our own input. Early experimental work showed an incomplete picture of elasticity [141] or those for cubic-SiC [142]; significant effort using Density Functional Theory (DFT) spawned several publications though with widely varying results dependent upon computational costs and contemporary approximation accuracies [143, 144, 145]. Ultimately, we used the full elastic matrix measured in 1997 by Kamitani *et al.* via Brillouin scattering on 4H-SiC CREE wafers, the same used in the production of our SiCOI. The stiffness matrix is given

by Kamitani *et al.* with values given in GPa:

$$\begin{bmatrix} 507 \pm 6 & 108 \pm 8 & 52 \pm 9 & 0 & 0 & 0 \\ & 507 \pm 6 & 52 \pm 9 & 0 & 0 & 0 \\ & & 547 \pm 6 & 0 & 0 & 0 \\ & & & 159 \pm 7 & 0 & 0 \\ & & & & 159 \pm 7 & 0 \\ & & & & & 199.5 \pm 8.5 \end{bmatrix} \tag{5.3}$$

However, frequencies simulated—while proximate to measurement—never showed the same accuracy that devices measured and fabricated in silicon demonstrate (Table 5.4). Both optically and capacitively, all wineglass modes in disks showed a fairly systematic error ~ 2%; while this was accounted for in subsequent simulation and design by including a disk radius scaling factor, this is not a long term solution particularly for gyroscopic electrostatic simulation. Notably, the radial mode was simulated precisely with very minor errors and formed the cornerstone of our results in [70]. Intuitively, as the radial mode is radially isotropic, it has greater frequency dependence upon C_{11} (which has a proportionally smaller margin of error) rather than C_{66}.

The Lamé mode serendipitously presented a fantastic opportunity to clarify the elastic constants of 4H-SiC to provide the most accurate simulations possible—especially in our SiCOI frame work. The mode is an ideal vehicle for measuring elastic constants as it is determined uniquely by C_{66} with strong robustness to contributions from device thickness h, tether width t_w, polar cut misalignment β and other elastic constants. This is counter to elliptical modes, which have both axial and shear contributions to their frequencies which make fundamental assertions difficult. Our measurements coupled with (5.1) and Table 5.1 return a C_{66} of ~203.5 GPa considering fabrication variation and electrostatic softening.

Table 5.4: Measured and simulated frequencies of devices measured in this work. Simulated frequencies are performed in COMSOL with elasticity values from Kamitani et al.

Resonator	Mode Shape	Frequency f [MHz]		Error [%]
		Simulated	Measured	
Square (section 5.3): L = 900 µm (2 unit cell)	Lamé	6.176	6.272	1.5
	Sq-Ext	7.509	7.615	1.4
Disk (subsection 4.2.2): d = 2.21 mm	radial	3.58	3.56	0.56
	m = 3	4.06	4.17	2.6
	m = 4	5.28	5.37	1.6
	m = 5	6.41	6.54	2.0
	m = 6	7.54	7.73	2.5
Disk: d = 1.71 mm	radial	4.61	4.60	0.3
	m = 3	5.25	5.32	1.3
Disk (subsection 4.2.3): d = 1.64 mm	radial	4.86	4.86	0
	m = 2	3.58	3.61	0.8
	m = 3	5.47	5.53	1.1
	m = 4	7.11	7.18	1.3
	m = 5	8.64	8.73	1.0
Disk (subsection 4.2.2): d = 1.573 mm	radial	5.02	5.00	0.4
	m = 3	5.75	5.69	1.0
	m = 4	7.48	7.39	1.4
	m = 5	9.09	8.98	1.2
Disk (subsection 4.3.2): d = 1.44 mm	radial	5.48	5.53	0.72
	m = 3	6.233	6.29	1.0

Combining measured results from the capacitive disks in Chapter 4 and equations (B.11), (B.9) yields a revised set of elastic constants:

$$\begin{bmatrix} 517 & 110 & 52 & 0 & 0 & 0 \\ & 517 & 52 & 0 & 0 & 0 \\ & & 549 & 0 & 0 & 0 \\ & & & 159 & 0 & 0 \\ & & & & 159 & 0 \\ & & & & & 203.5 \end{bmatrix} \text{(GPa)}. \tag{5.4}$$

These elastic constants are in accordance with measured results for capacitive disks and square resonators, particularly for elliptical modes which have a stronger C_{66} dependence (Table 5.5). Notably in the new matrix, C_{11} is larger, in better agreement with more recent measurements of $E_{x,y}$ of 4H-SiC using the four-point bending method [147]. These elastic constants are by no means the final word; contributions to frequency from stress, deviations from the plate approximation and other factors unaccounted for may still exist. Namely, since our interest is primarily focused on in-plane modes such as the elliptical wineglass modes and Lamé modes, the elastic constants of interest are $C_{11},\ C_{66}$ and C_{12}; contributions from other components of C_{ij} are virtually negligible and the prior analysis largely ignores them in accordance with simulation. That said, given significant fabrication or operational/-electrostatic variations, they may play a larger role. As such, these constants provide a refinement of existing elastic constants within the framework of our SiCOI platform, its respective fabrication protocols and its application to in-plane bulk modes

Table 5.5: Simulated values of modes using new stiffness matrix (5.4)*. The values of* C_{11} *and* C_{66} *are chosen to match measurements of capacitive disks with diameter of* 1.44 mm *and in general simulate the elliptical modes with greater precision.*

Resonator	Mode Shape	Frequency f [MHz]		Error [%]
		Simulated	Measured	
Square (section 5.3): L = 900 µm (2 unit cell)	Lamé	6.269	6.272	0.05
	Sq-Ext	7.560	7.615	0.7
Disk (subsection 4.2.2): d = 2.21 mm	radial	3.58	3.56	0.56
	m = 3	4.11	4.17	1.5
	m = 4	5.33	5.37	0.75
	m = 5	6.48	6.54	0.92
	m = 6	7.59	7.73	1.8
Disk: d = 1.71 mm	radial	4.61	4.60	0.3
	m = 3	5.31	5.32	0.19
Disk (subsection 4.2.3): d = 1.64 mm	radial	4.86	4.86	0
	m = 2	3.61	3.61	0
	m = 3	5.53	5.53	0
	m = 4	7.18	7.18	0
	m = 5	8.72	8.73	0.1
Disk (subsection 4.2.2): d = 1.573 mm	radial	5.04	5.00	0.4
	m = 3	5.74	5.69	0.87
	m = 4	7.45	7.39	0.94
	m = 5	9.06	8.98	0.9
Disk (subsection 4.3.2): d = 1.44 mm	radial	5.53	5.53	<0.05
	m = 3	6.295	6.292	0.05

CHAPTER 6

CONCLUSION AND FUTURE WORK

4H-SiC is a rapidly maturing and increasingly appealing material for MEMS research and instrumentation. Production is increasing and foundries are shiftig toward six inch wafer production, pushing costs down making commercialization more attractive. While much has been covered in this thesis regarding the fabrication and development of resonators in thick single crystal 4H-SiC, there is far more to be unearthed; this chapter will discuss achievements made and explore future potential for 4H-SiC MEMs.

6.1 Exploring the Limits of Dissipation

This work has explored the origins of dissipation in 4H-SiC and methods to quash them in bulk acoustic wave resonators with heavy attention paid to thermoelastic dissipation and anchor loss. However, as Richard Feynman said, "There's plenty of room at the bottom." I.e. Microscopically, plenty of work remains in 4H-SiC to understand dissipation fundamentally and realize it experimentally. As of now, there has been little experimental verification of many structural and elastic properties of 4H-SiC. Brillouin scattering performed in 1997 by Kamitani *et al.* formed the basis of our simulation whereas recent work has used nano-indentation and strain gauge methods to measure effective moduli [147].

There has been however, a significant effort to study 4H-SiC computationally, with DFT (density functional theory) being the instrument of choice. Extracting structural and elastic constants especially with respect to temperature can allow us to probe the absolute

limits of dissipation. To wit, recalling (2.9), the fundamental phonon-phonon limit depends directly and indirectly through the specific heat and Grüneisen parameters on temperature. Meanwhile, TED is a strong function of the coefficient of thermal expansion ((2.17)), which is also a function of temperature. In fact, resonators measured at ~ 120 K—where $\alpha = 0$—showed the highest Q in silicon, free from thermoelastic dissipation [123]. DFT allows one to calculate a menagerie of material properties, providing motivation for further study and experiment (Figure 6.1). Simulations in silicon are relatively straightforward and efficient, with only two atoms in the primitive cell; however, computational effort scales approximately as N^{2-3} making computations involving 4H-SiC—which contains eight atoms in the primitive cell—far more taxing. Simple calculations have been performed such as the relaxed lattice parameter and the elastic constants at a single temperature, but to perform simulation akin to those in silicon requires careful investigation and optimization.

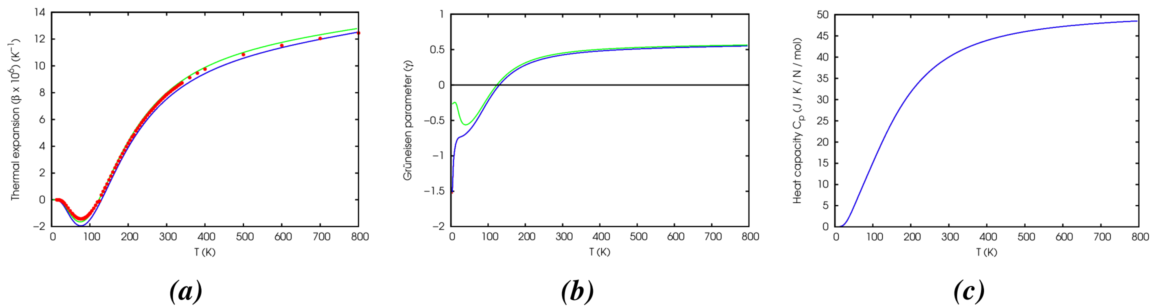

Figure 6.1. *(a) Calculated coefficient of thermal expansion of Si from* 0 K *to* 700 K *with a zero at* 120 K. *In theory, this would eliminate TED entirely. (b) The Grüneisen parameter also sees a zero near* 120 K *as one would expect. (c) The heat capacity of Si tending toward zero.*

Whereas Si does show $\alpha(T = 120\,\text{K}) = 0$, SiC does not for any of its polytypes [148, 149, 150]. Still, there is much to explore as temperature has a non-trivial effect on Q; recalling the expressions for Q_{AKE} and Q_{TED} (2.8) and (2.10), respectively, these parameters generally all possess dependence on temperature as well as doping [151] as described in Table 6.1.

Table 6.1: Overview of material parameters relevant to Q_{AKE} and Q_{TED} as a function of temperature at low temperature. A good reference for low temperature material properties can be found in [152, Ch. 2].

Param.	Unit	T-dependence	Remarks and References
α	ppm/K	$\alpha(T) \sim\propto T$	Contributes strongly to thermoelastic dissipation [148, 149, 150].
E	GPa	$\Delta E(T) \sim\propto -T \exp\{\frac{-1}{T}\}$	Young's modulus generally decreases with temperature [153, 154]. Note that the temperature coefficient of frequency (TCF) is related to α and the temperature coefficient of Young's modulus (TCE) as TCF $= \frac{1}{2}(\text{TCE} + \alpha)$.
c	J/(kg K)	$c_v(T) \sim\propto T^n$	Specific heat can depend on the doping concentration of the substrate as heat can be carried by either free charge carriers ($n = 1$) or lattice vibrations ($n = 3$). In solids, $c \approx c_v \approx c_p$.
k	W/(m K)	see above	Thermal conductivity can be related to the specific heat as $k = \frac{1}{3}cvl$ where v is the velocity and l is the mean free path of the heat carrier.

Table 6.1 merely depicts the tip of the iceberg and somewhat belies the highly complex nature of the behavior of solids in the quantum regime. That said, with proper understanding of the effect of temperature upon material properties, a deliberately engineered Lamé mode resonator can provide insight into the nature of silicon carbide and probe the ultimate limits of dissipation.

6.2 BAW Gyroscopes with High Aspect Ratio Capacitive Gaps

Inertial grade gyroscopes demand not only ultra-high Q factors, but mode-matched elliptical modes as well, with a couple avenues to achieving mode-matched operation.

One is narrow gap transduction via the HARPSS process [155] utilizing the electrostatic spring softening effect; the other is via frequency tuning by mass ablation or stiffness trimming [156]—a more promising solution given SiC's greater isotropy relative to silicon. HARPSS on SiC has been attempted but not fully demonstrated; CTE mismatches and other issues still remain but if successful, can offer incredibly low motional resistances and extremely high scale factors (see equations (1.17), (1.18)).

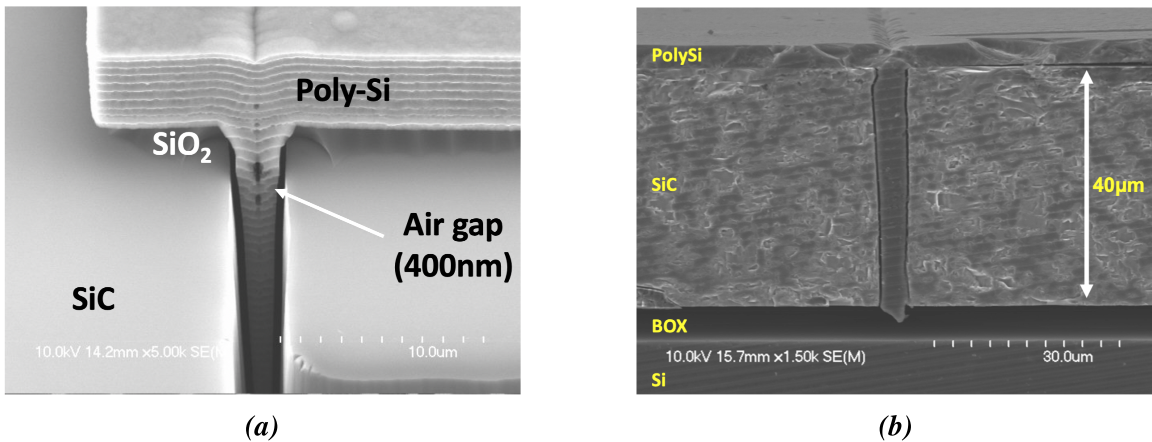

(a) *(b)*

Figure 6.2. *(a) SEM image of a prototyped HARPSS on SiC device. (b) Cross section in a* 40 μm *thick substrate with a* 440 nm *gap.*

However, a trade-off exists. Capacitive transduction in a resonant device demonstrates linear response between input to output signals until the vibration amplitude reaches 10% of its nominal gap size. This is ultimately detrimental to the minimum detectable input rotation-rate limited by brownian noise ((1.20) as well as the dynamic range ((1.19)). Therefore, to take full advantage of SiC's high quality factor, one would utilize wider gaps and implement trimming post-fabrication to enable performance comparable to modern ring-laser gyroscopes (Table 6.2).

Table 6.2: Comparison of proposed SiC gyro design utilizing laser trimming along with existing Si BAW gyros and state-of-the-art ring laser gyro [157].

Parameter	Unit	(1 0 0) Si	Epi-poly Si	SiC	RLG
Q-factor	1	100×10^3	1×10^6	20×10^6	
Gap size	nm	200–300	400–500	2000	N/A
Drive amplitude	nm	25	45	200	
Volume	cm^3	< 0.05	< 0.05	< 0.05	270
Power	mW		< 100 (projected)		> 400
ARW	$^\circ/\sqrt{h}$	0.06	0.01	0.00016	0.00023

6.3 Concluding Remarks

This work aimed to make strides in the development of thick single crystalline SiC resonant MEMS with a focus on achieving ultra-high quality factors. Resonators fabricated using optimized processing techniques exhibit state of the art quality factors with dissipation nearing their mechanical limits (Figure 6.3). With the theoretical framework established, continued research and investigation into SiC's material and dissipative properties along with development of its batch fabrication position monocrystalline SiC MEMS to make waves in the field of high performance sensors and instruments.

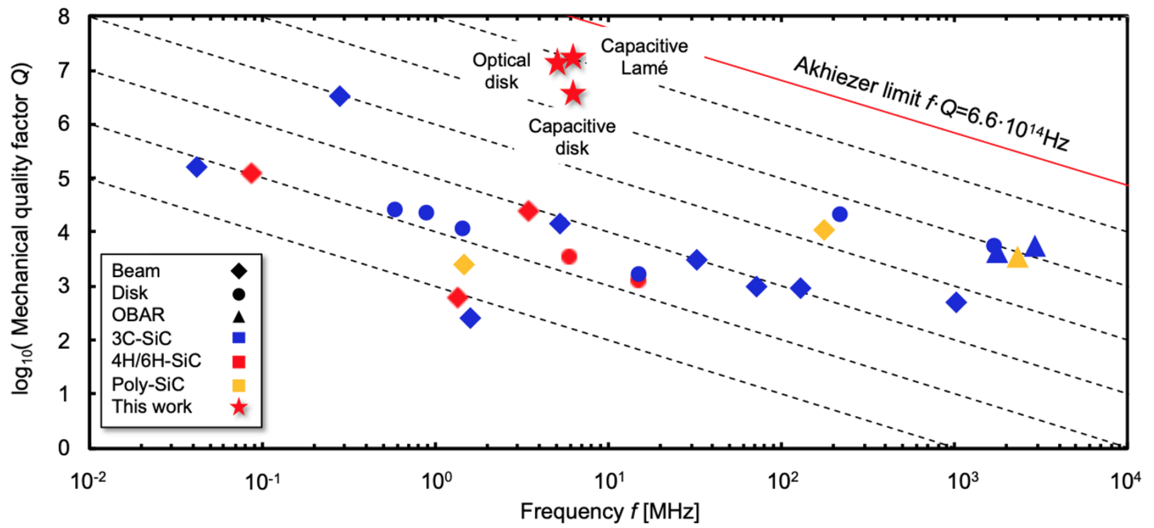

Figure 6.3. *Work presented in this dissertation show the highest mechanical $f \cdot Q$ in 4H-SiC and just under 10× below the fundamental phonon-phonon dissipation limits.*

Appendices

APPENDIX A

HOOKE'S LAW FOR ANISOTROPIC MEDIA

When discussing crystals and their orientations, it's helpful to define the Miller indices hkl for cubic crystals or Miller-Bravais indices $utvw$ for hexagonal crystals which define various crystal planes and directions (Table A.1). These indices differ whether referencing cubic or hexagonal Bravais lattices. It's important to recognize the correspondence between the Miller-Bravais crystallographic indices and natural Cartesian axes used when reporting values of anisotropic elasticity (Figure A.1a).

Table A.1: Miller index notation for cubic crystals [158] and Miller-Bravais index notation for hexagonal crystals where $u + v + t = 0$ *[159].*

Cubic	Hexagonal	Meaning
$[h\,k\,l]$	$[u\,v\,t\,w]$	Direction vector given by hkl or $uvtw$
$\langle h\,k\,l \rangle$	$\langle u\,v\,t\,w \rangle$	Family of symmetric direction vectors given by hkl or $uvtw$
$(h\,k\,l)$	$(u\,v\,t\,w)$	Crystal plane perpendicular to $[h\,k\,l]$ or $[u\,v\,t\,w]$
$\{h\,k\,l\}$	$\{u\,v\,t\,w\}$	Family of crystal planes perpendicular to $[h\,k\,l]$ or $[u\,v\,t\,w]$

The elastic constants are elements of the fourth-order stiffness tensor (C_{ijkl}, S_{ijkl}) relating anisotropic stress (σ) to strain (ε) and vice-versa; Voigt notation has been introduced throughout this work [160, 161].

$$
\begin{array}{ccccccccc}
ij & = & 11 & 22 & 33 & 23,32 & 13,31 & 12,21 \\
 & & \Updownarrow & \Updownarrow & \Updownarrow & \Updownarrow & \Updownarrow & \Updownarrow \\
\Downarrow & & xx & yy & zz & yz,zy & xz,zx & xy,yx \\
 & & \Downarrow & \Downarrow & \Downarrow & \Downarrow & \Downarrow & \Downarrow \\
\alpha & = & 1 & 2 & 3 & 4 & 5 & 6
\end{array}
$$

$$\sigma_{ij} = C_{ijkl}\varepsilon_{kl} \Leftrightarrow \begin{bmatrix}\sigma_1\\\sigma_2\\\sigma_3\\\sigma_4\\\sigma_5\\\sigma_6\end{bmatrix} = \begin{bmatrix}C_{11} & C_{12} & C_{13} & C_{14} & C_{15} & C_{16}\\C_{21} & C_{22} & C_{23} & C_{24} & C_{25} & C_{26}\\C_{31} & C_{32} & C_{33} & C_{34} & C_{35} & C_{36}\\C_{41} & C_{42} & C_{43} & C_{44} & C_{45} & C_{46}\\C_{51} & C_{52} & C_{53} & C_{54} & C_{55} & C_{56}\\C_{61} & C_{62} & C_{63} & C_{64} & C_{65} & C_{66}\end{bmatrix}\begin{bmatrix}\varepsilon_1\\\varepsilon_2\\\varepsilon_3\\\varepsilon_4\\\varepsilon_5\\\varepsilon_6\end{bmatrix} \tag{A.1}$$

$$\varepsilon_{ij} = S_{ijkl}\sigma_{kl} \Leftrightarrow \begin{bmatrix}\varepsilon_1\\\varepsilon_2\\\varepsilon_3\\\varepsilon_4\\\varepsilon_5\\\varepsilon_6\end{bmatrix} = \begin{bmatrix}S_{11} & S_{12} & S_{13} & S_{14} & S_{15} & S_{16}\\S_{21} & S_{22} & S_{23} & S_{24} & S_{25} & S_{26}\\S_{31} & S_{32} & S_{33} & S_{34} & S_{35} & S_{36}\\S_{41} & S_{42} & S_{43} & S_{44} & S_{45} & S_{46}\\S_{51} & S_{52} & S_{53} & S_{54} & S_{55} & S_{56}\\S_{61} & S_{62} & S_{63} & S_{64} & S_{65} & S_{66}\end{bmatrix}\begin{bmatrix}\sigma_1\\\sigma_2\\\sigma_3\\\sigma_4\\\sigma_5\\\sigma_6\end{bmatrix} \tag{A.2}$$

The symmetries of linear elasticity reduce C_{ijkl} to a *symmetric* second order tensor with

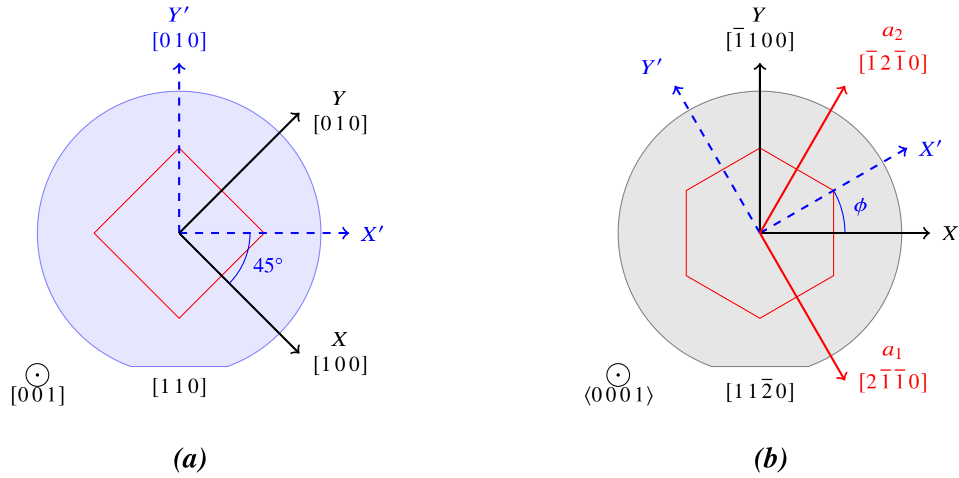

Figure A.1. *(a) A standard* (1 0 0) *silicon wafer with wafer flat aligned to the* [1 1 0] *direction. Rotated axes* ($X'Y'$) *show transformation from* [1 0 0] *to* [1 1 0] *alignment. (b) A standard* {0 0 0 1} *on-axis 4H-SiC wafer with wafer flat aligned to the* [1 1 2̄ 0] *direction. The red axes* $a_{1,2}$ *are lattice vectors that form the basis spanning crystal space. Natural Cartesian axes (black) aligned to reported crystallographic constants differ from as-manufactured flats, though for hexagonal SiC, this is largely irrelevant.*

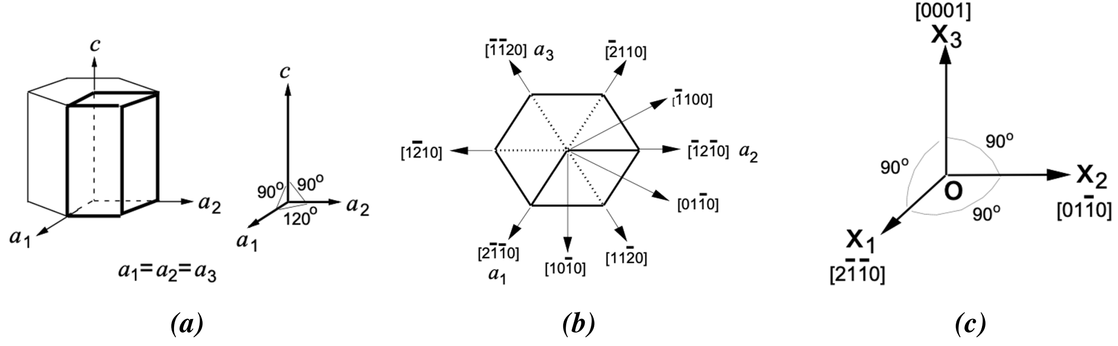

Figure A.2. *Hexagonal close packed crystallography. (a) The hexagonal unit cell depicting the c and $a_{1,2}$ vectors. (b) Directions with hexagonal Miller-bravais indices. The third index t is a dummy index to reinforce analogy with the cubic system i.e. the indices obey $u+v+t = 0$. (c) The link between Miller-Bravais index notation and standard orthogonal cartesian axes xyz. All elastic constant C values are reported with respect to this convention.*

21 independent elements for the most general anisotropic material:

$$C_{\alpha\beta} = \begin{bmatrix} C_{11} & C_{12} & C_{13} & C_{14} & C_{15} & C_{16} \\ & C_{22} & C_{23} & C_{24} & C_{25} & C_{26} \\ & & C_{33} & C_{34} & C_{35} & C_{36} \\ & & & C_{44} & C_{45} & C_{46} \\ & & & & C_{55} & C_{56} \\ & & & & & C_{66} \end{bmatrix} \quad \text{(A.3)}$$

An *orthotropic* material has three planes of symmetry and reduces the stiffness matrix to [160]:

$$C_{\alpha\beta} = \begin{bmatrix} C_{11} & C_{12} & C_{13} & 0 & 0 & 0 \\ & C_{22} & C_{23} & 0 & 0 & 0 \\ & & C_{33} & 0 & 0 & 0 \\ & & & C_{44} & 0 & 0 \\ & & & & C_{55} & 0 \\ & & & & & C_{66} \end{bmatrix} \quad \text{(A.4)}$$

The inverse of (A.4)—the compliance matrix—is commonly written in the form:

$$\begin{bmatrix} \varepsilon_1 \\ \varepsilon_2 \\ \varepsilon_3 \\ \varepsilon_4 \\ \varepsilon_5 \\ \varepsilon_6 \end{bmatrix} = \begin{bmatrix} \frac{1}{E_1} & \frac{-\nu_{21}}{E_2} & \frac{-\nu_{31}}{E_3} & 0 & 0 & 0 \\ \frac{-\nu_{12}}{E_1} & \frac{1}{E_2} & \frac{-\nu_{32}}{E_3} & 0 & 0 & 0 \\ \frac{-\nu_{13}}{E_1} & \frac{-\nu_{23}}{E_2} & \frac{1}{E_3} & 0 & 0 & 0 \\ & & & \frac{1}{G_{23}} & 0 & 0 \\ & & & & \frac{1}{G_{31}} & 0 \\ & & & & & \frac{1}{G_{12}} \end{bmatrix} \begin{bmatrix} \sigma_1 \\ \sigma_2 \\ \sigma_3 \\ \sigma_4 \\ \sigma_5 \\ \sigma_6 \end{bmatrix} \tag{A.5}$$

which is useful to relate the given elastic constants to "fundamental" elastic quantities such as the Young's Modulus (E_i), Poisson's ratio (ν_{ij}) and the shear modulus (G_{ij}).

Cubically symmetric materials such as (1 0 0) silicon or β-SiC possess four unique elements:

$$C_{\alpha\beta}^{(c)} = \begin{bmatrix} C_{11} & C_{12} & C_{12} & 0 & 0 & 0 \\ & C_{11} & C_{12} & 0 & 0 & 0 \\ & & C_{11} & 0 & 0 & 0 \\ & & & C_{44} & 0 & 0 \\ & & & & C_{44} & 0 \\ & & & & & C_{44} \end{bmatrix} \tag{A.6}$$

Similarly, hexagonally symmetric materials such as (4H, 6H)-SiC have five independent elements:

$$C_{\alpha\beta}^{(h)} = \begin{bmatrix} C_{11} & C_{12} & C_{13} & 0 & 0 & 0 \\ & C_{11} & C_{13} & 0 & 0 & 0 \\ & & C_{33} & 0 & 0 & 0 \\ & & & C_{44} & 0 & 0 \\ & & & & C_{44} & 0 \\ & & & & & \frac{C_{11}-C_{12}}{2} \end{bmatrix} \tag{A.7}$$

A.1 Universal Anisotropy Index

Zener initially introduced an anisotropy factor which can be considered the relation between the shear modulus for the material and its (isotropic) equivalent. This formulation

is suitable for cubic materials *only* [162]:

$$a_r = \frac{G}{E/[2(1+\nu)]} = \frac{2(1+\nu)G}{E} \equiv \frac{2C_{44}}{C_{11} - C_{12}} \tag{A.8}$$

A metric extending to all crystal symmetries was introduced called the universal anisotropy index [163]:

$$A^U = \frac{\kappa^V}{\kappa^R} + 5\frac{\mu^V}{\mu^R} - 6 \tag{A.9}$$

where $\kappa^{V,R}$ and $\mu^{V,R}$ are the bulk and shear moduli in the Voigt and Reuss approximations, respectively, calculated from the elastic constants for an orthotropic material [164]:

$$\begin{gathered} E^V = \frac{(A - B + 3C)(A + 2B)}{2A + 3B + C}, \quad \mu^V = \frac{A - B + 3C}{5}, \\ \kappa^V = \frac{A + 2B}{3}, \quad \nu^V = \frac{A + 4B - 2C}{4A + 6B + 2C} \end{gathered} \tag{A.10}$$

with

$$A = \frac{C_{11} + C_{22} + C_{33}}{3}, \quad B = \frac{C_{23} + C_{13} + C_{12}}{3}, \quad C = \frac{C_{44} + C_{55} + C_{66}}{3} \tag{A.11}$$

Similarly, the Reuss bounds are determined by:

$$\begin{gathered} E^R = \frac{5}{3A' + 2B' + C'}, \quad \mu^R = \frac{5}{4A' - 4B' + 3C'}, \\ \kappa^R = \frac{1}{3A' + 6B'}, \quad \nu^R = -\frac{2A' + 8B' - C'}{6A' + 4B' + 2C'} \end{gathered} \tag{A.12}$$

with

$$A' = \frac{S_{11} + S_{22} + S_{33}}{3}, \quad B' = \frac{S_{23} + S_{13} + S_{12}}{3}, \quad C' = \frac{S_{44} + S_{55} + S_{66}}{3} \tag{A.13}$$

Additionally, the various moduli are related through traditional engineering definitions:

$$\kappa^{V,R} = \frac{E^{V,R}}{3(1 - \nu^{V,R})}, \quad \mu^{V,R} = \frac{E^{V,R}}{2(1 + \nu^{V,R})} \tag{A.14}$$

A.2 Material Frame Rotation

As wafers are typically specified with a face $(h\ k\ l)$ and a flat $\langle h\ k\ l \rangle$, it's often necessary to rotate given elasticity matrices for use in FEA simulation. FEA software typically has this capability; alternatively, one may rotate the matrices themselves changing the basis with which to represent the elastic matrix [165].

Transforming/rotating the stiffness or compliance matrices (second order) from basis $\boldsymbol{e_1}, \boldsymbol{e_2}, \boldsymbol{e_3}$ to a second one $\boldsymbol{m_1}, \boldsymbol{m_2}, \boldsymbol{m_3}$ requires a transformation matrix $\Omega_{ij} = \boldsymbol{m} \cdot \boldsymbol{e}$:

$$\begin{bmatrix} \boldsymbol{m_1} \cdot \boldsymbol{e_1} & \boldsymbol{m_1} \cdot \boldsymbol{e_2} & \boldsymbol{m_1} \cdot \boldsymbol{e_3} \\ \boldsymbol{m_2} \cdot \boldsymbol{e_1} & \boldsymbol{m_2} \cdot \boldsymbol{e_2} & \boldsymbol{m_2} \cdot \boldsymbol{e_3} \\ \boldsymbol{m_3} \cdot \boldsymbol{e_1} & \boldsymbol{m_3} \cdot \boldsymbol{e_2} & \boldsymbol{m_3} \cdot \boldsymbol{e_3} \end{bmatrix} \tag{A.15}$$

Naturally, this matrix satisfies $\Omega^T \Omega = \Omega \Omega^2 = \boldsymbol{I}$. The stress, strain and elasticity matrices

then transform as:

$$\begin{aligned}
\sigma_{ij}^{(\boldsymbol{m})} &= \Omega_{ik}\sigma_{kl}^{(\boldsymbol{e})}\Omega_{jl} \\
\varepsilon_{ij}^{(\boldsymbol{m})} &= \Omega_{ik}\varepsilon_{kl}^{(\boldsymbol{e})}\Omega_{jl} \\
C_{ijkl}^{(\boldsymbol{m})} &= \Omega_{ip}\Omega_{jq}C_{pqrs}^{(\boldsymbol{e})}\Omega_{kr}\Omega_{ls}
\end{aligned} \tag{A.16}$$

The transformation can be more conveniently expressed as:

$$\boldsymbol{C}^{(\boldsymbol{m})} = \boldsymbol{K}\boldsymbol{C}^{(\boldsymbol{e})}\boldsymbol{K}^{T}, \quad \boldsymbol{S}^{(\boldsymbol{m})} = \boldsymbol{K}^{-T}\boldsymbol{S}^{(\boldsymbol{e})}\boldsymbol{K}^{-1} \tag{A.17}$$

$$\boldsymbol{K} = \begin{bmatrix} \boldsymbol{K}^{(1)} & 2\boldsymbol{K}^{(2)} \\ \boldsymbol{K}^{(3)} & \boldsymbol{K}^{(4)} \end{bmatrix}, \quad \boldsymbol{K}^{-T} = \begin{bmatrix} \boldsymbol{K}^{(1)} & \boldsymbol{K}^{(2)} \\ 2\boldsymbol{K}^{(3)} & \boldsymbol{K}^{(4)} \end{bmatrix} \tag{A.18}$$

$$\left.\begin{aligned}
\boldsymbol{K}_{ij}^{(1)} &= \Omega_{ij}^{2} \qquad \boldsymbol{K}_{ij}^{(2)} = \Omega_{i\ mod(j+1,3)}\Omega_{i\ mod(j+2,3)} \\
\boldsymbol{K}_{ij}^{(3)} &= \Omega_{mod(i+1,3)\ j}\Omega_{mod(i+2,3)\ j} \\
\boldsymbol{K}_{ij}^{(4)} &= \Omega_{mod(i+1,3)mod(j+1,3)}\Omega_{mod(i+2,3)mod(j+2,3)} \\
&\quad +\Omega_{mod(i+1,3)mod(j+2,3)}\Omega_{mod(i+2,3)mod(j+1,3)}
\end{aligned}\right\} i, j = 1 \ldots 3 \tag{A.19}$$

where mod is the modulo function. More directly, the matrices $\boldsymbol{R}$ for counter-clockwise

rotations around the x,y,z axes respectively are, with $c = \cos\theta$ and $s = \sin\theta$:

$$\boldsymbol{K}_x(\theta) = \begin{bmatrix} 1 & 0 & 0 & 0 & 0 & 0 \\ 0 & c^2 & s^2 & 2cs & 0 & 0 \\ 0 & s^2 & c^2 & -2cs & 0 & 0 \\ 0 & -cs & -cs & c^2 - s^2 & 0 & 0 \\ 0 & 0 & 0 & 0 & c & -s \\ 0 & 0 & 0 & 0 & s & c \end{bmatrix} \tag{A.20a}$$

$$\boldsymbol{K}_y(\theta) = \begin{bmatrix} c^2 & 0 & s^2 & 0 & 2cs & 0 \\ 0 & 1 & 0 & 0 & 0 & 0 \\ s^2 & 0 & c^2 & 0 & -2cs & 0 \\ 0 & 0 & 0 & c & 0 & -s \\ -cs & 0 & cs & 0 & c^2 - s^2 & 0 \\ 0 & 0 & 0 & s & 0 & c \end{bmatrix} \tag{A.20b}$$

$$\boldsymbol{K}_z(\theta) = \begin{bmatrix} c^2 & s^2 & 0 & 0 & 0 & 2cs \\ s^2 & c^2 & 0 & 0 & 0 & -2cs \\ 0 & 0 & 1 & 0 & 0 & 0 \\ 0 & 0 & 0 & c & s & 0 \\ 0 & 0 & 0 & s & c & 0 \\ -cs & cs & 0 & 0 & 0 & c^2 - s^2 \end{bmatrix} \tag{A.20c}$$

Transverse Isotropy Hexagonal materials possess something known as transverse isotropy, i.e. for 4H-SiC the stiffness matrix $\boldsymbol{C}$ is symmetric about the c-axis with material properties constant within this plane. Mathematically, this means that $\boldsymbol{C} = \boldsymbol{K}_z\boldsymbol{C}\boldsymbol{K}_z^T$; any rotation about the z-axis will return the same matrix. This can be observed by applying (A.20c) with arbitrary θ to any matrix that follows the form (A.7). Conversely, applying any rotation $\theta \neq n\pi/2$ to silicon yields a new stiffness matrix $\boldsymbol{C}$.

One can relate the stiffness matrix $\boldsymbol{C}$ to traditional engineering moduli by inverting it to

the compliance matrix $\boldsymbol{S}$:

$$\boldsymbol{S} = \frac{1}{\Delta}\begin{bmatrix} C_{11}C_{33} - C_{13}^2 & C_{13}^2 - C_{12}C_{33} & (C_{12} - C_{11})C_{13} & 0 & 0 & 0 \\ & C_{11}C_{33} - C_{13}^2 & (C_{12} - C_{11})C_{13} & 0 & 0 & 0 \\ & & C_{11}^2 - C_{12}^2 & 0 & 0 & 0 \\ & & & \frac{\Delta}{C_{44}} & 0 & 0 \\ & & & & \frac{\Delta}{C_{44}} & 0 \\ & & & & & \frac{2\Delta}{C_{11}-C_{12}} \end{bmatrix} \tag{A.21}$$

where $\Delta \coloneqq (C_{11} - C_{12})[(C_{11} + C_{12})C_{33} - 2C_{13}^2]$. In engineering parlance,

$$\boldsymbol{S} = \begin{bmatrix} \frac{1}{E_1} & \frac{-\nu_{21}}{E_1} & \frac{-\nu_{31}}{E_3} & 0 & 0 & 0 \\ \frac{-\nu_{12}}{E_1} & \frac{1}{E_1} & \frac{-\nu_{31}}{E_3} & 0 & 0 & 0 \\ \frac{-\nu_{13}}{E_1} & \frac{-\nu_{13}}{E_1} & \frac{1}{E_3} & 0 & 0 & 0 \\ & & & \frac{1}{G_{23}} & 0 & 0 \\ & & & & \frac{1}{G_{23}} & 0 \\ & & & & & \frac{2(1+\nu_{12})}{E_1} \end{bmatrix} \tag{A.22}$$

where $\Delta \coloneqq (C_{11}-C_{12})[(C_{11}+C_{12})C_{33}-2C_{13}^2]$. Applying transverse isotropic constraints to the general form of orthotropic compliance (A.5) and comparing it to (A.22), the following moduli for transversely (hexagonal) symmetric materials can be extracted:

$$E_z = C_{33} - 2C_{13}^2/(C_{11} + C_{12}) \tag{A.23a}$$

$$E_x = E_y = (C_{11} - C_{12})(C_{11}C_{33} + C_{12}C_{33} - 2C_{13}^2)/(C_{11}C_{33} - C_{13}^2) \tag{A.23b}$$

$$G_{xy} = (C_{11} - C_{12})/2 = C_{66} \tag{A.23c}$$

$$\nu_{zx} = C_{13}/(C_{11} + C_{12}) \tag{A.23d}$$

$$\nu_{xy} = (C_{11}C_{33} + C_{12}C_{33} - 2C_{13}^2)/(C_{11}C_{33} - C_{13}^2) - 1 \tag{A.23e}$$

where E is the Young's modulus, G_{xy} is the in-plane shear modulus and ν is Poisson's ratio.

Wafer Cut Misalignment Most expressions for moduli (A.23) in the wafer cut misaligned frame are cumbersome and are left for the reader to implement in software. However, out-of-plane axial stiffness and the average shear stiffness are more conveniently expressed in terms of compliances:

$$\frac{1}{E'_z(\beta)} = S'_{33} = S_{11}(\sin^4\beta) + S_{33}(\cos^4\beta) + (2S_{13} + S_{44})\cos^4\beta\sin^4\beta \tag{A.24a}$$

$$\begin{aligned}\frac{1}{G'_{(x,y)z}(\beta)} &= S'_G = (S'_{44} + S'_{55})/2 \\ &= S_{44} + (S_{11} - S_{12} - S_{44}/2)(\sin^2\beta) + 2(S_{11} + S_{33} - 2S_{13} - S_{44})(\cos^2\beta\sin^2\beta)\end{aligned} \tag{A.24b}$$

For cubic materials, in the direction $[h\,k\,l]$ [166]:

$$\frac{1}{E_{[h\,k\,l]}} = S_{11} - 2\left[(S_{11} - S_{12}) - \frac{1}{2}S_{44}\right](m^2n^2 + n^2p^2 + m^2p^2) \tag{A.25a}$$

$$\frac{1}{G_{[h\,k\,l]}} = S_{44} + 4\left[(S_{11} - S_{12}) - \frac{1}{2}S_{44}\right](m_1^2m_2^2 + n_1^2n_2^2 + p_1^2p_2^2) \tag{A.25b}$$

where $m,\ n,\ p$ are the direction cosines between $[h\,k\,l]$ and the natural $x,\ y,\ z$-axes ($\langle 1\,0\,0\rangle$ equivalent). In (A.25b), $m_{1,2},\ n_{1,2},\ p_{1,2}$ are the direction cosines for two orthogonal directions of interest of the shear modulus. For rotation β about a single axis e.g. x, this reduces

to:

$$\frac{1}{E'(\beta)} = S_{11} - 2\left[(S_{11} - S_{12}) - \frac{1}{2}S_{44}\right](\cos^2\beta\sin^2\beta) \tag{A.26a}$$

$$\frac{1}{G'(\beta)_{xy}} = S_{44} \tag{A.26b}$$

$$\frac{1}{G'(\beta)_{yz}} = S_{44} + 4\left[S_{11} - S_{12} - \frac{1}{2}S_{44}\right](2\cos^2\beta\sin^2\beta) \tag{A.26c}$$

Note that for cubic materials, the in-plane shear modulus is unchanged by polar cut misalignment.

APPENDIX B

BULK ELLIPTICAL MODAL ANALYSIS IN DISKS

The 2-D elastic theory governing in-plane vibrations in a disk can be described with the following wave equation [167]:

$$\frac{E}{1-\nu^2}\nabla(\nabla \cdot \boldsymbol{u}) - \frac{E}{2(1+\nu)}\nabla \times \nabla \times \boldsymbol{u} = \rho\frac{\partial^2 \boldsymbol{u}}{\partial t^2} \tag{B.1}$$

where E, ν and ρ denote the Young's modulus, Poisson's ratio and density of the resonator material, respectively. The displacement vector $\boldsymbol{u}$ may be defined in terms of the longitudinal pressure (P-wave) scalar potential Φ, and the shear wave (S-wave) vector potential $\boldsymbol{\Psi}$ via the Helmholtz theorem which says that any vector field can be decomposed into a curl-free scalar potential and a divergence-free vector potential:

$$\boldsymbol{u} = \nabla\Phi + \nabla \times \boldsymbol{\Psi} \tag{B.2}$$

Combining (B.2) with (B.1) and taking the curl and divergence, the elastic equations can be expressed as:

$$\frac{\partial^2 \Phi}{\partial t^2} = \alpha^2 \nabla^2 \Phi \tag{B.3a}$$

$$\frac{\partial^2 \Psi}{\partial t^2} = \beta^2 \nabla^2 \Psi \tag{B.3b}$$

in cylindrical coordinates: $\nabla^2 = \left(\frac{1}{r}\right)\left(\frac{\partial}{\partial r}\right) + \left(\frac{\partial^2}{\partial r^2}\right) + \left(\frac{1}{r^2}\right)\left(\frac{\partial}{\partial \theta}\right)$. $\alpha = \sqrt{E/\rho(1-\nu^2)}$ and

$\beta = \sqrt{E/2\rho(1+\nu)}$ are the propagation velocities of the P and S-waves, respectively.

With the assumption that the material is radially isotropic, the solutions to (B.3) involve trigonometric and Bessel functions of the first kind and take the form:

$$\Phi_m = A_m \; J_m(k_m r/R)\cos(m\theta)e^{i\omega_m t} \tag{B.4a}$$

$$\Psi_m = B_m \; J_m(h_m r/R)\sin(m\theta)e^{i\omega_m t} \tag{B.4b}$$

Here, m is assumed to be greater than or equal to two. $m = 0$ refers to the radial breathing mode which is independent of the azimuthal (tangential) direction, whereas the $m = 1$ mode involves nonzero deformation at the center, a translational mode [168]. A_m and B_m are elastic wave constants dimensionally equal to m^2. k_m and h_m are dimensionless frequency parameters relating the angular frequency ω_m, the radius R and the P and S wave speeds:

$$k_m = \omega_m R/\alpha \tag{B.5a}$$

$$h_m = \omega_m R/\beta \tag{B.5b}$$

Substituting (B.4) into (B.2) gives the radial and azimuthal components $\boldsymbol{u}$:

$$U_m = \left[A_m \frac{\mathrm{d}}{\mathrm{d}r}(J_m(k_m r/R)) + \frac{m}{r} B_m \; J_m(h_m r/R)\right]\cos m\theta \tag{B.6a}$$

$$V_m = \left[-B_m \frac{\mathrm{d}}{\mathrm{d}r}(J_m(h_m r/R)) - \frac{m}{r} A_m \; J_m(h_m r/R)\right]\sin m\theta \tag{B.6b}$$

The boundary conditions at $r = R$ for a disk with free circumference are given by the

following expressions for the axial radial stress σ_r and the shear azimuthal stress $\tau_{r\theta}$:

$$\sigma_r|_{r=R} = \frac{E}{1-\nu^2}\left[\frac{\partial U}{\partial r} + \frac{\nu}{r}\left(U + \frac{\partial V}{\partial \theta}\right)\right] = 0 \tag{B.7a}$$

$$\tau_{r\theta}|_{r=R} = \frac{E}{2(1+\nu})\left[\frac{\partial V}{\partial r} + \frac{1}{r}\left(\frac{\partial U}{\partial \theta} - V\right)\right] = 0 \tag{B.7b}$$

Combining (B.6) and (B.7) yields the following system of equations to solve for the coefficients A_m and B_m:

$$\begin{bmatrix} a_{11} & a_{12} \\ a_{21} & a_{22} \end{bmatrix} \cdot \begin{bmatrix} A_m \\ B_m \end{bmatrix} = 0 \tag{B.8}$$

as well as the eigenvalue equation for the disk mode shapes:

$$\left[\frac{k_m\ J_{m-1}(k_m)}{J_m(k_m)} - m - \frac{h_m^2}{2(m^2-1)}\right]\left[\frac{k_m\ J_{m-1}(h_m)}{J_m(h_m)} - m - \frac{h_m^2}{2(m^2-1)}\right] - m^2\left(\frac{h_m^2}{2(m^2-1)} - 1\right)^2 = 0 \tag{B.9}$$

From (B.8), the constants A_m and B_m are determined as the ratio of the P-wave and S-wave amplitudes ξ_m:

$$\begin{aligned}\xi_m &= \frac{B_m}{A_m} \\ &= \frac{J_m(k_m)}{J_m(h_m)} \frac{\frac{2k_m\ J_{m-1}(k_m)}{J_m(k_m)} + h_m^2 - 2m(m+1)}{\left(\frac{h_m\ J_{m-1}(h_m)}{J_m(h_m)} - (m+1)\right)2m}\end{aligned} \tag{B.10}$$

Defining $h_m = k_m\sqrt{2/(1-\nu)}$, the resonant frequencies can be calculated from (B.5a) and (B.9) and obey:

$$f_m = \frac{k_m}{2\pi R}\sqrt{\frac{E}{\rho(1-\nu^2)}} \tag{B.11}$$

with k_m for different modes and materials in Table B.1 solved for using Mathematica®.

Table B.1: Parameters to calculate in-plane elliptical wineglass mode frequencies using (B.11). k_m *depends upon the Poisson's ratio of the material which can be derived from the stiffness matrices via* (A.5) *for orthotropic and cubic materials and more directly via* (A.23e) *for hexagonal materials. The last two columns are in 4H-SiC.*

Parameter	Unit	$\langle 1\,0\,0 \rangle$ Si	$\langle 1\,1\,0 \rangle$ Si	Kamitani *et al.*	(C.2)
Density (ρ)	kg/m^3	2320	2320	3230	3230
In-plane Young's Modulus (E)	GPa	130	169	481	491
Poisson's ratio (ν)	1	0.278	0.064	0.205	0.204
$k_{m=2}$		1.41	1.60	1.48	1.48
$k_{m=0}$		2.04	1.89	1.99	1.99
$k_{m=3}$	1	2.16	2.44	2.26	2.26
$k_{m=4}$		2.81	3.15	2.94	2.94
$k_{m=5}$		3.42	3.82	3.57	3.57

The displacements in the radial and tangential directions u_r and u_θ, respectively, are related to the total displacements for two degenerate modes q_1 and q_2 via the following relationship:

$$\begin{bmatrix} u_r \\ u_\theta \end{bmatrix} = q_1(t) \begin{bmatrix} U_r \cos(m\theta) \\ U_\theta \sin(m\theta) \end{bmatrix} + q_2(t) \begin{bmatrix} -U_r \sin(m\theta) \\ U_\theta \cos(m\theta) \end{bmatrix} \tag{B.12}$$

Evidently, in accordance with Equation B.12, the degenerate modes are orthogonal with angular spacing $\theta_n = \pi/(2n)$, where n is the mode number and U_r, U_θ are the normalized mode shape functions in the radial and tangential directions.

B.1 Elliptical Mode Frequency Split in Disks

We first express the frequencies of the degenerate in-plane elliptical modes in terms of their effectives stiffnesses $K_{1,2}$ and their effectives masses $M_{1,2}$ [169]:

$$f_{1,2} = \frac{1}{2\pi}\sqrt{\frac{K_{1,2}}{M_{1,2}}} \tag{B.13}$$

Here, K_1 and K_2 are given with no loss of generality with respect to crystal symmetry:

$$K_{1,2} = K_0 \mp \frac{h\Delta_c}{32}\frac{\sin(4m\pi)}{m-2}\int_0^R \left[\frac{\mathrm{d}(U_r - U_\theta)}{\mathrm{d}r} + (m-1)\frac{U_r - U_\theta}{r}\right]^2 r\,\mathrm{d}r \tag{B.14a}$$

$$\begin{aligned} K_0 = \pi h \int_0^R \left(\frac{C_{11}^2 - C_{12}^2}{C_{11}} + \frac{\Delta_c}{4}\right)\left[\frac{\mathrm{d}U_r}{\mathrm{d}r}^2 + \left(\frac{U_r + mU_\theta}{r}\right)^2\right] r\,\mathrm{d}r \\ + 2\pi h \int_0^R \left(\frac{C_{11}C_{12} - C_{12}^2}{C_{11}} - \frac{\Delta_c}{4}\right)\left[(U_r + mU_\theta)\frac{\mathrm{d}U_r}{\mathrm{d}r}\right] r\,\mathrm{d}r \\ + \frac{\pi h}{4}\int_0^R (2C_{11} - 2C_{12} + \Delta_c)\left(\frac{\mathrm{d}U_\theta}{\mathrm{d}r} - \frac{mU_r + U_\theta}{r}\right)^2 r\,\mathrm{d}r \end{aligned} \tag{B.14b}$$

where $\Delta_c = C_{12} - C_{11} + 2C_{66}$. **Notably**—for hexagonal matrices where $C_{66} = (C_{11} - C_{12})/2$—$\Delta_c$ is zero and consequently, the second term of (B.14a) is zero, rendering total degeneracy. Conversely, for single crystal silicon where this relationship doesn't hold, the term $\sin(4m\pi)/(m-2)$ is zero for all $m \neq 2$ following:

$$\lim_{m\to 2}\frac{\sin(4m\pi)}{4(m-2)} = \pi \tag{B.15}$$

Caveat: Equations (B.14a) and (B.15) would suggest that all modes $m \neq 2$ show intrinsic degeneracy; unfortunately, this belies the real story. Recall that the disk modal analysis of this

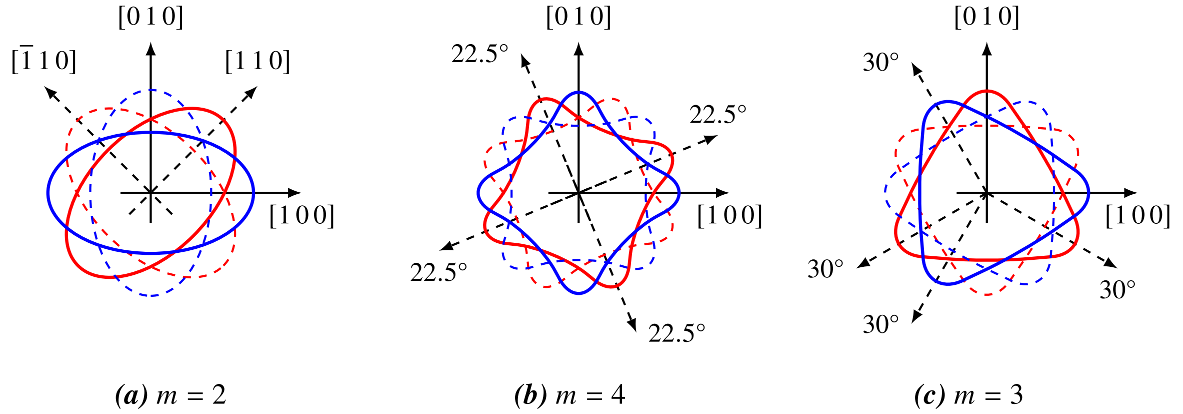

(a) $m = 2$ ***(b)*** $m = 4$ ***(c)*** $m = 3$

Figure B.1. *In these figures, the two orthogonal modes are in red and blue and their phase opposites are in the same color with dashed lines. (a,b) Even-ordered wineglass modes. For* $m = 2$*, the blue mode has anti-nodes aligned with* $\langle 1\,0\,0 \rangle$ *directions, while its orthogonal mode (red) has anti-nodes in the* $\langle 1\,1\,0 \rangle$ *directions. These directions have inequivalent stiffnesses according to* (A.25)*, breaking the degeneracy. For* $m = 4$*, the mode (blue) has anti-nodes along* $\langle 1\,0\,0 \rangle$ *and* $\langle 1\,1\,0 \rangle$ *directions while its orthogonal mode (red) has anti-nodes offset by* $\pi/(2m) = 22.5°$*, inducing frequency split. (c) Compare this to the* $m = 3$ *wineglass modes, where the two degenerate modes' anti-nodes are congruent with each other though offset by* 30°*. For example, the blue mode's anti-nodes at* 0°*,* 120° *and* 240° *are aligned to* 0°*,* 30° *and* 30° *equivalent crystal directions (given cubic crystal symmetry, i.e. modulo(*θ*,* 90°*)); the red orthogonal mode's anti-nodes at* 90°*,* 210° *and* 330° *are similarly aligned to* 0°*,* 30° *and* 30° *equivalent crystal directions. This analysis can be continued for higher odd-numbered modes, so despite material anisotropy, odd-numbered modes are inherently degenerate while even-numbered modes are not.*

section assumes that all modes are *exactly* periodically symmetric. This assumption holds for isotropic materials such as (1 1 1) Si and transversely isotropic materials such as 4H-SiC but isn't strictly correct for (1 0 0) or (1 1 0) Si where the in-plane stiffness variation non-uniform anti-nodal displacements [170, 171]. Therefore, for cubically symmetric materials like silicon, a general rule of thumb is that odd-numbered elliptical modes are inherently mode-matched while even-numbered elliptical modes exhibit frequency split (Figure B.1). Note that hexagonal materials are *immune* to this effect and exhibit total degeneracy for ***all*** elliptical modes.

APPENDIX C

MATERIAL PARAMETERS USED FOR SIMULATION

Table C.1: Relevant bulk material parameters used in FEA simulation. Stiffness matrices follow in section C.1.

Parameter	Unit	4H-SiC	SCS	polySi	SiO_2
Structural					
Density (ρ)	kg/m^3	3230	2320	2320	2200
Isotropic Young's Modulus (E)	GPa	-	-	130	70
Poisson's ratio (ν)	1	-	-	0.28	0.17
Thermal					
Conductivity (k)	W/(m K)	370	130	130	1.4
Coeff. of expansion (α)	ppm/K	4.2	2.6	2.6	0.5
Specific Heat (c_v)	J/(kg K)	690	690	690	730
Electrical					
Relative Permittivity (ε_r)	1	10	12	12	4.2

C.1 Stiffness Matrices used in Simulation

4H-SiC Elasticity matrix used for simulation and design of 4H-SiC devices at 298 K from Kamitani *et al.*:

$$\begin{bmatrix} 507 \pm 6 & 108 & 52 & 0 & 0 & 0 \\ & 507 \pm 6 & 52 & 0 & 0 & 0 \\ & & 547 \pm 6 & 0 & 0 & 0 \\ & & & 159 \pm 7 & 0 & 0 \\ & & & & 159 \pm 7 & 0 \\ & & & & & 199.5 \pm 8.5 \end{bmatrix} (\text{GPa}). \tag{C.1}$$

Motivated by measurement of Lamé mode resonators, some refinement introduces new constants:

$$\begin{bmatrix} 517 & 110 & 52 & 0 & 0 & 0 \\ & 517 & 52 & 0 & 0 & 0 \\ & & 549 & 0 & 0 & 0 \\ & & & 159 & 0 & 0 \\ & & & & 159 & 0 \\ & & & & & 203.5 \end{bmatrix} (\text{GPa}). \tag{C.2}$$

3C-SiC From Li *et al.*:

$$\begin{bmatrix} 352.3 & 140.4 & 140.4 & 0 & 0 & 0 \\ & 352.3 & 140.4 & 0 & 0 & 0 \\ & & 352.3 & 0 & 0 & 0 \\ & & & 232.9 & 0 & 0 \\ & & & & 232.9 & 0 \\ & & & & & 232.9 \end{bmatrix} (\text{GPa}). \tag{C.3}$$

Single Crystal Silicon The fundamental elasticity matrix reported for $(1\,0\,0)$ silicon with natural axes oriented along $\langle 1\,0\,0 \rangle$ Hopcroft *et al.*:

$$\boldsymbol{C}_{<100>\ \mathrm{Si}} = \begin{bmatrix} 165.7 & 63.9 & 63.9 & 0 & 0 & 0 \\ & 165.7 & 63.9 & 0 & 0 & 0 \\ & & 165.7 & 0 & 0 & 0 \\ & & & 79.6 & 0 & 0 \\ & & & & 79.6 & 0 \\ & & & & & 79.6 \end{bmatrix} (\text{GPa}). \tag{C.4}$$

Applying (A.16) with a 45° rotation around the z-axis to (C.4), one obtains in accordance

with [158]:

$$\boldsymbol{C}_{<110>\ \mathrm{Si}} = \begin{bmatrix} 194.4 & 35.2 & 63.9 & 0 & 0 & 0 \\ & 194.4 & 63.9 & 0 & 0 & 0 \\ & & 165.7 & 0 & 0 & 0 \\ & & & 79.6 & 0 & 0 \\ & & & & 79.6 & 0 \\ & & & & & 50.9 \end{bmatrix} (\mathrm{GPa}). \tag{C.5}$$

This is the frame of reference of a standard (1 0 0) silicon wafer with flat parallel to [1 0 0], and should be the matrix used for FEA simulation if rotation about the z-axis isn't implemented in software itself.

Any orientation is possible by composing three elementary rotations; in this case, we COMSOL multiphysics' convention of sequentially rotating about the zxz-axes with Euler angles α, β and γ to derive the stiffness matrix for (1 1 1) Si (Figure C.1).

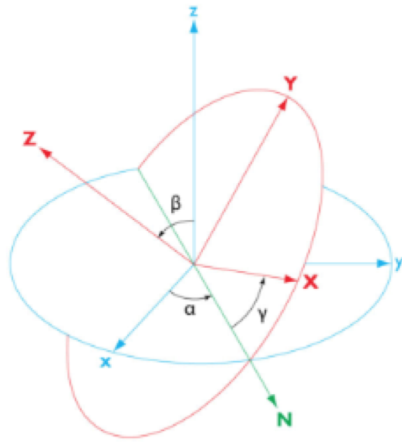

$$\boldsymbol{K} = \boldsymbol{K}_z(90°)\boldsymbol{K}_x(54.73°)\boldsymbol{K}_z(45°)$$

$$\begin{bmatrix} \frac{1}{6} & \frac{1}{6} & \frac{2}{3} & \frac{2}{3} & \frac{2}{3} & \frac{-1}{3} \\ \frac{1}{2} & \frac{1}{2} & 0 & 0 & 0 & 1 \\ \frac{1}{3} & \frac{1}{3} & \frac{1}{3} & \frac{-2}{3} & \frac{-2}{3} & \frac{-2}{3} \\ \frac{1}{\sqrt{6}} & \frac{-1}{\sqrt{6}} & 0 & \frac{-1}{\sqrt{6}} & \frac{1}{\sqrt{6}} & 0 \\ \frac{1}{3\sqrt{2}} & \frac{1}{3\sqrt{2}} & \frac{-\sqrt{2}}{3} & \frac{1}{3\sqrt{2}} & \frac{1}{3\sqrt{2}} & \frac{-\sqrt{2}}{3} \\ \frac{1}{2\sqrt{3}} & \frac{-1}{2\sqrt{3}} & 0 & \frac{1}{\sqrt{3}} & \frac{-1}{\sqrt{3}} & 0 \end{bmatrix} \tag{C.6}$$

Figure C.1. *Coordinate transformation using sequential Euler angle rotations α about the z-axis, β about the x-axis and γ about the z-axis. The 6×6 rotation matrix $\boldsymbol{K}$ is shown to the right.*

Applying 90°, 54.73° and 45° rotations[1] about the z, x, z axes, we use (C.4) and (C.6)

[1]54.73° results from the dot product of the two vectors ⟨1 0 0⟩ and ⟨1 1 1⟩: $\mathbf{a} \cdot \mathbf{b} = |a||b| \cos\theta$.

with (A.17) to yield the stiffness matrix for (1 1 1) face single crystal silicon:

$$\boldsymbol{C}_{(1\,1\,1)\ \mathrm{Si}} = \begin{bmatrix} 194.4 & 54.3 & 44.8 & 0 & -13.5 & 0 \\ & 194.4 & 44.8 & 0 & 13.5 & 0 \\ & & 204.0 & 0 & 0 & 0 \\ & & & 60.5 & 0 & 13.5 \\ & & & & 60.5 & 0 \\ & & & & & 70.3 \end{bmatrix} (\mathrm{GPa}). \qquad \text{(C.7)}$$

APPENDIX D

PROCESS PARAMETERS

Wet Chemistry When anisotropy is of no concern, wet etching is a straightforward and highly effective means of material removal and cleaning in general. Table D.1 reviews wet chemistries used throughout this thesis and their intended uses and compatibilities.

Table D.1: Wet etch chemistries and their material compatibilities. ✓, ✗ and ✓, ✗ denote strong and weak compatibilities and incompatibilities, respectively. SiC is virtually totally inert to all of these chemistries.

		Compatibility								
Etchant	Target	Ti	Cu	Cr	Au	Ni	Si	PR	Ox	Remarks
Piranha	Ti, Cu, Ni, Organics	-	-	✓	✓	-	✓	✓	✗	3:1 H_2SO_4 : H_2O_2
Aqua Regia	Noble Metals	✗	✗	✓	-	✗	✓	✗	✓	3:1 HCl : HNO_3
Acetic Acid	Cu	✓	-	✓	✓	✓	✓	✓	✓	5:1:1 H_2O : H_2O_2 : CH_3COOH
HNA	Si	✗	✗	✗	✓	✗	-	✓	✗	HF : HNO_3
HF/BOE	Ti, Al, Oxides, Nitrides	-	✓	✓	✓	✓	✓	✓	-	Oxide etch rate 1 µm/min to 3 µm/min
1020AC	Cr	✓	✗	-	✓	✗	✓	✓	✓	Cr etchant
EKC265™	Etch residue	✗	✗	✓	✓	✗	✓	✗	✓	Typically used after DRIE of silicon at 80 °C.
EKC162™	Etch residue	✗	✗	✓	✓	✓	✗	✗	✓	Used for ex-situ passivation cleaning during SiC etch.

Wet Oxidation Wet Oxidation steps for bonding were performed in a Tystar® Mini Tube with heated water bubbler to introduce steam, allowing for long oxidations > 30 h. For silicon, rates follow the Grove and Deal model for diffusion-limited oxidation. For silicon carbide, rates were extrapolated from Kumar *et al.*

Polysilicon Deposition Polysilicon deposition was performed in a low pressure Tystar® deposition furnace at 588 °C and 300 mTorr with 100 sccm SiH_4 and 7 sccm PH_3.

Polysilicon Etching Following deposition, polysilicon etch-back was performed in STS HRM ICP tool with the turbo pump valve manually set to 90% open, 13.56 MHz coil power of 2000 W, 13.56 MHz platen power of 30 W and SF_6 flow of 260 sccm. Etch rate is approximately 25 s/µm [173].

Seed Layer Metallization Cu was deposited either via evaporation in a chamber at room temperature and 2×10^{-6} Torr with deposition rate of 2 Å/s or sputtered at chamber pressure 30 mTorr and room temperature; 0.2 A for a deposition rate of 2 Å/s. Ti was deposited in a similar fashion though sputtered at 0.3 A for a deposition rate of 0.8 Å/s. Cr and Au were evaporated in the same conditions and with the same parameters. Etching metals used either dry etch Ar milling in an RIE tool: 250 W, 50 sccm Ar, 20 mTorr or wet etched according to Table D.1.

Photolithography Most lithography was executed in a Heidelberg Maskless Aligner 150. The laser was periodically calibrated by Heidelberg engineers and maintained by staff at Georgia Tech's Institute for Electronics and Nanotechnology. The center of the laser's

Table D.2: Photoresist conditions. In general, dose and softbake time scale linearly with thickness whereas thickness is proportional to the inverse square root of speed. AZ P4620 was used for general thick resist use. AZ 9260 high resolution resist was used for nickel electroplating. SC1827 was used for poly patterning and oxide etching. Softbakes conducted at 110 °C, 110 °C *and* 120 °C *for AZ P4620, AZ 9260 and SC1827, respectively.*

PR	Development	Speed [rpm]	Thickness [μm]	Softbake [min]	Dose [mJ/cm^2]
AZ P4620	2:1 MF-351 or 3:1 AZ400K	3000	7.5	2.5	700
		2500	8.5	3	800
		2000	13	4	1000
AZ9260	5 min DI soak, 3:1 AZ400K	2500	8.5	4	500
		2000	10	5	600
		1500	13	6	700
SC1827	MF-319	1500	5.4	3	500

Gaussian profile was also monitored and set to be close to the substrate surface with perpendicular incidence. AZ9260 was soaked in DI water for 5 min for film water sorption prior to development [174, 175].

Silicon Handle Layer Through-Etch Backside etching of the handle layer was performed in an STS Pegasus using the Bosch process and a low frequency (380 kHz) platen with the following parameters [173]:

Table D.3: Parameters for etching vias in the silicon handle layer in an STS Pegasus ICP tool. → indicates the parameter is ramped over the duration of the etch.

Parameter	Value	
	Etch	Passivation
Cycle time [s]	3.8	2
Pressure [mTorr]	30 → 25	15
C_4F_8 [sccm]	0	150
SF_6 [sccm]	250 → 300	0
O_2 [sccm]	10 → 12	0
Coil [W]	2200	1900
Platen [W]	80 → 95	0
Platen Temperature [°C]	−10 °C	−10 °C

APPENDIX E

DENSITY FUNCTIONAL THEORY IN QUANTUM ESPRESSO

In principle, the quantum mechanical wavefunction contains all the information of the system. However, with few exceptions, there are no analytical solutions to the Schrödinger equation which provides the allowed energy levels of the system. It's virtually impossible to calculate the N-body quantum-mechanical system largely due to the interaction potential between electrons, forcing evaluation of a system with $3N$ degrees of freedom rather than many single particle equations:

$$\hat{H}\Psi = \left[\hat{T} + \hat{V} + \hat{U}\right]\Psi = \left[\sum_{i}^{N}\left(\frac{-\hbar^2}{2m_i}\nabla_i^2\right) + \sum_{i}^{N} V(\boldsymbol{r}_i) + \sum_{i<j}^{N} U(\boldsymbol{r}_i, \boldsymbol{r}_j)\right]\Psi = E\Psi \qquad \text{(E.1)}$$

where $\hat{H}$ is the Hamiltonian composed of $\hat{T}$, $\hat{V}$ and $\hat{U}$ which are the kinetic energy, the external potential due to static positively-charged nuclei (Born-Oppenheimer approximation) and the interaction potential, respectively. The last term is the exchange-correlation potential and captures the effects of the Coulombic interactions between electrons and is the root of the computational difficulties in calculating wavefunctions.

Numerous approaches have been forged but the most successful by far—Density functional theory (DFT)—undercuts this problem by proving that the electron density uniquely determines the wavefunction:

$$\Psi(\boldsymbol{r}_1, \boldsymbol{r}_2, \ldots, \boldsymbol{r}_N) \Rightarrow \Psi[n] \qquad \text{(E.2)}$$

The Hamiltonian can then be reframed with an effective single-particle potential:

$$V_s(\boldsymbol{r}) = V(\boldsymbol{r}) + \int \frac{e^2 n_s(\boldsymbol{r}')}{|\boldsymbol{r} - \boldsymbol{r}'|}\, \mathrm{d}^3\boldsymbol{r}' + V_{XC}[n_s(\boldsymbol{r})] \tag{E.3}$$

where the second term describes Coulomb repulsion and V_{XC} is the effective exchange-correlation potential. This is the basis of density functional theory and enables greatly simplified calculation. The challenge, outside the scope of this thesis, becomes how to approximate the complex interaction between electrons and determine the electron density n. One important simplification that's been pioneered is the introduction of pseudopotentials which simplify the effective potential by largely ignoring the nucleus and the core electrons screening it. It's been shown that pseudopotentials generated with the PBEsol functional framework provide the best accuracy and precision for solids and their structural and elastic properties [176, 177, 178].

Bash script used to calculate the elastic constants of 4H-SiC after relaxing the cell and finding the equilibrium lattice constant using Quantum Espresso and thermo_pw:

```
#!/bin/sh

cat > thermo_control << EOF
 &INPUT_THERMO
  what='mur_lc_elastic_constants',
  frozen_ions=.FALSE.,
  elastic_algorithm='advanced'
 /
EOF

cat > i.cij << EOF
 &control
    calculation = 'scf'
    restart_mode='from_scratch',
    prefix='4HSiC_cij',
    pseudo_dir = '../pseudo/',
    outdir='../tmpdir/'
 /
```

```
 &system
   ibrav= 4, a=3.078,c=10.046, nat= 8, ntyp= 2,
   ecutwfc =36.0,
/
 &electrons
   conv_thr = 1.0d-8
 /
ATOMIC_SPECIES
 Si 28.086 Si.pbesol-n-kjpaw_psl.1.0.0.UPF
 C  12    C.pbesol-n-kjpaw_psl.1.0.0.UPF
ATOMIC_POSITIONS (crystal)
 C      0.000000000 0.000000000 0.187090781
 C      0.000000000 0.000000000 0.687090781
 C      0.333333333 0.666666667 0.437718884
 C      0.666666667 0.333333333 -0.062281116
 Si     0.000000000 0.000000000 -0.000238656
 Si    -0.000000000 -0.000000000 0.499761344
 Si     0.333333333 0.666666667 0.249803990
 Si     0.666666667 0.333333333 0.749803990
K_POINTS AUTOMATIC
6 6 6 1 1 1
EOF

$ECHO "\n running the thermo mur_lc_elastic_constants calculation"
$ECHO " to calculate the elastic constants of 4HSiC at the "
$ECHO " equilibrium lattice constant. The results are in o.elastic
    ...\c"
thermo_pw.x < i.cij > o.cij
check_failure $?
```

BIBLIOGRAPHY

[1] F. Ayazi, "Multi-DOF inertial MEMS: From gaming to dead reckoning," in *2011 16th International Solid-State Sensors, Actuators and Microsystems Conference*, Jun. 2011, pp. 2805–2808.

[2] D. M. Rozelle, "The hemispherical resonator gyro: From wineglass to the planets," in *Proc. 19th AAS/AIAA Space Flight Mechanics Meeting*, 2009, pp. 1157–1178.

[3] A. Shamir, "An overview of Optical Gyroscopes Theory, Practical Aspects, Applications and Future Trends," p. 24, 2006.

[4] J. Fang and J. Qin, "Advances in Atomic Gyroscopes: A View from Inertial Navigation Applications," *Sensors*, vol. 12, no. 5, pp. 6331–6346, May 11, 2012.

[5] C. Randell, C. Djiallis, and H. Muller, "Personal position measurement using dead reckoning," in *Seventh IEEE International Symposium on Wearable Computers, 2003. Proceedings.*, White Plains, NY, USA: IEEE, 2003, pp. 166–173.

[6] H. Wen, "Toward inertial-navigation-on-chip: The physics and performance scaling of multi degree-of-freedom resonant MEMS gyroscopes," Georgia Institute of Technology, May 2018.

[7] R. Abdolvand and F. Ayazi, "An advanced reactive ion etching process for very high aspect-ratio sub-micron wide trenches in silicon," *Sensors and Actuators A*, vol. 144, pp. 109–116, May 1, 2008.

[8] D. R. Myers, K. B. Cheng, B. Jamshidi, R. G. Azevedo, D. G. Senesky, L. Chen, M. Mehregany, M. B. J. Wijesundara, and A. P. Pisano, "Silicon carbide resonant tuning fork for microsensing applications in high-temperature and high G-shock environments," *Journal of Micro/Nanolithography, MEMS, and MOEMS*, vol. 8, no. 2, p. 021 116, Apr. 2009.

[9] M. Zaman and S. Rao, "BAW Gyroscope Technology Positioned to Transform Inertial MEMS Applications," p. 7, 2004.

[10] D. E. Serrano, “Integrated inertial measurement units using silicon bulk-acoustic wave gyroscopes,” Nov. 12, 2014.

[11] G. Bryan, “On the beats in the vibrations of a revolving cylinder or bell,” *Proceedings of the Cambridge Philosophical Society*, vol. 7, pp. 101–111, 1890.

[12] V. M. N. Passaro, A. Cuccovillo, L. Vaiani, M. De Carlo, and C. E. Campanella, “Gyroscope Technology and Applications: A Review in the Industrial Perspective,” *Sensors*, vol. 17, no. 10, p. 2284, Oct. 7, 2017.

[13] W.-K. Sung, “High-frequency tri-axial resonant gyroscopes,” Aug. 23, 2013.

[14] T. B. Gabrielson, “Mechanical-thermal noise in micromachined acoustic and vibration sensors,” *IEEE Transactions on Electron Devices*, vol. 40, no. 5, pp. 903–909, May 1993.

[15] M. Lerman and D. Elata, “On the quality-factor of micro-resonators,” *Procedia Engineering*, vol. 5, pp. 95–98, 2010.

[16] S. Ozdemir, S. Akhtar, O. Gunal, M. Khater, R. Saritas, E. Abdel-Rahman, and M. Yavuz, “Measuring the Quality Factor in MEMS Devices,” *Micromachines*, vol. 6, no. 12, pp. 1935–1945, Dec. 8, 2015.

[17] H. Campanella, *Acoustic Wave and Electromechanical Resonators: Concept to Key Applications*, ser. Integrated Microsystems Series. Norwood, MA: Artech House, 2010, 345 pp.

[18] S. A. Chandorkar, M. Agarwal, R. Melamud, R. N. Candler, K. E. Goodson, and T. W. Kenny, “Limits of quality factor in bulk-mode micromechanical resonators,” in *2008 IEEE 21st International Conference on Micro Electro Mechanical Systems*, Jan. 2008, pp. 74–77.

[19] R. Mirjalili, H. Wen, D. E. Serrano, and F. Ayazi, “Substrate-decoupled silicon disk resonators having degenerate gyroscopic modes with Q in excess of 1-million,” in *2015 Transducers - 2015 18th International Conference on Solid-State Sensors, Actuators and Microsystems (TRANSDUCERS)*, Jun. 2015, pp. 15–18.

[20] F. Ayazi, L. Sorenson, and R. Tabrizian, "Energy dissipation in micromechanical resonators," presented at the Micro- and Nanotechnology Sensors, Systems, and Applications III, vol. 8031, International Society for Optics and Photonics, May 13, 2011, p. 803 119.

[21] L. D. Sorenson, "Design and analysis of microelectromechanical resonators with ultra-low dissipation," Aug. 16, 2013.

[22] S. S. Iyer and R. N. Candler, "Mode- and Direction-Dependent Mechanical Energy Dissipation in Single-Crystal Resonators due to Anharmonic Phonon-Phonon Scattering," *Physical Review Applied*, vol. 5, no. 3, p. 034 002, Mar. 4, 2016.

[23] A. Akhiezer, "On the Absorption of Sound in Solids," *J. Phys. USSR*, p. 1277, 1939.

[24] T. O. Woodruff and H. Ehrenreich, "Absorption of Sound in Insulators," *Physical Review*, vol. 123, no. 5, pp. 1553–1559, Sep. 1, 1961.

[25] L. Landau, "On the Absorption of Sound in Solids," in *Collected Papers of L.D. Landau*, Elsevier, 1937, pp. 187–192.

[26] A. E. Duwel, J. Lozow, C. J. Fisher, T. Phillips, R. H. Olsson, and M. Weinberg, "Thermal energy loss mechanisms in micro- to nano-scale devices," in *Micro- and Nanotechnology Sensors, Systems, and Applications III*, vol. 8031, International Society for Optics and Photonics, May 13, 2011, p. 80311C.

[27] S. Ghaffari, S. A. Chandorkar, S. Wang, E. J. Ng, C. H. Ahn, V. Hong, Y. Yang, and T. W. Kenny, "Quantum Limit of Quality Factor in Silicon Micro and Nano Mechanical Resonators," *Scientific Reports*, vol. 3, p. 3244, Nov. 19, 2013.

[28] R. Lifshitz and M. L. Roukes, "Thermoelastic damping in micro- and nanomechanical systems," *Physical Review B*, vol. 61, no. 8, pp. 5600–5609, Feb. 15, 2000.

[29] C. Zener, "Internal Friction in Solids. I. Theory of Internal Friction in Reeds," *Physical Review*, vol. 52, no. 3, pp. 230–235, Aug. 1, 1937.

[30] R. Abdolvand, H. Johari, G. K. Ho, A. Erbil, and F. Ayazi, “Quality factor in trench-refilled polysilicon beam resonators,” *Journal of Microelectromechanical Systems*, vol. 15, no. 3, pp. 471–478, Jun. 2006.

[31] A. Duwel, R. N. Candler, T. W. Kenny, and M. Varghese, “Engineering MEMS Resonators With Low Thermoelastic Damping,” *Journal of Microelectromechanical Systems*, vol. 15, no. 6, pp. 1437–1445, Dec. 2006.

[32] S. A. Chandorkar, R. N. Candler, A. Duwel, R. Melamud, M. Agarwal, K. E. Goodson, and T. W. Kenny, “Multimode thermoelastic dissipation,” *Journal of Applied Physics*, vol. 105, no. 4, p. 043 505, Feb. 15, 2009.

[33] L. Shao and M. Palaniapan, “Effect of etch holes on quality factor of bulk-mode micromechanical resonators,” *Electronics Letters*, vol. 44, no. 15, pp. 938–940, Jul. 17, 2008.

[34] D. E. Serrano, M. F. Zaman, A. Rahafrooz, P. Hrudey, R. Lipka, D. Younkin, S. Nagpal, I. Jafri, and F. Ayazi, “Substrate-decoupled, bulk-acoustic wave gyroscopes: Design and evaluation of next-generation environmentally robust devices,” *Microsystems & Nanoengineering*, vol. 2, micronano201615, Apr. 25, 2016.

[35] L. Sorenson, J. Fu, and F. Ayazi, “Linear acoustic bandgap arrays for spurious mode suppression in piezoelectric MEMS resonators,” in *2011 Joint Conference of the IEEE International Frequency Control and the European Frequency and Time Forum (FCS) Proceedings*, May 2011, pp. 1–5.

[36] L. Sorenson, J. L. Fu, and F. Ayazi, “One-dimensional linear acoustic bandgap structures for performance enhancement of AlN-on-Silicon micromechanical resonators,” in *2011 16th International Solid-State Sensors, Actuators and Microsystems Conference*, Jun. 2011, pp. 918–921.

[37] W. E. Newell, “Miniaturization of Tuning Forks,” *Science*, vol. 161, no. 3848, pp. 1320–1326, Sep. 27, 1968.

[38] M. Bao and H. Yang, “Squeeze film air damping in MEMS,” *Sensors and Actuators A: Physical*, 25th Anniversary of Sensors and Actuators A: Physical, vol. 136, no. 1, pp. 3–27, May 1, 2007.

[39] W. S. Griffin, H. H. Richardson, and S. Yamanami, “A Study of Fluid Squeeze-Film Damping,” *Journal of Basic Engineering*, vol. 88, no. 2, pp. 451–456, Jun. 1, 1966.

[40] U. Gysin, S. Rast, P. Ruff, E. Meyer, D. W. Lee, P. Vettiger, and C. Gerber, “Temperature dependence of the force sensitivity of silicon cantilevers,” *Physical Review B*, vol. 69, no. 4, p. 045 403, Jan. 8, 2004.

[41] K. Yasumura, T. Stowe, E. Chow, T. Pfafman, T. Kenny, B. Stipe, and D. Rugar, “Quality factors in micron- and submicron-thick cantilevers,” *Journal of Microelectromechanical Systems*, vol. 9, no. 1, pp. 117–125, Mar. 2000.

[42] E. Romero, V. M. Valenzuela, A. R. Kermany, L. Sementilli, F. Iacopi, and W. P. Bowen, “Engineering the Dissipation of Crystalline Micromechanical Resonators,” *Physical Review Applied*, vol. 13, no. 4, p. 044 007, Apr. 3, 2020.

[43] B. Hamelin, V. Tavassoli, and F. Ayazi, “Microscale pierced shallow shell resonators: A test vehicle to study surface loss,” in *2017 IEEE 30th International Conference on Micro Electro Mechanical Systems (MEMS)*, Jan. 2017, pp. 1134–1137.

[44] V. Braginsky, *Systems with Small Dissipation*. University Of Chicago Press, 1986.

[45] E. Hwang and S. A. Bhave, “Experimental verification of internal friction at GHZ frequencies in doped single-crystal silicon,” in *2011 IEEE 24th International Conference on Micro Electro Mechanical Systems*, Jan. 2011, pp. 424–427.

[46] A. Samarao and F. Ayazi, “Quality Factor Sensitivity to Crystallographic Axis Misalignment in Silicon Micromechanical Resonators,” in *2010 Solid-State, Actuators, and Microsystems Workshop Technical Digest*, Hilton Head, South Carolina, USA: Transducer Research Foundation, Jun. 6, 2010, pp. 479–482.

[47] S. Nishino, J. A. Powell, and H. A. Will, “Production of large-area single-crystal wafers of cubic SiC for semiconductor devices,” *Applied Physics Letters*, vol. 42, no. 5, pp. 460–462, Mar. 1, 1983.

[48] H. Matsunami and T. Kimoto, "Step-controlled epitaxial growth of SiC: High quality homoepitaxy," *Materials Science and Engineering: R: Reports*, R20, vol. 20, no. 3, pp. 125–166, Aug. 1, 1997.

[49] R. W. Olesinski and G. J. Abbaschian, "The C-Si (Carbon-Silicon) system," *Bulletin of Alloy Phase Diagrams*, vol. 5, no. 5, pp. 486–489, Oct. 1984.

[50] P. J. Guichelaar, "Acheson Process," in *Carbide, Nitride and Boride Materials Synthesis and Processing*, A. W. Weimer, Ed., Dordrecht: Springer Netherlands, 1997, pp. 115–129.

[51] Y. M. Tairov and V. F. Tsvetkov, "Investigation of growth processes of ingots of silicon carbide single crystals," *Journal of Crystal Growth*, vol. 43, no. 2, pp. 209–212, Mar. 1, 1978.

[52] G. Ziegler, P. Lanig, D. Theis, and C. Weyrich, "Single crystal growth of SiC substrate material for blue light emitting diodes," *IEEE Transactions on Electron Devices*, vol. 30, no. 4, pp. 277–281, Apr. 1983.

[53] D. L. Barrett, R. G. Seidensticker, W. Gaida, R. H. Hopkins, and W. J. Choyke, "SiC boule growth by sublimation vapor transport," *Journal of Crystal Growth*, vol. 109, no. 1, pp. 17–23, Feb. 2, 1991.

[54] Y. M. Tairov and V. F. Tsvetkov, "General principles of growing large-size single crystals of various silicon carbide polytypes," *Journal of Crystal Growth*, vol. 52, pp. 146–150, Apr. 1, 1981.

[55] Y. M. Tairov, "Growth of bulk SiC," *Materials Science and Engineering: B*, European Materials Research Society 1994 Spring Meeting Symposium E: High Temperature Electronics: Materials, Devices and Applications, vol. 29, no. 1, pp. 83–89, Jan. 1, 1995.

[56] J. M. Dedulle, M. Anikin, M. Pons, E. Blanquet, A. Pisch, R. Madar, and C. Bernard, "Free Growth of 4H-SiC by Sublimation Method," *Materials Science Forum*, vol. 457-460, pp. 71–74, Jun. 2004.

[57] N. Schulze, D. Barrett, and G. Pensl, "Controlled Growth of 15R-SiC Single Crystals by the Modified Lely Method," *physica status solidi (a)*, vol. 178, no. 2, pp. 645–650, 2000.

[58] K. Chourou, M. Anikin, J. Bluet, V. Lauer, G. Guillot, J. Camassel, S. Juillaguet, O. Chaix, M. Pons, and R. Madar, "Experimental investigation of 4H-SiC bulk crystal growth," in *7th International Conference on Silicon Carbide, III-Nitrides and Related Materials (ICSCIII-N 97)*, ser. Materials Science Forum, vol. 264-268, Stockholm, Sweden, Aug. 1997, pp. 17–20.

[59] R. Cheung, *Silicon Carbide Microelectromechanical Systems for Harsh Environments*. World Scientific, 2006, 193 pp.

[60] A. Daruwalla, H. Wen, R. Mirjalili, and F. Ayazi, "Epitaxially-grown thick polysilicon for baw disk resonator gyroscopes with very low dissipation," in *2018 IEEE Micro Electro Mechanical Systems (MEMS)*, Belfast: IEEE, Jan. 2018, pp. 1008–1011.

[61] A. Rahafrooz, D. E. Serrano, D. Younkin, S. Nagpal, I. Jafri, and F. Ayazi, "A 0.5 mm2 7-mhz capacitive bulk acoustic wave gyroscope in (100) silicon with large dynamic range," in *2017 IEEE 30th International Conference on Micro Electro Mechanical Systems (MEMS)*, Jan. 2017, pp. 25–28.

[62] L. Di Cioccio, F. Letertre, Y. Le Tiec, A. M. Papon, C. Jaussaud, and M. Bruel, "Silicon carbide on insulator formation by the Smart-Cut® process," *Materials Science and Engineering: B*, E-MRS 1996 Spring Meeting, Symposium A: High Temperature Electronics: Materials, Devices and Applications, vol. 46, no. 1, pp. 349–356, Apr. 1, 1997.

[63] S. Ko, B. Hamelin, J. Yang, and F. Ayazi, "High-Q monocrystalline silicon carbide disk resonators fabricated using drie of thick SiC-on-insulator substrates," in *2018 IEEE Micro Electro Mechanical Systems (MEMS)*, Jan. 2018, pp. 996–999.

[64] M. Mukherjee, Ed., *Silicon Carbide - Materials, Processing and Applications in Electronic Devices*, InTech, Oct. 10, 2011.

[65] S. Kumar and J. Akhtar, "Thermal Oxidation of Silicon Carbide (SiC) – Experimentally Observed Facts," in *Silicon Carbide - Materials, Processing and Applications in Electronic Devices*, M. Mukherjee, Ed., InTech, Oct. 10, 2011.

[66] T. Suni, "Direct wafer bonding for MEMS and microelectronics," 2006.

[67] "The effects of edge trimming," p. 3, 2016.

[68] M. Ozgur, M. Pedersen, and M. Huff, "Comparison of the Etch Mask Selectivity of Nickel and Copper for a Deep, Anisotropic Plasma Etching Process of Silicon Carbide (SiC)," *ECS Journal of Solid State Science and Technology*, vol. 7, no. 2, P55–P59, 2018.

[69] K. M. Dowling, A. J. Suria, A. Shankar, C. A. Chapin, and D. G. Senesky, "Multilayer etch masks for 3-dimensional fabrication of robust silicon carbide microstructures," in *2015 28th IEEE International Conference on Micro Electro Mechanical Systems (MEMS)*, Jan. 2015, pp. 284–287.

[70] J. Yang, B. Hamelin, S. Ko, and F. Ayazi, "Ultra-High Q Monocrystalline Silicon Carbide Disk Resonators Anchored Upon A Phononic Crystal," in *2018 Solid-State, Actuators, and Microsystems Workshop Technical Digest*, Hilton Head, South Carolina, USA: Transducer Research Foundation, May 21, 2018, pp. 83–86.

[71] B. Hamelin, J. Yang, A. Daruwalla, H. Wen, and F. Ayazi, "Monocrystalline Silicon Carbide Disk Resonators on Phononic Crystals with Ultra-Low Dissipation Bulk Acoustic Wave Modes," *Scientific Reports*, vol. 9, no. 1, pp. 1–8, Dec. 10, 2019.

[72] J. Yang, B. Hamelin, and F. Ayazi, "Nano-Precision Deep Reactive Ion Etching of Monocrystalline 4H-SiCOI for Bulk Acoustic Wave Resonators with Ultra-Low Dissipation," *ECS Transactions*, vol. 97, no. 4, pp. 3–13, May 1, 2020.

[73] H.-K. Sung, T. Qiang, Z. Yao, Y. Li, Q. Wu, H.-K. Lee, B.-D. Park, W.-S. Lim, K.-H. Park, and C. Wang, "Vertical and bevel-structured SiC etching techniques incorporating different gas mixture plasmas for various microelectronic applications," *Scientific Reports*, vol. 7, no. 1, pp. 1–9, 1 Jun. 20, 2017.

[74] D. G. Senesky and A. P. Pisano, "Aluminum nitride as a masking material for the plasma etching of silicon carbide structures," in *2010 IEEE 23rd International Conference on Micro Electro Mechanical Systems (MEMS)*, Wanchai, Hong Kong, China: IEEE, Jan. 2010, pp. 352–355.

[75] N. Dartnell, M. Flowers, R. Greef, J. Zhu, and A. Blackburn, "Reactive ion etching of silicon carbide (SixC1 - x)," *Vacuum*, vol. 46, no. 4, pp. 349–355, Apr. 1, 1995.

[76] J. K. Luo, M. Pritschow, A. J. Flewitt, S. M. Spearing, N. A. Fleck, and W. I. Milne, "Effects of Process Conditions on Properties of Electroplated Ni Thin Films for Microsystem Applications," *Journal of The Electrochemical Society*, vol. 153, no. 10, p. D155, 2006.

[77] W. A. Wesley, "The Electrochemistry of Nickel," vol. 44, no. 5, p. 9, 1952.

[78] N. V. Mandich and D. W. Baudrand, "Troubleshooting Electroplating Installations: Nickel Sulfamate Plating Systems," *Sep tem b er*, p. 9, 2002.

[79] H. Cho, P. Leerungnawarat, D. C. Hays, S. J. Pearton, S. N. G. Chu, R. M. Strong, C.-M. Zetterling, M. Östling, and F. Ren, "Ultradeep, low-damage dry etching of SiC," *Applied Physics Letters*, vol. 76, no. 6, pp. 739–741, Feb. 1, 2000.

[80] P. M. Thibado, B. R. Bennett, M. E. Twigg, B. V. Shanabrook, and L. J. Whitman, "Evolution of GaSb epitaxy on GaAs(001)-c(4×4)," *Journal of Vacuum Science & Technology A*, vol. 14, no. 3, pp. 885–889, May 1, 1996.

[81] P. Leerungnawarat, K. P. Lee, S. J. Pearton, F. Ren, and S. N. G. Chu, "Comparison of F2 plasma chemistries for deep etching of SiC," *Journal of Electronic Materials*, vol. 30, no. 3, pp. 202–206, Mar. 1, 2001.

[82] L. Jiang, R. Cheung, R. Brown, and A. Mount, "Inductively coupled plasma etching of SiC in SF6/O2 and etch-induced surface chemical bonding modifications," *Journal of Applied Physics*, vol. 93, no. 3, pp. 1376–1383, Feb. 1, 2003.

[83] L. E. Luna, M. J. Tadjer, T. J. Anderson, E. A. Imhoff, K. D. Hobart, and F. J. Kub, "Deep reactive ion etching of 4H-SiC via cyclic SF6/O2 segments," *Journal of Micromechanics and Microengineering*, vol. 27, no. 9, p. 095 004, Aug. 2017.

[84] S. Bae, "Remote RF Oxygen Plasma Cleaning of the Photoresist Residue and RIE-Related Fluorocarbon Films," *Journal of the Korean Physical Society*, vol. 41, no. 2, p. 4, 2002.

[85] S. Myneni and D. W. Hess, "Post-Plasma-Etch Residue Removal Using CO 2-Based Fluids," *Journal of The Electrochemical Society*, vol. 150, no. 12, G744–G750, Dec. 1, 2003.

[86] J. Crofton, L. M. Porter, and J. R. Williams, "The Physics of Ohmic Contacts to SiC," *physica status solidi (b)*, vol. 202, no. 1, pp. 581–603, 1997.

[87] A. Nomura, S. Kurinec, and R. Raffaelle, "Ohmic contact formation on n-type 6H-SiC using polysilicon and silicides," in *2001 International Semiconductor Device Research Symposium. Symposium Proceedings (Cat. No.01EX497)*, Dec. 2001, pp. 523–526.

[88] J. P. Henning, K. J. Schoen, M. R. Melloch, J. M. Woodall, and J. A. Cooper, "Electrical characteristics of rectifying polycrystalline silicon/silicon carbide heterojunctions," *Journal of Electronic Materials*, vol. 27, no. 4, pp. 296–299, Apr. 1998.

[89] H. M. Ayedh, V. Bobal, R. Nipoti, A. Hallén, and B. G. Svensson, "Formation of carbon vacancy in 4H silicon carbide during high-temperature processing," *Journal of Applied Physics*, vol. 115, no. 1, p. 012 005, Jan. 2, 2014.

[90] T. Wimbauer, B. K. Meyer, A. Hofstaetter, A. Scharmann, and H. Overhof, "Negatively charged Si vacancy in \$4H\$ SiC: A comparison between theory and experiment," *Physical Review B*, vol. 56, no. 12, pp. 7384–7388, Sep. 15, 1997.

[91] M. O. Aboelfotoh and J. P. Doyle, "Defect energy levels in electron-irradiated and deuterium-implanted \$6H\$ silicon carbide," *Physical Review B*, vol. 59, no. 16, pp. 10 823–10 829, Apr. 15, 1999.

[92] S. Y. Han, K. H. Kim, J. K. Kim, H. W. Jang, K. H. Lee, N.-K. Kim, E. D. Kim, and J.-L. Lee, “Ohmic contact formation mechanism of Ni on n-type 4H–SiC,” *Applied Physics Letters*, vol. 79, no. 12, pp. 1816–1818, Sep. 12, 2001.

[93] G. Hui, F. Qian, T. Xiaoyan, Z. Yimen, and Z. Yuming, “Fabrication of n+ Polysilicon Ohmic Contacts with a Heterojunction Structure to n-Type 4H-Silicon Carbide,” *Journal of Semiconductors*, vol. 29, no. 4, pp. 637–640, Apr. 3, 2008.

[94] H. Zhu, D. Yang, L. Wang, and D. Due, “Thermal nitridation kinetics of silicon wafers in nitrogen atmosphere during annealing,” *Thin Solid Films*, vol. 474, no. 1, pp. 326–329, Mar. 1, 2005.

[95] Z. Hao, S. Pourkamali, and F. Ayazi, “VHF single-crystal silicon elliptic bulk-mode capacitive disk resonators-part I: Design and modeling,” *Journal of Microelectromechanical Systems*, vol. 13, no. 6, pp. 1043–1053, Dec. 2004.

[96] Z. Hao and F. Ayazi, “Support loss in micromechanical disk resonators,” in *18th IEEE International Conference on Micro Electro Mechanical Systems, 2005. MEMS 2005.*, Jan. 2005, pp. 137–141.

[97] Z. Hao and F. Ayazi, “Support loss in the radial bulk-mode vibrations of center-supported micromechanical disk resonators,” *Sensors and Actuators A: Physical*, vol. 134, no. 2, pp. 582–593, Mar. 15, 2007.

[98] X. Lu, J. Y. Lee, P. X.-L. Feng, and Q. Lin, “High Q silicon carbide microdisk resonator,” *Applied Physics Letters*, vol. 104, no. 18, p. 181 103, May 5, 2014.

[99] M. Maldovan, “Phonon wave interference and thermal bandgap materials,” *Nature Materials*, vol. 14, no. 7, p. 667, Jul. 2015.

[100] R. Martínez-Sala, J. Sancho, J. V. Sánchez, V. Gómez, J. Llinares, and F. Meseguer, “Sound attenuation by sculpture,” *Nature*, vol. 378, no. 6554, pp. 241–241, Nov. 1995.

[101] L. Yang, N. Yang, and B. Li, “Reduction of Thermal Conductivity by Nanoscale 3D Phononic Crystal,” *Scientific Reports*, vol. 3, no. 1, pp. 1–5, 1 Jan. 31, 2013.

[102] J.-K. Yu, S. Mitrovic, D. Tham, J. Varghese, and J. R. Heath, “Reduction of thermal conductivity in phononic nanomesh structures,” *Nature Nanotechnology*, vol. 5, no. 10, pp. 718–721, 10 Oct. 2010.

[103] I. El-Kady, M. F. Su, C. M. Reinke, P. E. Hopkins, D. Goettler, E. A. Shaner, and R. H. O. Iii, “Manipulation Thermal Phonons: A Phononic Crystal Route to High-ZT Thermoelectrics,” p. 9, 2011.

[104] S. Wang, L. Popa, and D. Weinstein, “GaN MEMS Resonator Using a Folded Phononic Crystal Structure,” in *2014 Solid-State, Actuators, and Microsystems Workshop Technical Digest*, Hilton Head, South Carolina, USA: Transducer Research Foundation, May 30, 2014, pp. 72–75.

[105] S. Yang, J. H. Page, Z. Liu, M. L. Cowan, C. T. Chan, and P. Sheng, “Focusing of Sound in a 3D Phononic Crystal,” *Physical Review Letters*, vol. 93, no. 2, p. 024 301, Jul. 7, 2004.

[106] J. Shi, S.-C. S. Lin, and T. J. Huang, “Wide-band acoustic collimating by phononic crystal composites,” *Applied Physics Letters*, vol. 92, no. 11, p. 111 901, Mar. 17, 2008.

[107] A. Khelif, A. Choujaa, B. Djafari-Rouhani, M. Wilm, S. Ballandras, and V. Laude, “Trapping and guiding of acoustic waves by defect modes in a full-band-gap ultrasonic crystal,” *Physical Review B*, vol. 68, no. 21, p. 214 301, Dec. 5, 2003.

[108] M. Ke, Z. Liu, C. Qiu, W. Wang, J. Shi, W. Wen, and P. Sheng, “Negative-refraction imaging with two-dimensional phononic crystals,” *Physical Review B*, vol. 72, no. 6, p. 064 306, Aug. 24, 2005.

[109] X. Zhang and Z. Liu, “Negative refraction of acoustic waves in two-dimensional phononic crystals,” *Applied Physics Letters*, vol. 85, no. 2, pp. 341–343, Jul. 8, 2004.

[110] M. Sigalas and E. Economou, “Band structure of elastic waves in two dimensional systems,” *Solid State Communications*, vol. 86, no. 3, pp. 141–143, Apr. 1993.

[111] T. Gorishnyy, C. K. Ullal, M. Maldovan, G. Fytas, and E. L. Thomas, "Hypersonic Phononic Crystals," *Physical Review Letters*, vol. 94, no. 11, p. 115 501, Mar. 22, 2005.

[112] A. Khelif and A. Adibi, Eds., *Phononic Crystals*, New York, NY: Springer New York, 2016.

[113] A. Ward and D. A. Broido, "Intrinsic phonon relaxation times from first-principles studies of the thermal conductivities of Si and Ge," *Physical Review B*, vol. 81, no. 8, p. 085 205, Feb. 4, 2010.

[114] R. T. Bonnecaze, G. J. Rodin, O. Sigmund, and J. Søndergaard Jensen, "Systematic design of phononic band–gap materials and structures by topology optimization," *Philosophical Transactions of the Royal Society of London. Series A: Mathematical, Physical and Engineering Sciences*, vol. 361, no. 1806, pp. 1001–1019, May 15, 2003.

[115] Y. Tsaturyan, A. Barg, E. S. Polzik, and A. Schliesser, "Ultracoherent nanomechanical resonators via soft clamping and dissipation dilution," *Nature Nanotechnology*, vol. 12, no. 8, nnano.2017.101, Jun. 12, 2017.

[116] F. D. Bannon, J. R. Clark, and C. T. C. Nguyen, "High-Q HF microelectromechanical filters," *IEEE Journal of Solid-State Circuits*, vol. 35, no. 4, pp. 512–526, Apr. 2000.

[117] L. Sorenson, P. Shao, and F. Ayazi, "Bulk and Surface Thermoelastic Dissipation in Micro-Hemispherical Shell Resonators," *Journal of Microelectromechanical Systems*, vol. 24, no. 2, pp. 486–502, Apr. 2015.

[118] B. J. Gallacher, J. Hedley, J. S. Burdess, A. J. Harris, A. Rickard, and D. O. King, "Electrostatic correction of structural imperfections present in a microring gyroscope," *Journal of Microelectromechanical Systems*, vol. 14, no. 2, pp. 221–234, Apr. 2005.

[119] A. K. Bhat, M. J. Storey, and S. A. Bhave, "Optomechanical sensing of wine-glass modes of a BAW resonator," in *2015 IEEE International Symposium on Inertial Sensors and Systems (ISISS) Proceedings*, Mar. 2015, pp. 1–2.

[120] X. Tang, K. Wongchotigul, and M. G. Spencer, "Optical waveguide formed by cubic silicon carbide on sapphire substrates," *Applied Physics Letters*, vol. 58, no. 9, pp. 917–918, Mar. 4, 1991.

[121] M. Fruit and P. Antoine, "Development of silicon carbide mirrors: The example of the Sofia secondary mirror," in *International Conference on Space Optics — ICSO 2000*, vol. 10569, International Society for Optics and Photonics, Nov. 21, 2017, 105691S.

[122] B. Hamelin, "Silicon Carbide (SiC) and Silicon Dioxide (SiO2) Micromechanical Resonators with Ultra-Low Dissipation," 2018.

[123] J. Rodriguez, S. A. Chandorkar, C. A. Watson, G. M. Glaze, C. H. Ahn, E. J. Ng, Y. Yang, and T. W. Kenny, "Direct Detection of Akhiezer Damping in a Silicon MEMS Resonator," *Scientific Reports*, vol. 9, no. 1, pp. 1–10, Feb. 19, 2019.

[124] G. Lamé, *Leçons sur la théorie mathématique de l'élasticité des corps solides*, in collab. with Harvard University. Paris, Bachelier, 1852, 384 pp.

[125] P. Lloyd and M. Redwood, "Finite-Difference Method for the Investigation of the Vibrations of Solids and the Evaluation of the Equivalent-Circuit Characteristics of Piezoelectric Resonators. I," *The Journal of the Acoustical Society of America*, vol. 39, no. 2, pp. 346–354, Feb. 1, 1966.

[126] C. S. Lam, A. Gao, C.-M. Lin, and J. Zou, "A Review of Lamé and Lamb Mode Crystal Resonators for Timing Applications and Prospects of Lamé and Lamb Mode PiezoMEMS Resonators for Filtering Applications," p. 12,

[127] J. Rosenbaum, *Bulk Acoustic Wave Theory and Devices*, First Edition edition. Boston: Artech Print on Demand, Jun. 1, 1988, 480 pp.

[128] A. T.-H. Lin, J. Yan, and A. A. Seshia, "Electrostatically transduced face-shear mode silicon MEMS microresonator," in *2010 IEEE International Frequency Control Symposium*, Jun. 2010, pp. 534–538.

[129] V. Kaajakari, T. Mattila, A. Oja, J. Kiihamaki, H. Kattelus, M. Koskenvuori, P. Rantakari, I. Tittonen, and H. Seppa, "Square-extensional mode single-crystal silicon micromechanical RF-resonator," vol. 2, IEEE, 2003, pp. 951–954.

[130] R. Abdolvand, B. Bahreyni, J. Lee, and F. Nabki, "Micromachined Resonators: A Review," *Micromachines*, vol. 7, no. 9, p. 160, Sep. 8, 2016.

[131] E. J. Ng, V. A. Hong, Y. Yang, C. H. Ahn, C. L. M. Everhart, and T. W. Kenny, "Temperature Dependence of the Elastic Constants of Doped Silicon," *Journal of Microelectromechanical Systems*, vol. 24, no. 3, pp. 730–741, Jun. 2015.

[132] H. Guo, Q. Feng, D. Qiao, Y. Zhang, and Y. Zhang, "Ohmic contacts with heterojunction structure to N-type 4H-silicon carbide by N^+ polysilicon film," presented at the Sixth International Conference on Thin Film Physics and Applications, Shanghai, China, Feb. 29, 2008, 69843F.

[133] L. Khine and M. Palaniapan, "High- Q bulk-mode SOI square resonators with straight-beam anchors," *Journal of Micromechanics and Microengineering*, vol. 19, no. 1, p. 015 017, 2009.

[134] Y.-W. Lin, S. Lee, S.-S. Li, Y. Xie, Z. Ren, and C.-C. Nguyen, "Series-resonant VHF micromechanical resonator reference oscillators," *IEEE Journal of Solid-State Circuits*, vol. 39, no. 12, pp. 2477–2491, Dec. 2004.

[135] H. Zhu, Y. Xu, and J. E.-Y. Lee, "Piezoresistive Readout Mechanically Coupled Lamé Mode SOI Resonator With Q of a Million," *Journal of Microelectromechanical Systems*, vol. 24, no. 4, pp. 771–780, Aug. 2015.

[136] G. Xereas and V. P. Chodavarapu, "Wafer-Level Vacuum-Encapsulated Lamé Mode Resonator With f-Q Product of $^{13\$}$ Hz," *IEEE Electron Device Letters*, vol. 36, no. 10, pp. 1079–1081, Oct. 2015.

[137] G. Wu, D. Xu, B. Xiong, and Y. Wang, "High Q Single Crystal Silicon Micromechanical Resonators With Hybrid Etching Process," *IEEE Sensors Journal*, vol. 12, no. 7, pp. 2414–2415, Jul. 2012.

[138] M. Ziaei-Moayyed, S. Habermehl, D. Branch, P. J. Clews, and R. H. Olsson, “Silicon carbide lateral overtone bulk acoustic resonator with ultrahigh quality factor,” in *2011 IEEE 24th International Conference on Micro Electro Mechanical Systems*, Cancun, Mexico: IEEE, Jan. 2011, pp. 788–792.

[139] M. Willander, M. Friesel, Q.-u. Wahab, and B. Straumal, “Silicon carbide and diamond for high temperature device applications,” *Journal of Materials Science: Materials in Electronics*, vol. 17, no. 1, p. 1, Jan. 1, 2006.

[140] C. M. DiMarino, R. Burgos, and B. Dushan, “High-temperature silicon carbide: Characterization of state-of-the-art silicon carbide power transistors,” *IEEE Industrial Electronics Magazine*, vol. 9, no. 3, pp. 19–30, Sep. 2015.

[141] S. Karmann, R. Helbig, and R. A. Stein, “Piezoelectric properties and elastic constants of 4H and 6H SiC at temperatures 4–320 K,” Oct. 27, 1998.

[142] Z. Li and R. C. Bradt, “The single crystal elastic constants of hexagonal SiC to 1000°C,” *International Journal of High Technology Ceramics*, vol. 4, no. 1, pp. 1–10, Jan. 1, 1988.

[143] K.-H. Kang, T. Eun, M.-C. Jun, and B.-J. Lee, “Governing factors for the formation of 4H or 6H-SiC polytype during SiC crystal growth: An atomistic computational approach,” *Journal of Crystal Growth*, vol. 389, pp. 120–133, Mar. 1, 2014.

[144] L. Pizzagalli, “Stability and mobility of screw dislocations in 4H, 2H and 3C silicon carbide,” *Acta Materialia*, vol. 78, pp. 236–244, Oct. 1, 2014.

[145] M. Iuga, G. Steinle-Neumann, and J. Meinhardt, “Ab-initio simulation of elastic constants for some ceramic materials,” *The European Physical Journal B*, vol. 58, no. 2, pp. 127–133, Jul. 1, 2007.

[146] K. Kamitani, M. Grimsditch, J. C. Nipko, C.-K. Loong, M. Okada, and I. Kimura, “The elastic constants of silicon carbide: A Brillouin-scattering study of 4H and 6H SiC single crystals,” *Journal of Applied Physics*, vol. 82, no. 6, pp. 3152–3154, Sep. 15, 1997.

[147] J. Chen, A. Fahim, J. C. Suhling, and R. C. Jaeger, "A Study of the Elastic Constants of 4H Silicon Carbide (4H-SiC)," in *2019 18th IEEE Intersociety Conference on Thermal and Thermomechanical Phenomena in Electronic Systems (ITherm)*, May 2019, pp. 835–840.

[148] Z. Li and R. C. Bradt, "Thermal expansion of the cubic (3C) polytype of SiC," *Journal of Materials Science*, vol. 21, no. 12, pp. 4366–4368, Dec. 1986.

[149] ——, "Thermal expansion of the hexagonal (4H) polytype of SiC," *Journal of Applied Physics*, vol. 60, no. 2, pp. 612–614, Jul. 15, 1986.

[150] ——, "Thermal Expansion of the Hexagonal (6H) Polytype of Silicon Carbide," *Journal of the American Ceramic Society*, vol. 69, no. 12, pp. 863–866, 1986.

[151] B. Andriyevsky, W. Janke, V. Stadnyk, and M. Romanyuk, "Thermal conductivity of silicon doped by phosphorus: Ab initio study," *Materials Science-Poland*, vol. 35, no. 4, pp. 717–724, Mar. 20, 2018.

[152] S. W. Van Sciver, *Helium Cryogenics*. New York, NY: Springer New York, 2012.

[153] J. B. Wachtman, W. E. Tefft, D. G. Lam, and C. S. Apstein, "Exponential Temperature Dependence of Young's Modulus for Several Oxides," *Physical Review*, vol. 122, no. 6, pp. 1754–1759, Jun. 15, 1961.

[154] E. J. Boyd, L. Li, R. Blue, and D. Uttamchandani, "Measurement of the temperature coefficient of Young's modulus of single crystal silicon and 3C silicon carbide below 273K using micro-cantilevers," *Sensors and Actuators A: Physical*, vol. 198, pp. 75–80, Aug. 15, 2013.

[155] F. Ayazi and K. Najafi, "High aspect-ratio combined poly and single-crystal silicon (HARPSS) MEMS technology," *Journal of Microelectromechanical Systems*, vol. 9, no. 3, pp. 288–294, Sep. 2000.

[156] B. Hamelin, A. Daruwalla, and F. Ayazi, "Stiffness trimming of high Q MEMS resonators by excimer laser annealing of germanium thin film on silicon," in *2016*

IEEE 29th International Conference on Micro Electro Mechanical Systems (MEMS), Jan. 2016, pp. 1026–1029.

[157] (). "GG1320AN Digital Ring Laser Gyroscope."

[158] M. A. Hopcroft, W. D. Nix, and T. W. Kenny, "What is the Young's Modulus of Silicon?" *Journal of Microelectromechanical Systems*, vol. 19, no. 2, pp. 229–238, Apr. 2010.

[159] D. Tromans, "Elastic Anisotropy of HCP Metal Crystals and Polycrystals," p. 22, 2011.

[160] A. P. Boresi, R. J. Schmidt, and O. M. Sidebottom, *Advanced Mechanics of Materials*, 5th edition. New York: John Wiley & Sons, Jan. 1993, 811 pp.

[161] W. Voigt, *Lehrbuch der Kristallphysik (mit Ausschluss der Kristalloptik)*. Vieweg+Teubner Verlag, 1928.

[162] S. I. Ranganathan and M. Ostoja-Starzewski, "Universal Elastic Anisotropy Index," *Physical Review Letters*, vol. 101, no. 5, p. 055 504, Aug. 1, 2008.

[163] C. M. Kube, "Elastic anisotropy of crystals," *AIP Advances*, vol. 6, no. 9, p. 095 209, Sep. 1, 2016.

[164] J. M. J. den Toonder, J. A. W. van Dommelen, and F. P. T. Baaijens, "The relation between single crystal elasticity and the effective elastic behaviour of polycrystalline materials: Theory, measurement and computation," *Modelling and Simulation in Materials Science and Engineering*, vol. 7, no. 6, pp. 909–928, Nov. 1, 1999.

[165] T. Ting, *Anisotropic Elasticity: Theory and Applications*, 1 edition. New York: Oxford University Press, Feb. 15, 1996, 592 pp.

[166] Z. Qin, Y. Gao, J. Jia, X. Ding, L. Huang, and H. Li, "The Effect of the Anisotropy of Single Crystal Silicon on the Frequency Split of Vibrating Ring Gyroscopes," *Micromachines*, vol. 10, no. 2, p. 126, 2 Feb. 2019.

[167] S. S. H. Chen and T. M. Liu, “Extensional vibration of thin plates of various shapes,” *The Journal of the Acoustical Society of America*, vol. 58, no. 4, pp. 828–831, Oct. 1, 1975.

[168] N. H. Farag and J. Pan, “Modal characteristics of in-plane vibration of circular plates clamped at the outer edge,” *The Journal of the Acoustical Society of America*, vol. 113, no. 4, pp. 1935–1946, Mar. 20, 2003.

[169] X. Wei and A. A. Seshia, “Analytical formulation of modal frequency split in the elliptical mode of SCS micromechanical disk resonators,” *Journal of Micromechanics and Microengineering*, vol. 24, no. 2, p. 025 011, Feb. 1, 2014.

[170] M. H. Toorani and A. A. Lakis, “General Equations of Anisotropic Plates and Shells Including Transverse Shear Deformations, Rotary Inertia and Initial Curvature Effects,” *Journal of Sound and Vibration*, vol. 237, no. 4, pp. 561–615, Nov. 2, 2000.

[171] E. Benvenisty and D. Elata, “Frequency Matching of Orthogonal Wineglass Modes in Disk and Ring Resonators Made From (100) Silicon,” *IEEE Sensors Letters*, vol. 3, no. 3, pp. 1–4, Mar. 2019.

[172] Z. Li and R. C. Bradt, “The single-crystal elastic constants of cubic (3C) SiC to 1000° C,” *Journal of Materials Science*, vol. 22, no. 7, pp. 2557–2559, Jul. 1, 1987.

[173] A. Daruwalla, “Advanced HARPSS Processes for High Q and High Frequency Inertial Sensors,” 2019.

[174] O. P. Lehar, M. A. Spak, S. Meyer, R. R. Dammel, C. J. Brodsky, and C. G. Willson, “Resist rehydration during thick film processing,” presented at the 26th Annual International Symposium on Microlithography, F. M. Houlihan, Ed., Santa Clara, CA, Aug. 24, 2001, p. 463.

[175] Y. Sensu, A. Sekiguchi, and Y. Miyake, “Study on Improved Resolution of Thick Film Resist,” p. 16, 2001.

[176] J. P. Perdew, A. Ruzsinszky, G. I. Csonka, O. A. Vydrov, G. E. Scuseria, L. A. Constantin, X. Zhou, and K. Burke, “Restoring the Density-Gradient Expansion for Exchange in Solids and Surfaces,” *Physical Review Letters*, vol. 100, no. 13, p. 136 406, Apr. 4, 2008.

[177] M. Råsander and M. A. Moram, “On the accuracy of commonly used density functional approximations in determining the elastic constants of insulators and semiconductors,” *The Journal of Chemical Physics*, vol. 143, no. 14, p. 144 104, Oct. 9, 2015.

[178] K. Lejaeghere, G. Bihlmayer, T. Björkman, P. Blaha, S. Blügel, V. Blum, D. Caliste, I. E. Castelli, S. J. Clark, A. D. Corso, S. de Gironcoli, T. Deutsch, J. K. Dewhurst, I. D. Marco, C. Draxl, M. Dułak, O. Eriksson, J. A. Flores-Livas, K. F. Garrity, L. Genovese, P. Giannozzi, M. Giantomassi, S. Goedecker, X. Gonze, O. Grånäs, E. K. U. Gross, A. Gulans, F. Gygi, D. R. Hamann, P. J. Hasnip, N. a. W. Holzwarth, D. Iuşan, D. B. Jochym, F. Jollet, D. Jones, G. Kresse, K. Koepernik, E. Küçükbenli, Y. O. Kvashnin, I. L. M. Locht, S. Lubeck, M. Marsman, N. Marzari, U. Nitzsche, L. Nordström, T. Ozaki, L. Paulatto, C. J. Pickard, W. Poelmans, M. I. J. Probert, K. Refson, M. Richter, G.-M. Rignanese, S. Saha, M. Scheffler, M. Schlipf, K. Schwarz, S. Sharma, F. Tavazza, P. Thunström, A. Tkatchenko, M. Torrent, D. Vanderbilt, M. J. van Setten, V. V. Speybroeck, J. M. Wills, J. R. Yates, G.-X. Zhang, and S. Cottenier, “Reproducibility in density functional theory calculations of solids,” *Science*, vol. 351, no. 6280, Mar. 25, 2016.